Phase Coexistence in Manganites

James Christopher Chapman

Churchill College

Cambridge

A Dissertation submitted for the Degree of Doctor of Philosophy

at the University of Cambridge

April 2005

Abstract

The doped perovskite manganite $La_{1-x}Ca_xMnO_3$ ($0<x<1$) has been extensively studied due to the interactions between the electronic, magnetic and crystal lattices, and the wide range of phases that can coexist. The region of greatest interest in the bulk material is around $x\sim0.5$, where there is often mesoscopic phase coexistence between a ferromagnetic metal (FM) and an antiferromagnetic insulator (AF).

The first part of the dissertation describes a systematic study on a series of $La_{1-x}Ca_xMnO_3$ films deposited onto $SrTiO_3$ (001) by pulsed laser deposition with compositions in the range $0.40<x<0.45$. From electrical transport and magnetisation measurements, the limit of metallic behaviour was found to be $x=0.41$ whereas ferromagnetism was seen up to $x=0.45$. Although the transition temperatures of 150-200 K were comparable with the bulk material, the saturation moment at 20 K was about 40% of the fully spin-aligned value, which suggests the possibility of a phase separated mixture of FM and AF regions. The deviation from the bulk behaviour is thought to be due to substrate-induced strain altering the crystal symmetry and making the cubic ferromagnetic state less favourable.

In the remainder of this work, the nature of phase separation in 60 nm $La_{0.59}Ca_{0.41}MnO_3$ and $La_{0.60}Ca_{0.40}MnO_3$ films is investigated. The effect of an external magnetic field is studied. A high-field magnetoresistance ($\Delta\rho/\rho_{B=0}$) of 41% in fields of 400 mT was observed for a $La_{0.60}Ca_{0.40}MnO_3$ film, which, while not as large as the values previously reported in the literature, is still significant. The magnetic history of the films was found to be very significant, with the zero-field resistivity depending on the highest field applied. The isothermal time dependence of the resistivity was found to be exponential, with a time constant in the range 100-1000 s. Possible mechanisms for the MR effect and the dependence on magnetic history are discussed.

Declaration

This dissertation is submitted for the Degree of Doctor of Philosophy in the University of Cambridge. The work has been carried out in the Department of Materials Science and Metallurgy since October 2001. Except where specific references are made, this dissertation is entirely the result of my own work and includes nothing that is the outcome of work done in collaboration. No part of this work has been or is being submitted for any other degree, diploma or qualification at this or any other university. This dissertation does not exceed 60000 words.

James Chapman
Cambridge
April 2005

Acknowledgements

I have benefited from the help and assistance of many people during the past three years. I am indebted to my supervisor, Neil Mathur for his guidance and patience throughout the past 3 years, and also for patiently proofreading the various stages of this dissertation. I also wish to thank Prof. Jan Evetts and Prof. Mark Blamire for running the group that made this research possible, and to the whole of the Device Materials Group for providing such a diverse mixture of people and ideas. Within this group various people have made particular contributions, and these are summarised below. I am grateful to Neil Mathur for training me on the PLD system, the AFM and the VSM. Throughout my time here my closest collaborator has been Bas van Aken, so many thanks to him for all the useful scientific discussions and for contributing useful ideas. Thanks must also go to Gavin Burnell, Karen Yates and John Durrell for assistance on all computer related matters and to Nadia Stelmashenko for technical support ranging from vacuum pumps and dicing saws to suit combinations. Particular thanks must also go to Dennis Leung for assistance with low-temperature measurements, to Mary Vickers for help with X-ray measurements and to John Durrell and Bas van Aken for proofreading various stages of this work.

Finally, the people themselves have made the lab an interesting place to work. So, in no particular order, I offer my thanks to Susan Cox, Luis Hueso, Leticia Granja, Laura Singh, Tarek Mouganie, Ugi Balasubramaniam, Sibe Mennema, Chris Bell, Venimadhav Adyam, Noel Rutter, Zoe Barber, Wilma Eerenstein, Alex Mischenko, Vassilka Tsaneva, Diana Sánchez-Soria, Karl Sandeman and Rumen Tomov. Despite Rumen's best efforts, this 'lazy PhD student' has finally submitted a thesis.

Away from the lab, I would like to thank all those from the Cambridge University Bridge Club. Special mention must go to Geraint Harker, Mike Scanlon Paul Hunter, and, lastly, Rob Richardson for putting up with me at the table and sharing the odd success, and a rather more frequent pint, along the way. Thanks also to Gareth Birdsall and Sonia Zakrzewski for providing me with somewhere to live for the final months.

I am grateful for the financial support of the George and Lillian Schiff Foundation and to Churchill College.

Finally, none of this would have been possible without the constant love, support and guidance of my parents back up in Cheshire. I suppose this dissertation is the end product of all the years of probing questioning, and encouraging me to think problems through to a conclusion. Unfortunately, after seven years as a student I fear it is now time to enter the real world.

James Chapman,
Cambridge, April 2005

To my parents

Contents

A note on the units used in this dissertation

Wherever possible, S.I. units and conventions have been used in this thesis. Unfortunately magnetics is one area of physics where c.g.s. units (H in Oersted, M in e.m.u./cm^3) are still widely used and magnetic results will be reported using these units. There is also the occasional use of the Ångstrom (=0.1 nm) in discussions on crystallography.

List of symbols

a,b,c	lattice parameters
a_p	(pseudo-)cubic lattice parameter
a^*	reciprocal space lattice parameter
B, **B**	magnetic flux density
C	specific heat
D	diffusion coefficient
d_{hkl}	interplanar spacing
dS	element of vector area
e	electronic charge
E_a	activation energy
E_F	Fermi energy
E_g	energy gap
E_p	polaron hopping energy
f	ferromagnetic volume fraction
f_0	equilibrium ferromagnetic volume fraction
h	Planck's constant
H, **H**	magnetic field strength
H_C	coercive field
J_H	Hund coupling constant
k	Boltzmann constant
M, **M**	magnetisation
M_R	remnant magnetisation
n	density of states
P	probability
q	reciprocal space vector
R	d.c. resistance
	radius
r_A	radius of the A-site cations
r_{Mn}	radius of $Mn^{3+/4+}$ ion
r_O	radius of O^{2-} ion
S	classical spin quantum number
t	film thickness,
	Goldschmidt tolerance factor
	time
T	temperature
T_C	Curie temperature of a ferromagnet
T_{CO}	charge-ordering temperature

T_f	glass transition temperature
T_{MI}	metal-insulator transition temperature
T_N	Néel temperature of an antiferromagnet
x, y	level of divalent ion doping, usually the level of Ca in the $La_{1-x}Ca_xMnO_3$ system
δ	oxygen vacancies
ε	induced electromotive force
	strain
θ	angle
λ	wavelength
μ	carrier mobility
ν	Poisson's ratio
ρ	d.c. resistivity
σ	electrical conductivity
σ^2	variance
τ	time constant
Φ	magnetic flux
χ	magnetic susceptibility
ω	angle
	polaron hopping frequency

Abbreviations

AF	antiferromagnet(ic)
AFM	atomic force microscopy
CAF	canted antiferromagnet
CMR	colossal magnetoresistance
CO	charge-ordered
DE	double exchange
FC	field cooled
FM	ferromagnet(ic)
FMI	ferromagnetic insulator
FMM	ferromagnetic metal
FWHM	full width at half maximum
GMR	giant magnetoresistance
JT	Jahn-Teller
LMFR	low-field magnetoresistance
MR	magnetoresistance
NMR	nuclear magnetic resonance
PLD	pulsed laser deposition
PMI	paramagnetic insulator
STS	scanning tunnelling spectroscopy
TEM	transmission electron microscopy
VRH	variable range hopping
VSM	vibrating sample magnetometer
WFMI	weakly ferromagnetic insulator
ZFC	zero-field cooled

Chapter 1 Introduction

The ability of an external magnetic field H to alter the electrical resistivity ρ of a sample has long been known and the term magnetoresistance (MR) has been adopted to quantify the relative change in the resistivity. Attempts to increase the size of the MR effect have largely been driven by the needs of the technology industry to keep up with the demand for increased magnetic storage density. Magnetoresistance has been observed in many different physical systems and there appears to be a wide range of physical mechanisms responsible for the effect. These mechanisms can be intrinsic (e.g. double exchange in colossal magnetoresistance (CMR) materials) or extrinsic (e.g. the mechanism in a manganite tunnel junction). Typically intrinsic effects are due to the alignment of atomic spins and may only become significant in fields of several tesla, whereas extrinsic effects originate in the alignment of magnetic domains and can be seen in fields of a few millitesla.

The scale of the MR effect can also vary widely, from typically less than 1% in fields of several tesla in simple metals at room temperature [1], to 10^{12}% at 40 K in $Pr_{0.67}Ca_{0.33}MnO_3$ when the 'charge-ordered' phase is melted in a 4 T magnetic field [2]. It should be noted that there are two alternative definitions for MR (equations 1.1 and 1.2) used in the literature.

$$MR(H) = \frac{\rho(H=0) - \rho(H)}{\rho(H)} \tag{1.1}$$

$$MR(H) = \frac{\rho(H=0) - \rho(H)}{\rho(H=0)} \tag{1.2}$$

There is no upper limit on the MR using the first definition, but the second definition has an upper limit of 100%. For low MR values there is little difference between the two definitions but the values diverge as the MR increases. For comparison, the $\Delta\rho/\rho(H)$ value of 127000% obtained by Jin *et al.* [3] corresponds to a $\Delta\rho/\rho(H=0)$ value of 99.92%. The two MR values quoted in the first paragraph use the first definition. However, unless otherwise stated, all MR values quoted in this dissertation will use equation 1.2.

With the discovery of the CMR effect in $La_{0.67}Ca_{0.33}MnO_3$ in 1994 by Jin *et al*. [3], CMR materials were suggested as the basis of the next generation of disc-drive read heads. However, CMR materials could not compete with the incumbent giant magnetoresistance (GMR) materials, so the interest of the data storage industry was lost. The GMR effect was first seen in 1988 in Fe/Cr multilayers where the Fe layers were antiferromagnetically coupled through the non-magnetic Cr layers [4]. The GMR effect was a significant discovery because, as well as having an MR of ~50% at 4.2 K, GMR was an extrinsically engineerable effect and the MR value could be optimised. Within a decade, IBM had shipped the first disc drives with read heads comprising advanced GMR devices, or 'spin valves.'

The main drawbacks with CMR materials that made them unsuitable for technological applications were that the intrinsic MR effect requires fields of several tesla and, while this high-field MR effect close to the Curie temperature T_C is large, away from T_C the effect is negligible. By introducing artificial boundaries into CMR materials a low-field MR effect can be seen [5], but this low-field effect is extremely sensitive to the precise temperature. Therefore, CMR materials are now studied mainly for their scientific interest. Since 1994 the CMR effect has also been seen in layered perovskites such as $La_{2-2x}Sr_{1+2x}Mn_2O_7$ [6] and at higher temperatures in the double perovskite Sr_2FeMnO_6 [7].

The prototypical CMR material has the chemical formula $A_{1-x}B_xMnO_3$ (A=La, Pr, B=Ca, Sr, Ba, $0<x<1$) and exhibits a wide range of interesting scientific features including a rich phase diagram with various types of magnetic and electrical phases [8], intrinsic phase separation on micron lengthscales [9], a large CMR effect in the bulk material [3], a low-field MR effect at 100 mT originating in artificially induced constrictions [5], and almost complete spin polarisation in the ferromagnetic region at low temperature [10-13]. The electrical and magnetic properties can often be tuned by varying numerous external parameters including temperature [14] and magnetic field [15]. Furthermore, there are often significant differences between the properties of bulk samples and thin films due to the effects of substrate-induced strain [16].

This dissertation is concerned with epitaxial thin films of $La_{1-x}Ca_xMnO_3$ ($0<x<1$). In the bulk form, $La_{1-x}Ca_xMnO_3$ exhibits a wide range of phases including a ferromagnetic metal, a 'charge-ordered' antiferromagnetic insulator and a paramagnetic insulator depending on the level of Ca doping and temperature. These phases have been shown to coexist over surprisingly small lengthscales [9], and the phase-separated nature of $La_{1-x}Ca_xMnO_3$ is now well established. In epitaxial thin films, there will be an induced strain due to the slight lattice mismatch between the manganite and the substrate. This strain will alter the crystal symmetry of the film and change the Mn-O bond lengths. This can affect the relative stabilities of the competing phases. It is the change in stability of the ferromagnetic metallic phase due to strain which this dissertation attempts to investigate.

Overview of this dissertation

The focus of this dissertation is an experimental investigation of the effects of strain on the low temperature ground state of $La_{1-x}Ca_xMnO_3$ films in the range $0.40<x<0.45$. It can be divided broadly into two parts. The first part will set the work in context using a range of review articles. Chapter 2 will introduce the doped perovskite manganites, and discuss the underlying physical concepts, with emphasis on the properties of $La_{1-x}Ca_xMnO_3$. The topics discussed include the Jahn-Teller effect, the double exchange model, electron-lattice interactions and the effects of substrate-induced strain. Chapter 3 will conduct a review of the evidence for phase separation in the manganites including their time-dependent properties.

In the second part, the focus changes to experimental work. The experimental methods used in this study, which include pulsed laser deposition, sample characterisation using atomic force microscopy and X-ray diffraction, and the electrical and magnetic characterisation techniques are described in Chapter 4. In Chapter 5 a systematic study is made of the properties of a series of $La_{1-x}Ca_xMnO_3$ films ($0.40<x<0.45$) grown on $SrTiO_3$ (001). The electrical and magnetic properties are investigated as a function of temperature and a simple phase diagram for 60 nm thin films is constructed. There is also a short comparison with transport data and preliminary magnetic data from a similar set of less-strained films grown on paramagnetic $NdGaO_3$ (001) substrates. Due to the high paramagnetic signal from the

$NdGaO_3$ substrates only limited magnetic data is presented for this set of films. From these results it appears that the limit of metallic behaviour at low temperature is shifted from x=0.50 for the bulk material to x=0.41 for these strained films, although all the films studied here showed some degree of ferromagnetism at 20 K. Chapter 6 describes the magnetoresistance effects seen in these films as a function of magnetic field and temperature and offers evidence that phase-separated systems can be thought of as a cluster of interacting magnetic nanoparticles. The isothermal time dependence of the resistivity and magnetisation when the external field was altered is investigated in Chapter 7. A memory effect was seen where the *maximum* field applied was encoded into the zero-field resistivity. The time dependence immediately after the field was altered was fitted to a simple exponential decay of the form

$$\rho(t)=a+b\exp(-(t-t_0)/\tau), \qquad (1.3)$$

and values obtained for the time constant τ. The values of τ are linked to the magnetic history of the films.

Finally, Chapter 8 contains a summary of the findings and suggestions for further work.

References for Chapter 1

[1] J.P. Heremans, *Magnetic Field Sensors for Magnetic Position Sensing in Automotive Application.* Mat. Res. Soc. Symp. Proc. **475**, 63-74 (1997).

[2] A. Anane, J.-P. Renard, L. Reversat, C. Dupas, P. Veillet, M. Viret, L. Pinsard and A. Revcolevschi, *Colossal resistive relaxation effects in a $Pr_{0.67}Ca_{0.33}MnO_3$ single crystal.* Phys. Rev. B **59**, 77-80 (1999).

[3] S. Jin, T.H. Tiefel, M. McCormack, R.A. Fastnacht, R. Ramesh and L.H. Chen, *Thousandfold Change in Resistivity in Magnetoresistive La-Ca-Mn-O Films.* Science **264**, 413-5 (1994).

[4] M.N. Baibich, J.M. Broto, A. Fert, F. Nguyen Van Dau, F. Petroff, P. Eitenne, G. Creuzet, A. Friederich and J. Chazelas, *Giant Magnetoresistance of (001)Fe/(001)Cr Magnetic Superlattices.* Phys. Rev. Lett. **61**, 2472-5 (1988).

[5] N.D. Mathur, P.B. Littlewood, N.K. Todd, S.P. Isaac, B.-S. Teo, D.-J. Kang, E.J. Tarte, Z.H. Barber, J.E. Evetts and M.G. Blamire, *Resistance of a domain wall in $La_{0.7}Ca_{0.3}MnO_3$.* J. Appl. Phys. **86**, 6287-90 (1999).

[6] Y. Moritomo, A. Asamitsu, H. Kuwahara and Y. Tokura, *Giant magnetoresistance of manganese oxides with a layered perovskite structure.* Nature **380**, 141-4 (1996).

[7] K.-I. Kobayashi, T. Kimura, H. Sawada, K. Terakura and Y. Tokura, *Room-temperature magnetoresistance in an oxide material with an ordered double-perovskite structure.* Nature **395**, 677-80 (1998).

[8] S.-W. Cheong and H.Y. Hwang, in *Colossal Magnetoresistance Oxides* (Ed. Y. Tokura), Gordon & Breach, New York (1997).

[9] M. Uehara, S. Mori, C.H. Chen and S.-W. Cheong, *Percolative phase separation underlies colossal magnetoresistance in mixed-valent manganites.* Nature **399**, 560-3 (1999).

[10] J.Y.T. Wei, N.-C. Yeh and R.P. Vasquez, *Tunnelling Evidence of Half-Metallic Ferromagnetism in $La_{0.7}Ca_{0.3}MnO_3$.* Phys. Rev. Lett. **79**, 5150-3 (1997).

[11] Y. Okimoto, T. Katsufuji, T. Ishikawa, A. Urushibara, T. Arima and Y. Tokura, *Anomalous Variation of Optical Spectra with Spin Polarization in Double-Exchange Ferromagnet: $La_{1-x}Sr_xMnO_3$.* Phys. Rev. Lett. **75**, 109-12 (1995).

[12] M.-H. Jo, N.D. Mathur, N.K. Todd and M.G. Blamire, *Very large magnetoresistance and coherent switching in half-metallic manganite tunnel junctions.* Phys. Rev. B **61**, R14905-8 (2000).

[13] M. Bowen, M. Bibes, A. Barthélémy, J.-P. Contour, A. Anane, Y. Lemaître and A. Fert, *Nearly total spin polarisation in $La_{2/3}Sr_{1/3}MnO_3$ from tunnelling experiments.* Appl. Phys. Lett. **82**, 233-5 (2003).

[14] N.A. Babushkina, L.M. Belova, D.I. Khomskii, K.I. Kugel, O.Yu. Gorbenko and A.R. Kaul, *Low-temperature transition to a metallic state in $(La_{0.5}Pr_{0.5})_{0.7}Ca_{0.3}MnO_3$ films.* Phys. Rev. B **59**, 6994-7000 (1999).

[15] A. Asamitsu, Y. Moritomo, Y. Tomioka, T. Arima and Y. Tokura, *A structural phase transition induced by an external magnetic field.* Nature **373**, 407-9 (1995).

[16] E.B. Nyeanchi, I.P. Krylov, X.-M. Zhu and N. Jacobs, *Ferromagnetic ground state in $La_{0.5}Ca_{0.5}MnO_3$ thin films.* Europhys. Lett. **48**, 228-32 (1999).

Chapter 2 An introduction to the manganites

2.1 Historical background

There were reports of interesting behaviour in the doped perovskite manganites as far back as 1950. Jonker and Van Santen [1,2] carried out early work on the compounds $La_{1-x}A_xMnO_3$ with A = Ca, Sr and Ba. They found that the end members of the series, corresponding to x=0 and x=1, were antiferromagnetic insulators. However, intermediate values of x gave ferromagnetism, particularly around x=0.3. They found that the onset of ferromagnetism was associated with a sharp increase in electrical conductivity. In 1951, Zener proposed a double exchange model [3] to explain the link seen by Jonker and Van Santen between ferromagnetism and metallic behaviour. The first report of magnetoresistance (MR) was by Volger in 1954 [4]. In 1955 Wollan and Koehler reported neutron diffraction peaks corresponding to ferromagnetic (FM) regions, antiferromagnetic (AF) regions and occasionally FM and AF regions simultaneously in $La_{1-x}Ca_xMnO_3$ [5]. This was the earliest report of phase coexistence in the manganites. Phase coexistence will be discussed in more detail in Chapter 3.

There was little further activity until the early 1990s, when there were reports of 'colossal' magnetoresistance values. In 1993 a MR value ($\Delta\rho/\rho(H=0)$) of 60% was reported in $La_{2/3}Ba_{1/3}MnO_3$ films [6]. A year later in 1994 Jin *et al.* [7] discovered the colossal magnetoresistance (CMR) effect in strained annealed $La_{0.67}Ca_{0.33}MnO_3$ thin films. In what was possibly then the most dramatic magnetoresistance effect, application of a 6 T external magnetic field altered the resistivity around the Curie temperature by six orders of magnitude and gave a $\Delta\rho/\rho(H=0)$ value of 99.92%. There was comparatively little effect well above or well below T_C, as shown in Figure 2.1 and Figure 2.2.

There was a sharp upturn of interest in $La_{1-x}Ca_xMnO_3$ with $0.2<x<0.5$ after the discovery of the CMR effect. In this system, $La_{5/8}Ca_{3/8}MnO_3$ was found to have the highest Curie temperature T_C of 265 K [8]. These initial results were in qualitative agreement with Zener's original double exchange model, but the transition temperatures seen were an order of magnitude below the original theoretical

predictions. Clearly further work, both theoretical and experimental, was required to understand fully the fundamental physics involved. In particular, the magnitude of the CMR effect could not be explained by double exchange alone.

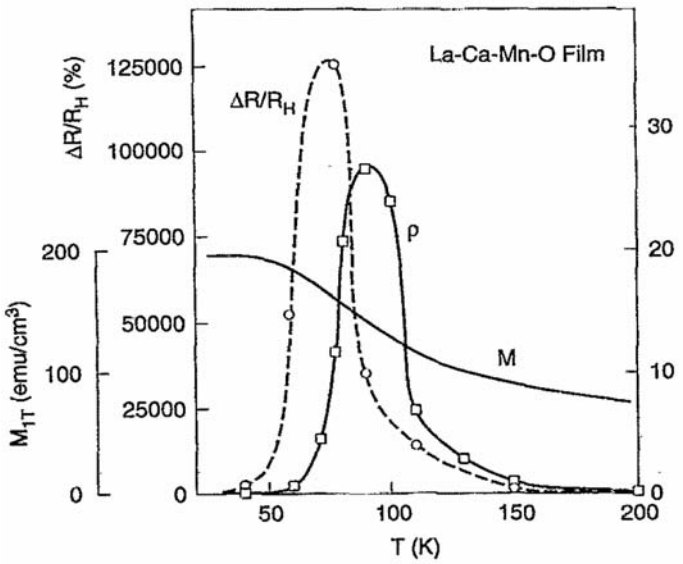

Figure 2.1. Resistivity, magnetoresistance and magnetisation data for an epitaxial $La_{0.67}Ca_{0.33}MnO_3$ film. Note that the MR values are quoted as $\Delta R/R_H$. (Taken from [9].)

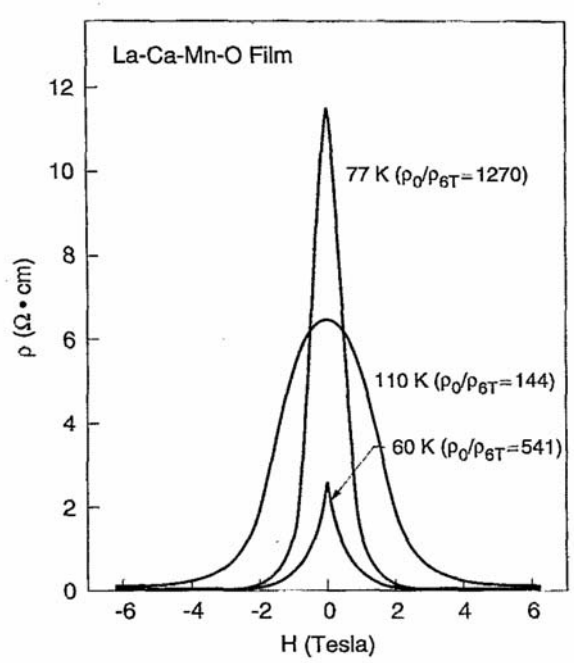

Figure 2.2. Resistivity as a function of applied field at 60 K, 77 K and 110 K for epitaxial $La_{0.67}Ca_{0.33}MnO_3$ films. (Taken from [9].)

2.2 Crystal structure and electronic studies

$La_{1-x}Ca_xMnO_3$ is a member of the perovskite family which has the general chemical formula ABO_3. The Mn ions occupy the B-site at the centre of the unit cell and are octahedrally coordinated by the oxygen ions. Adjacent MnO_6 octahedra are linked at their vertices. The La^{3+} and Ca^{2+} ions are then distributed randomly over the A-sites in the crystal. A cubic unit cell is shown in Figure 2.3. This cubic unit cell is idealised and is only seen at high temperature, above ~1000 K, where most perovskites are cubic. As the temperature is lowered, the MnO_6 octahedra distort and rotate around the oxygen links, thereby reducing the symmetry of the $La_{1-x}Ca_xMnO_3$ system. Below 700 K the structure remains orthorhombic *Pnma* for all levels of calcium doping, and therefore the $La_{1-x}Ca_xMnO_3$ system can be studied in the absence of structural phase transitions.

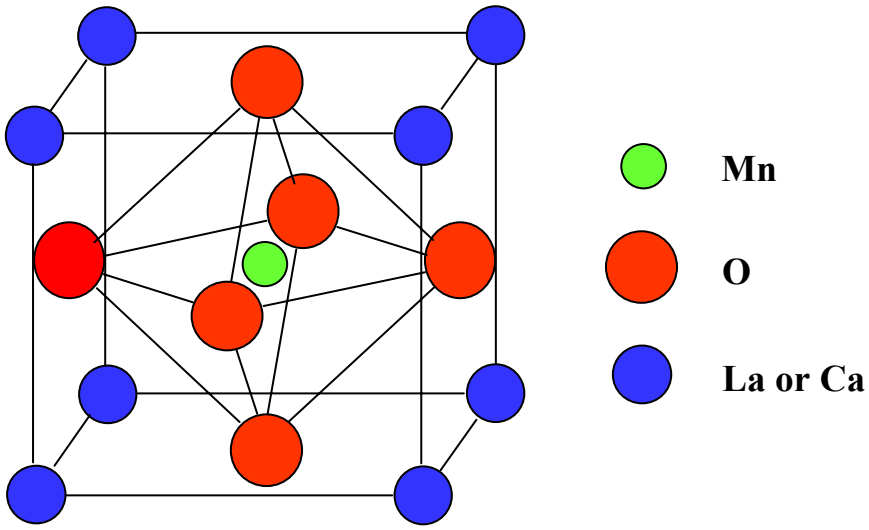

Figure 2.3. The perovskite building block of (La,Ca)MnO_3. Lanthanum and calcium occupy the A-sites and manganese occupies the central B-site.

2.2.1 A-site cation size

If the ions can be treated as hard spheres that just touch each other in equilibrium, then we can use the Goldschmidt tolerance factor *t* to parameterise any distortions from the ideal structure. This is defined as the ratio of the length of the

face diagonal to $\sqrt{2}$ times the cube edge. In terms of ionic radii, t is given by

$$t = \frac{\langle r_A \rangle + r_O}{\sqrt{2}(r_{Mn} + r_O)}. \qquad (2.1)$$

Here r_{Mn} and r_O are the radii of the manganese and oxygen ions respectively and $\langle r_A \rangle$ is the average radius of the A-site cations. If the A-site cation were to exactly fill the interstice then t=1 and the perovskite would be cubic. In practice this is not the case and stable structures generally lie in the range $0.8<t<1$. In the calculations which follow a coordination number of nine has been assumed for the A-site cations and the ionic radii values are taken from Shannon [10]. The radii of Mn^{3+} and Mn^{4+} are 0.58 Å and 0.53 Å respectively, so the average value of r_{Mn} will depend on the ratio of the two types of manganese ion present. The value for r_O is 1.21 Å, so to obtain the ideal cubic structure $\langle r_A \rangle$ must vary linearly between 1.32 Å for x=0 and 1.25 Å for x=1. The closer $\langle r_A \rangle$ is to this ideal value, the better the overlap between the Mn 3d and O 2p orbitals will be and the greater the stability of the metallic phase [11]. Note that the reported values of t depend strongly on the ionic radii and coordination numbers used.

In practice, the A-site ions are smaller than the ideal radius, which leads to a rotation of the MnO_6 octahedra. La^{3+} and Ca^{2+} have mean radii of 1.216 Å and 1.18 Å respectively, which leads to a tolerance factor of 0.958 for $LaMnO_3$ and 0.971 for $CaMnO_3$. For x=0.5, $\langle r_A \rangle$=1.198 Å and the tolerance factor is 0.965. This value of $\langle r_A \rangle$ is substantially less than the ideal value of 1.286 Å, and the MnO_6 octahedra rotate or distort to improve the packing. The true unit cell is an orthorhombic *Pnma* cell as stated earlier. The *Pnma* lattice structure can be derived from the ideal cubic perovskite cell as follows:

(i) Rotate an oxygen octahedron around the z-axis. Since the octahedra remain connected, the attached octahedra in the x-y plane rotate in the opposite sense. This results in a $\sqrt{2} \times \sqrt{2}$ doubling of the cell (conventionally taken to be the a-c plane). This reduces the symmetry to tetragonal ($b \neq a=c$).

(ii) Tilt an octahedron along the Mn-O-Mn bond in the c direction in the a-c plane, leading to opposite tilting of the neighbouring layers. This results in a further

doubling of the primitive unit cell along the *b* axis and orthorhombic symmetry. This leads to a slight reduction in *b* and one in-plane parameter (conventionally taken to be *c*). The unit cell volume tends to be conserved, so there is a slight increase in *a*.

The true unit cell is orthorhombic *Pnma* with $a \approx c \approx \sqrt{2}a_p$ and $b \approx 2a_p$, where a_p is the lattice parameter of the pseudo-cubic unit cell. The unit-cell of $La_{1-x}Ca_xMnO_3$ remains orthorhombic for all levels of Ca doping. The true unit cell is shown in Figure 2.4 and the relationship between cubic and orthorhombic unit cells is given in Figure 2.5.

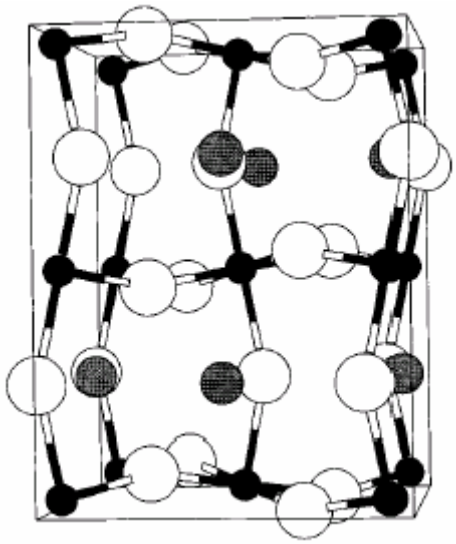

Figure 2.4. The Pnma unit cell of $La_{1-x}Ca_xMnO_3$, giving an impression of the distortions from the cubic unit cell. The ions are represented by black (manganese), grey (La or Ca) and white (oxygen) spheres respectively. The region shown comprises four cubic perovskite building blocks. (Taken from [12].)

The primary method of electronic conduction in the manganites is via the conduction band formed from the overlap of the Mn 3d and O 2p orbitals. The degree of overlap is maximised for a cubic perovskite structure (structure factor = 1). Any deviations from this, either by lengthening or bending the Mn-O-Mn bond, will reduce the orbital overlap and the hopping amplitude of the itinerant e_g electron. It is possible to investigate the effects of chemical pressure on the Mn-O-Mn bond by substituting trivalent ions of differing sizes into the perovskite structure while keeping

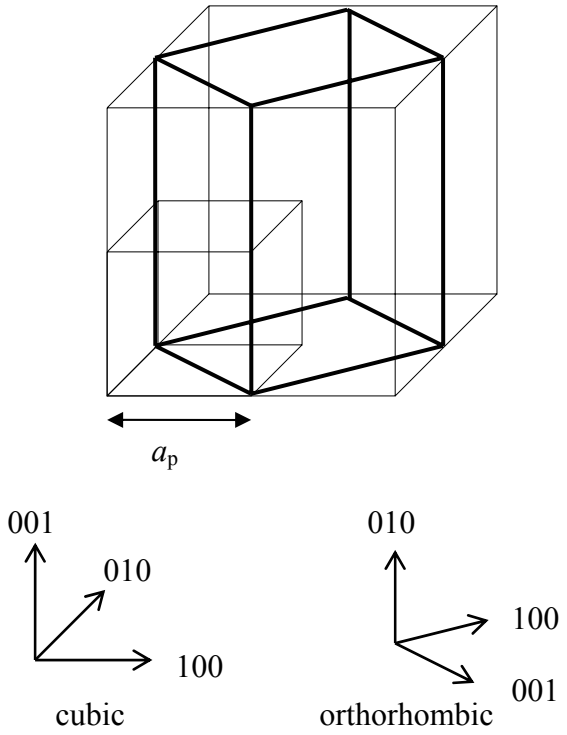

Figure 2.5. Orthorhombic (thick lines) and cubic (thin lines) unit cells for $La_{1-x}Ca_xMnO_3$ and the relative orientations of the crystallographic axes.

the fraction of divalent ions constant. Crucially this ionic substitution will leave the valency of the manganese ions and the number of potentially itinerant electrons unaltered. However, this introduces disorder into the crystal.

Ignoring this cation disorder, the effects of the average A-site cation size have been investigated by numerous groups (see reference [13] for a review), and a typical result is shown in Figure 2.6. Further studies have shown that the magnetoresistance increased and T_C decreased with decreasing $\langle r_A \rangle$ [14].

In 2000 Rodruíguez-Martínez and Attfield studied polycrystalline samples of $La_{0.7}M_{0.3}MnO_3$ with differing distributions of the A-site cations [11]. They used two parameters; the average radius $\langle r_A \rangle$, which is related to static distortions, and the

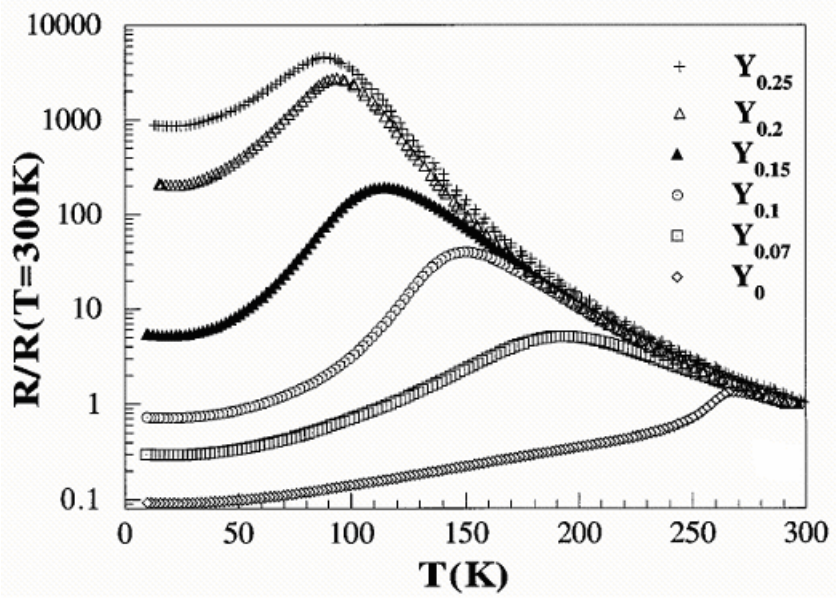

Figure 2.6. Normalised resistivity [R(T)/R(T=300 K)] vs. temperature for a series of samples of $La_{0.7-x}Y_xCa_{0.3}MnO_3$ with x=0, 0.07, 0.1, 0.15, 0.2, and 0.25. The Mn-O-Mn bond becomes more non-linear with increasing Y content. (Taken from [15].)

variance $\sigma^2 = \langle r^2_A \rangle - \langle r_A \rangle^2$, which is related to disorder. The compositions studied were such that $\langle r_A \rangle$ was held constant at 1.20 Å, but σ^2 varied from 0.0003 Å^2 to 0.0090 Å^2. All samples underwent a metal-insulator transition (Figure 2.7), but there were two distinct groups of transition temperatures T_{MI}. T_{MI} was suppressed to 70-100 K for the larger σ^2 values (above 0.005 Å^2) and the room temperature resistivity for these samples was an order of magnitude higher. The same authors proposed a 'chemical window' for $La_{0.7}M_{0.3}MnO_3$ in the $\langle r_A \rangle$–σ^2 plane (Figure 2.8). Empirical estimates have indicated that an ideal cubic manganite would have a T_C of 520 K.

Further evidence for the importance of the A-site cation distribution was seen by Uehara *et al.* in the $La_{5/8-y}Pr_yCa_{3/8}MnO_3$ system [16]. It was found that by altering the level of Pr doping the ground state could be tuned from a ferromagnetic metal (y=0) to a charge-ordered antiferromagnetic insulator (y=1). Furthermore, around y=0.3 there was coexistence between a charge-ordered and a charge-disordered phase on micron lengthscales. The charge-disordered phase was inferred to be a ferromagnetic metal from macroscopic resistivity and magnetisation data.

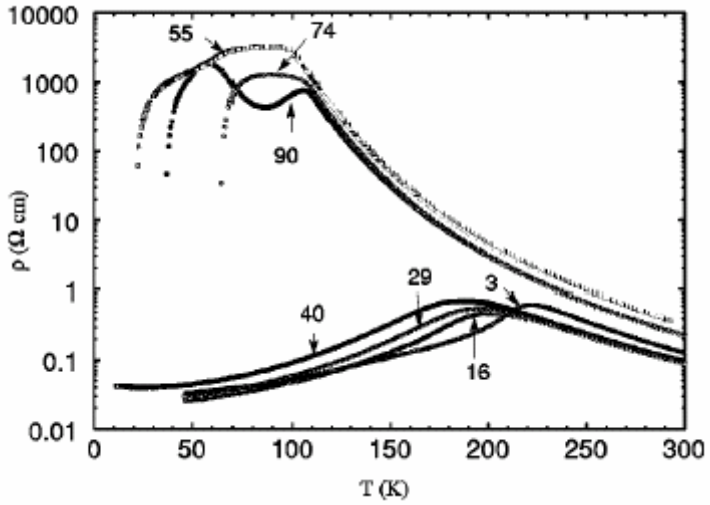

Figure 2.7. Temperature dependence of resistivity for polycrystalline samples of $La_{0.7}M_{0.3}MnO_3$. The average A-site cation size is 1.20 Å and the labels show σ^2 ($\times 10^4$ Å^2) values. (Taken from [11].)

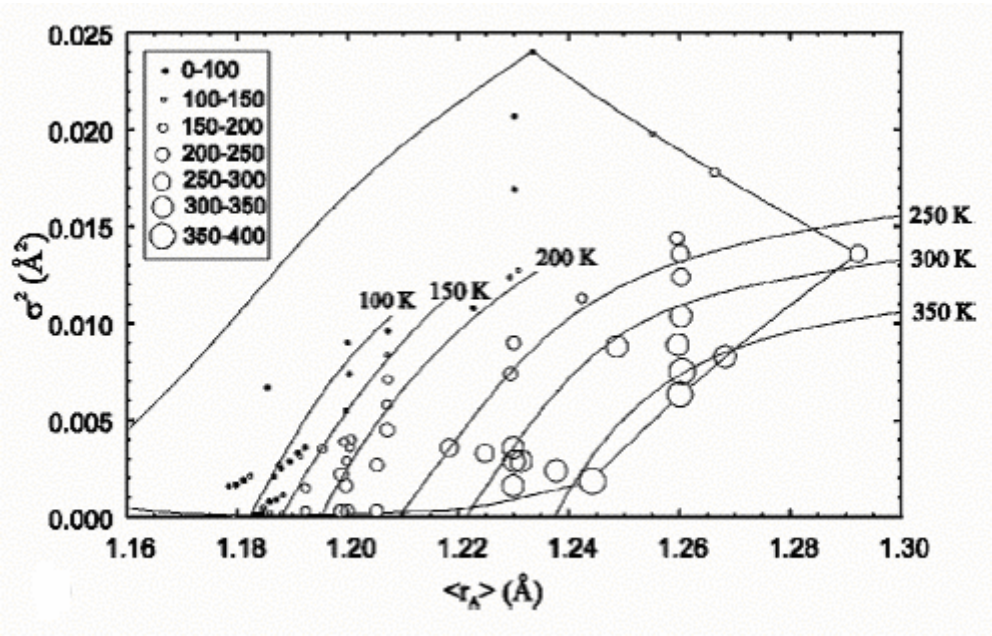

Figure 2.8. Metal-insulator transition temperatures for $La_{0.7}M_{0.3}MnO_3$ plotted in the $\langle r_A \rangle$–σ^2 plane. Values of the metal-insulator transition T_{MI} (in 50 K intervals) and approximate isotherms are shown. The ideal $La_{0.7}M_{0.3}MnO_3$ perovskite (with t=1 and σ^2=0) lies in the bottom right corner and has an estimated T_{MI} of 520 K. (Taken from [11].)

2.2.2 Crystal field splitting and the Jahn-Teller effect

Neutral manganese has the electron configuration $1s^2 2s^2 2p^6 3s^2 3p^6 3d^5 4s^2$. The first two electrons to be lost on ionisation are the two outermost 4s electrons. Thus, the three electrons that are lost to form a Mn^{3+} ion are the two from the 4s orbital and one further electron from the 3d energy level. The additional electron that is lost to form Mn^{4+} comes from the 3d level. Mn^{3+} has an outer electron configuration of $3d^4$ and the configuration of Mn^{4+} is $3d^3$.

In the undistorted perovskite structure, the Mn ions sit on an octahedral site, and the 5-fold degeneracy of the 3d orbitals is split by the octahedral crystal field. This leads to a low-lying t_{2g} triplet and a higher energy e_g doublet as depicted in Figure 2.9. Double occupancy of an individual t_{2g} level is strongly suppressed by Hund coupling and electrostatic repulsion, so the three 3d electrons in Mn^{4+} are spin aligned in the t_{2g} levels (S=3/2). The Mn^{3+} ion has one additional electron, which does not occupy a t_{2g} level due to strong Coulomb repulsion and the Pauli Exclusion Principle, but instead occupies one of the e_g levels. This electron is also strongly Hund coupled and therefore spin-aligned with the t_{2g} triplet.

There is a further possible splitting of the t_{2g} and e_g energy levels if manganese undergoes a Jahn-Teller distortion. Under such a distortion, both the t_{2g} and e_g sets of orbitals are split in energy, with the mean of each set remaining constant. A schematic representation is shown in Figure 2.9. The Jahn-Teller distortion is only energetically favourable if either of the t_{2g} or e_g sets is partially occupied. This only occurs for Mn^{3+} with its single e_g electron. In a Jahn-Teller distortion the Mn-O bond length is increased in the *c* direction and increased slightly in the *a*-*b* plane.

The Mn-O bonds are primarily responsible for the electrical conduction throughout the sample. In an octahedral environment, the orbitals in the Mn t_{2g} triplet (*xy*, *yz* and *zx* symmetries) have poor overlap with the oxygen 2p orbitals and are all strongly localised. However, the e_g orbitals ($3z^2$-r^2 and x^2–y^2 symmetries) are more diffuse and point towards the O 2p orbitals. The probability of overlap between a Mn e_g orbital and an O 2p orbital is sufficiently large for a hopping mechanism to be a plausible method of conduction. The closer the Mn-O-Mn bonds are to being linear and the shorter the Mn-O distance, then the better the overlap between the relevant

orbitals, and the higher the probability of hopping occurring. The length and angle of the Mn-O-Mn bonds is affected by the radii of the A-site cations.

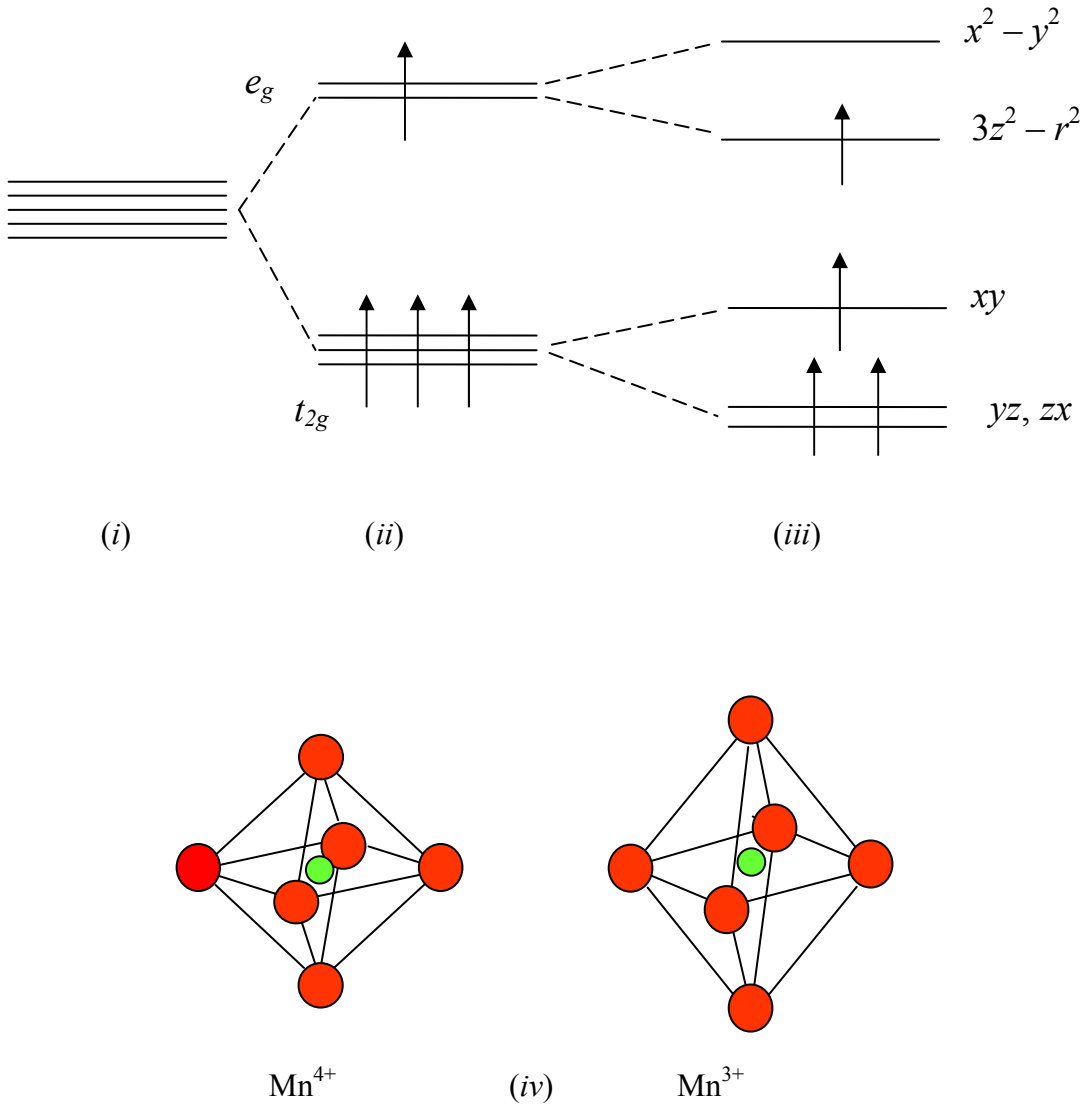

Figure 2.9. A schematic diagram showing the relative energies of the Mn 3d orbitals (i) in isolation, (ii) in an octahedral environment such as the MnO_6 octahedra, and (iii) after undergoing a Jahn-Teller distortion. (iv) The shape of the MnO_6 octahedron for Mn^{4+} and Mn^{3+} ions.

When an e_g electron moves between adjacent Mn ions the Jahn-Teller induced lattice distortion moves with it. This coupling between the lattice distortion and the e_g electron is known as a *polaron*. At room temperature, the polarons are free to move throughout the crystal and the paramagnetic state is essentially a polaronic liquid [17].

2.2.3 Magnetic interactions

The magnetic properties of the manganites are largely determined by transfer of electrons between the manganese and oxygen orbitals that point towards each other. The direct overlap between the atomic manganese orbitals is small and the magnetic interaction is mediated by intervening O 2p electrons. There are two important interactions, namely double exchange and superexchange. These are discussed in more detail below.

2.2.3.1 Double exchange

The basic idea of double exchange (DE) as a mechanism for electrical conduction in the manganites was postulated by Zener [3]. In the initial model there was the *simultaneous* transfer of one electron from a manganese 3d e_g orbital to an oxygen 2p orbital and transfer from the same oxygen 2p to a manganese 3d e_g orbital on an adjacent ion as shown in Figure 2.10. In this way the e_g electrons are able to move throughout the lattice. Both electrons involved in the exchange must have the same spin (because of the Pauli Exclusion Principle). This leads to a ferromagnetic arrangement of the e_g electrons.

Zener calculated that the electrical conductivity σ was given by equation 2.2 where x is the level of calcium doping, a_p is the pseudo-cubic lattice parameter, h is Planck's constant, e the charge of an electron, T is the temperature and T_C is the Curie temperature.

$$\sigma = \left(\frac{xe^2}{a_p h}\right)\left(\frac{T_C}{T}\right) \qquad (2.2)$$

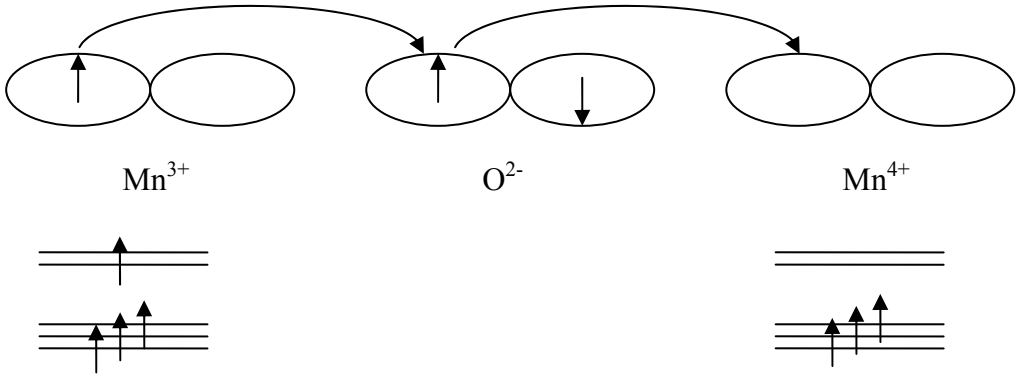

Figure 2.10. A schematic diagram of the double exchange mechanism showing the simultaneous transfer of electrons between adjacent ions and the orientation of the Mn spins.

Further theoretical work was performed by Anderson and Hasegawa [18] and de Gennes [19]. In the limit of large Hund (J_H) coupling, the spin of the e_g electron is tied to the core t_{2g} spin and the hopping parameter t varies as

$$t_{ij} = t\cos\left(\frac{\theta_{ij}}{2}\right) \qquad (J_H >> t), \qquad (2.3)$$

where θ_{ij} is the angle between the core t_{2g} spins on adjacent manganese ions. It should be noted that t_{ij} only depends on the *relative* orientation of the two spins and not their absolute direction with respect to the crystallographic axes. The kinetic energy of the e_g electron is proportional to t. Thus, in the DE model, if the manganese spins are arranged ferromagnetically then t will be maximised and electrical resistivity should have a minimum value. Therefore, ferromagnetism and metallicity are intimately linked. The basic DE model is in qualitative agreement with the experimental data. However, it cannot successfully explain the resistivity of the insulating state, the magnitude of the CMR effect or the observed transition temperatures.

Later theoretical models became more refined. Millis *et al*. considered spin correlations and the effects of electron-phonon coupling arising from the Jahn-Teller splitting of the manganese 3d levels [20]. They estimated the Curie temperature to be roughly 3000 K for $La_{0.825}Sr_{0.175}MnO_3$. This was an order of magnitude above the experimentally observed value of 283 K [21].

Röder *et al*. also considered lattice effects [22]. They postulated that some of the potential carriers were localised on certain Mn^{3+} ions by a lattice distortion. Since previous models had assumed that the level of carriers was set by the level of doping, this polaron self-trapping could explain the discrepancy in the predicted and observed values of T_C. Hall effect measurements on $La_{0.7}Ca_{0.3}MnO_3$ have revealed that the carrier density at 300 K is much reduced (as low at 10^{-2} per formula unit) [23]. Further investigations on single crystals [24] and films [25] report a good agreement with the DE model renormalised by the electron-phonon interaction [26]. However, recent studies have produced evidence from energy-loss spectra [27] and theoretical calculations [28] that the holes in manganites are preferentially found on oxygen ions. In this case, the origin of ferromagnetism has been hypothesised to be direct exchange between these holes [29].

2.2.3.2 Superexchange

In superexchange, the magnetic interaction between adjacent ions is mediated by an intermediate non-magnetic ion with a closed shell. This is a common interaction in the insulating magnetic oxides where the intermediate ion is O^{2-}. The basic interaction mechanism is as follows. If two orbitals on adjacent ions point towards each other, with one orbital fully occupied and the other orbital having a vacancy, then the electron will spend part of its time in the empty orbital on the other ion. For the case of the manganites, the orbitals involved are the vacant Mn e_g orbital and the occupied O 2p orbital, and so it is the O 2p electron that is 'shared' between the two ions. This *virtual transfer* of the electron is what characterises superexchange.

Superexchange can lead to either a ferromagnetic or an antiferromagnetic alignment of the spins, depending on the occupancy of the Mn orbitals, as depicted in Figure 2.11. There is strong Hund coupling between the core Mn t_{2g} spins and any e_g electron(s). There are two cases to consider, namely when the Mn e_g orbital has one permanent electron (Mn^{3+}) and occasionally the virtual electron, or only the virtual electron (Mn^{4+}). For Mn^{3+} the t_{2g} and permanent e_g electron will be spin-aligned (Hund's rules), so the spin of the transferred electron has to have the opposite sign, as

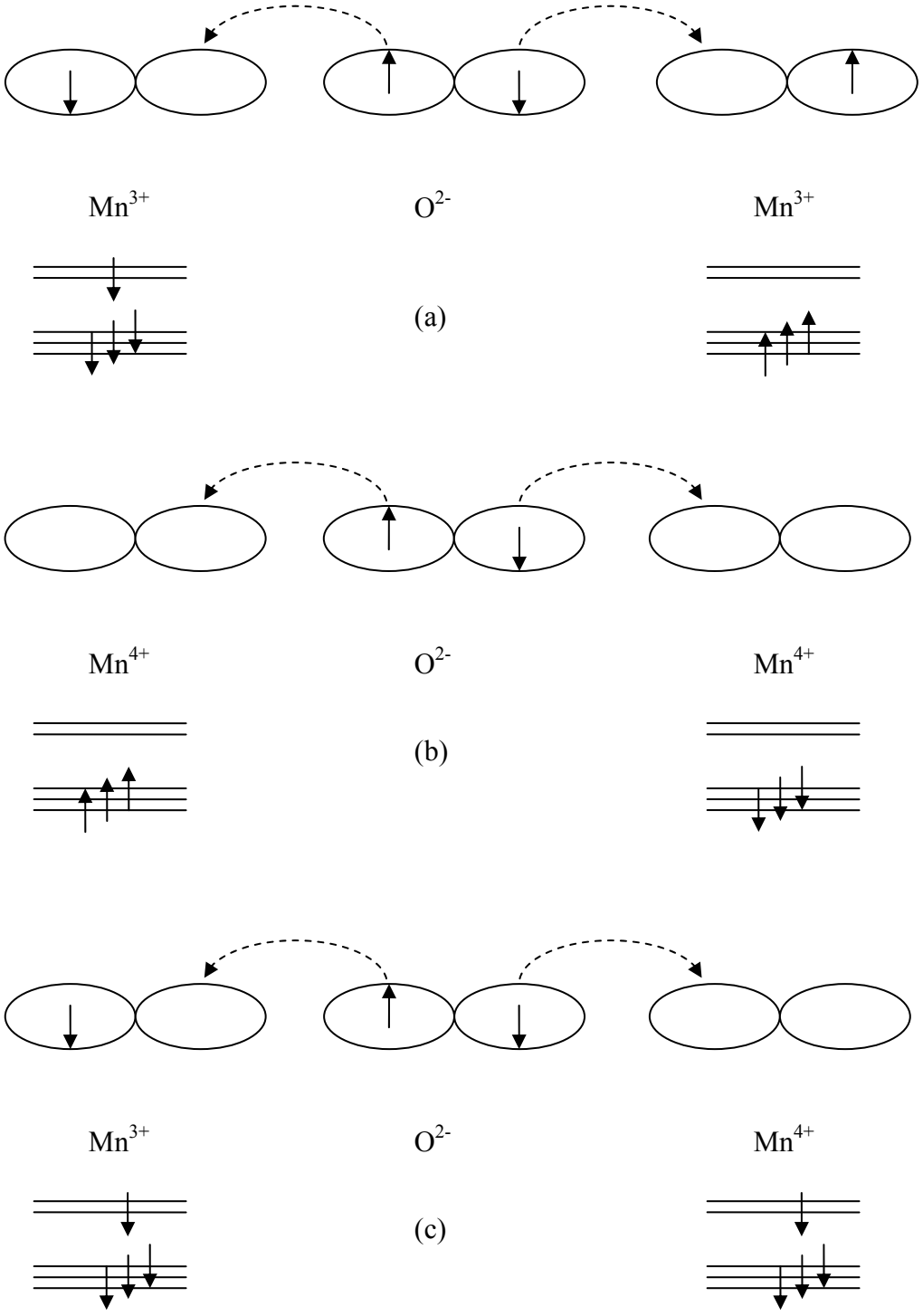

Figure 2.11. Schematic diagram showing the arrangement of spins and orbitals in superexchange. The orbitals involved are the Mn e_g and O 2p, and the dashed arrows represent the virtual transfer of the electron between these orbitals. This means that the electron is located on the oxygen ion for the majority of the time, but can be found in the manganese orbital indicated by the arrow. The three panels result in an (a) antiferromagnetic, (b) antiferromagnetic and (c) ferromagnetic arrangement of the core manganese spins respectively.

required by the Pauli Exclusion Principle. Conversely, for Mn^{4+}, the electrons in the Mn t_{2g} orbitals align with the virtual electron from the oxygen ion.

By applying these two rules and noting that the two electrons from the O 2p orbital have opposite spins, we find that two adjacent empty Mn orbitals or two half-full orbitals will lead to antiferromagnetic order, whereas an empty Mn orbital pointing towards a half-full one will lead to a ferromagnetic alignment of the core Mn spins. However, unlike double exchange, superexchange always results in an insulating state.

2.3 The phase diagram for $La_{1-x}Ca_xMnO_3$

The bandwidth of the general manganite $R_{1-x}A_xMnO_3$ can be altered by varying the R and A cations. Of all the combinations studied in the literature, $La_{1-x}Ca_xMnO_3$ has attracted the most interest due to its intermediate bandwidth and it appears to remain orthorhombic for all values of x. This permits a wide range of phases to be stable. Furthermore, the polaronic and therefore insulating nature of the paramagnetic phase leads to a significant CMR effect. $La_{1-x}Sr_xMnO_3$, has a larger bandwidth and the high-temperature paramagnetic phase is metallic (i.e. $d\rho/dT < 0$). This results in a smaller CMR effect than for $La_{1-x}Ca_xMnO_3$. In contrast, the ferromagnetic state in the narrow-bandwidth manganite $Pr_{1-x}Ca_xMnO_3$ is not easily stabilised. It was for this reason that $La_{1-x}Ca_xMnO_3$ was used in this study.

The competing phases in $La_{1-x}Ca_xMnO_3$ have similar free energies and can coexist in equilibrium with each other. Figure 2.12 shows a simple phase diagram as a function of x and temperature for bulk $La_{1-x}Ca_xMnO_3$ [30], but these are by no means the only parameters which affect the ground state. It should be noted that the diagram shown in Figure 2.12 refers to the bulk polycrystalline material. The phase diagram for epitaxial thin films may differ from this due to the additional effects of substrate-induced strain in the film and may also depend on the thickness of the film. Figure 2.12 also presents an idealised picture by depicting the phase boundaries as sharp lines and omitting any coexistence regions. From just considering the symmetry requirements of each phase, there is no reason why both the ferromagnetic and charge-ordered phases cannot coexist in equilibrium. This was observed previously by Levy *et al*. in bulk polycrystalline $La_{0.5}Ca_{0.5}MnO_3$ with varying grain

sizes [31]. Then in 2002, Loudon, Mathur and Midgley reported a phase that was both ferromagnetic and charge-ordered in a bulk sample of $La_{0.5}Ca_{0.5}MnO_3$ at 90 K, which added further complexity to the x=0.5 low-temperature boundary [32]. These two results, and phase coexistence in general will be discussed in more detail in Chapter 3.

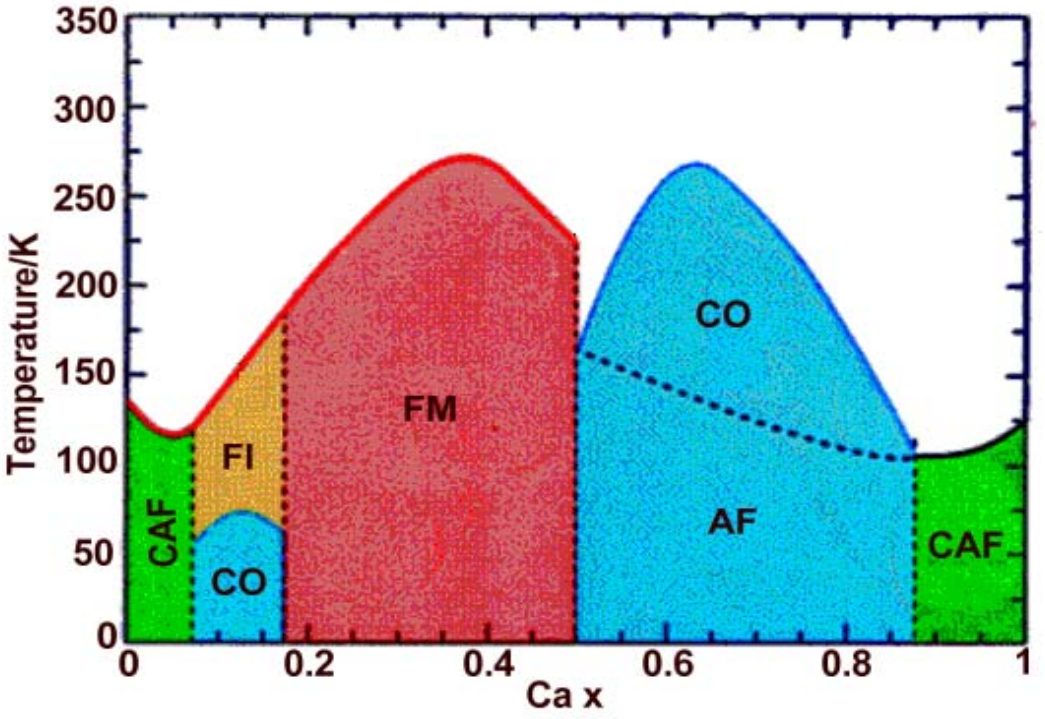

Figure 2.12. A simple phase diagram for polycrystalline $La_{1-x}Ca_xMnO_3$ due to Cheong and Hwang [30]. The white high temperature phase is a paramagnetic insulator (PMI) for all values of x. The coloured regions correspond to a canted antiferromagnet (CAF), ferromagnetic insulator (FI), charge-ordered state (CO), ferromagnetic metal (FM) and antiferromagnet (AF) respectively.

As the level of calcium doping x is increased a wide variety of electrical and magnetic phases is encountered, and these are summarised below. To a first approximation, the doping level and the temperature are the dominant factors in determining the electronic and magnetic properties of $La_{1-x}Ca_xMnO_3$. It should be noted that the ferromagnetic metal and the antiferromagnetic insulator are the most significant phases for this study.

2.3.1 0<*x*<0.1 Antiferromagnetic insulator

In $LaMnO_3$ (x=0) there are four 3d electrons on every manganese ion. The hopping of the itinerant e_g electron is restricted by the on-site Coulomb repulsion and the strong Hund coupling. The e_g electrons interact with each other by virtual hopping onto neighbouring atoms when their spins are antiparallel. This superexchange interaction leads to antiferromagnetic order and $LaMnO_3$ is therefore an antiferromagnetic insulator. Woolan and Koehler found the antiferromagnet lattice was A-type [5], in which the spins are ferromagnetically aligned within each *a*-*b* plane and adjacent planes are coupled antiferromagnetically. As x is increased the magnetic moment increases slightly. It is not clear whether this is due to a canted spin state or phase separation and there is no agreement as to the actual magnetic structure.

2.3.2 0.1<*x*<0.2 Ferromagnetic insulator – charge ordered insulator

In this range, two transitions are seen on cooling. The first transition, at about 120-170 K, is into a ferromagnetic insulating state. The fact that it is insulating means that the ferromagnetism is not caused by double exchange. The magnetic interactions are thought to be due to superexchange. The second transition, which occurs at 80 K, is ascribed to charge-ordering [33], However, charge-ordering does not necessarily imply a magnetic transition and the anomaly at 80 K has also been linked to domain wall pinning effects [34].

X-ray measurements on single crystals have shown that, as x increases towards 0.2, the coherent Jahn-Teller distortions, originating from d-orbital ordering, become suppressed and an orbitally *disordered* state is entered [35]. Orbital ordering is not compatible with metallicity so the ferromagnetic insulating phase is bounded by the limit of coherent Jahn-Teller distortions. This limit occurs at lower levels of Ca doping as the temperature is increased and therefore the phase boundary is not vertical on a plot of temperature versus calcium doping.

2.3.3 0.2<*x*<0.5 Ferromagnetic metal

For 0.2<x<0.5 the low-temperature ground state in the bulk material is a ferromagnetic metal (FM). If the crystal structure is close enough to the ideal cubic perovskite structure then the Mn-O-Mn bonds will be sufficiently linear. This leads to

good orbital overlap and a high probability of hopping and the charge carriers become a delocalised electron gas. The distinction between Mn^{3+} and Mn^{4+} ions is lost, and the Jahn-Teller distortions are reduced.

For the bulk material at x=0.5 two transitions are seen on cooling. A FM state is initially entered at around 230 K. At lower temperatures, there is a transition to an antiferromagnetic state. The Néel temperature is approximately 135 K on cooling and 185 K on warming [36]. This thermal hysteresis is typical of a first-order phase transition in the presence of pinning. Additionally, phase coexistence between FM and CO phases has been seen in bulk samples of $La_{0.5}Ca_{0.5}MnO_3$ [31] and a charge-ordered ferromagnetic phase was observed at 90 K in $La_{0.5}Ca_{0.5}MnO_3$ [32]. It therefore appears that the low-temperature boundary between the FM and AF phases is not sharp and there is a mixed-phase region around x=0.5.

2.3.4 0.5<x<0.9 Charge-ordered insulator

For the bulk material, values of x in the range 0.5<x<0.9 give a charge-ordered (CO) insulator as the low-temperature ground state. It was originally thought that in a CO state the Mn^{3+} and Mn^{4+} ions arranged themselves into two distinct sub-lattices and this resulted in a series of 'stripes' of the two types of ions [37]. The periodicity of the stripes is then determined by the ratio x:1-x, which is itself set by the composition. When this ratio is an integer (e.g. for x= 1/2, 2/3, 3/4, 4/5 etc.) the theory predicted a regular arrangement of Mn^{3+} and Mn^{4+} ions where the superlattice periodicity would be an integer multiple of the crystal lattice. An example of a regular striped array for $La_{0.33}Ca_{0.67}MnO_3$ is given in Figure 2.13.

For other levels of doping it was initially thought that there would be an array of Mn^{3+} and Mn^{4+} ions corresponding to the nearest 'special' composition, but with periodic 'stacking faults' comprising extra planes of one type of Mn ion to obtain the correct chemical composition [38]. Then in 2003, Loudon *et al.* used electron microscopy to probe samples of $La_{0.48}Ca_{0.52}MnO_3$ [39]. The expected distance between stacking faults at this composition is 9.6 nm if the sub-units correspond to x=1/2 and x=2/3, or 6.8 nm with alternate planes of Mn^{3+} and Mn^{4+} ions. With a convergent beam electron diffraction (CBED) probe with a 3.6 nm width they

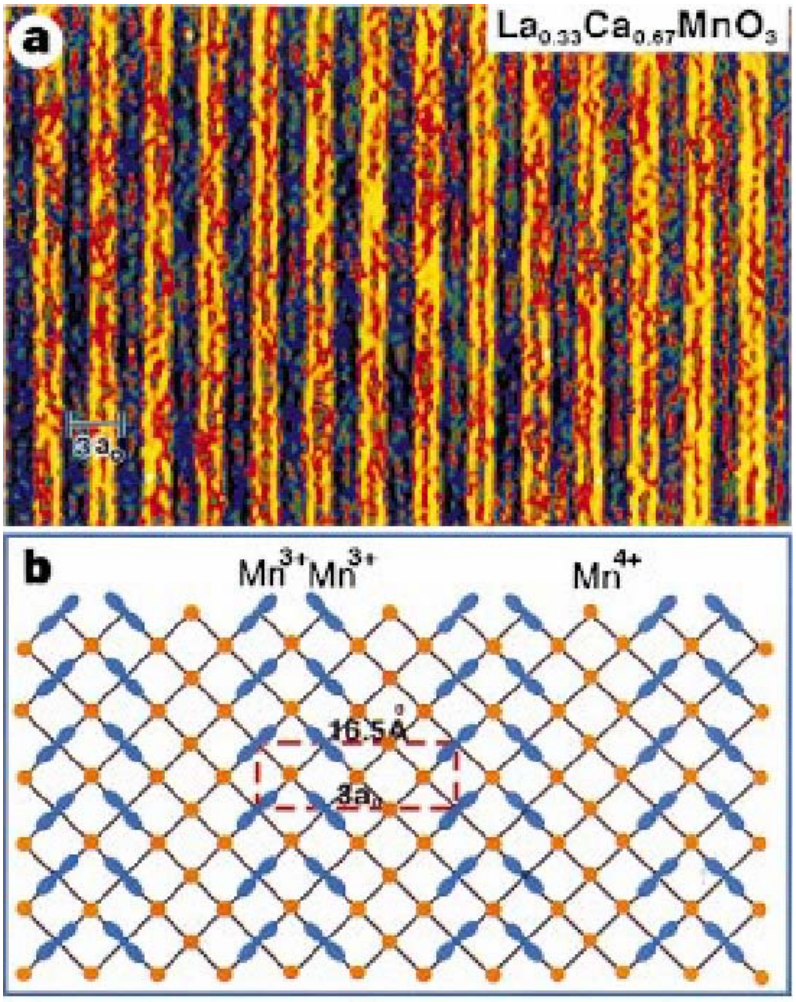

Figure 2.13. (a) A high-resolution electron diffraction image at 95 K showing the pairing of stripes in $La_{0.33}Ca_{0.67}MnO_3$. The periodicity is 3 times the lattice constant. (b) A schematic picture showing the arrangement of the occupied Mn^{3+} (blue) and Mn^{4+} (orange) orbitals. (Taken from [38].)

observed a modulation vector q/a^*=0.473±0.005, which agreed well with the value of q/a^*=0.468±0.003 obtained from a single grain with a selected area aperture, as measured in the object plane, of 500 nm. Crucially they did not observe a modulation vector of q/a^*=0.5 with the smaller probe, which would correspond to orbitally ordered alternating Mn^{3+} and Mn^{4+} planes. Furthermore, the diffraction peaks obtained from large area scans were sharp compared with those obtained from simulations that included the presence of stacking faults. If this result is accurate, then the distinction between Mn^{3+} and Mn^{4+} ions appears to be lost and the low-temperature state for $0.5<x<0.9$ cannot be considered to be 'charge-ordered'. Instead, there could be a small-amplitude charge density wave throughout the crystal.

However, in order to be consistent with the literature, this development will be ignored and the phase will be referred to as 'charge-ordered' in this dissertation.

There is an additional transition on further cooling, in which the manganese spins align themselves in an anti-parallel arrangement to form an antiferromagnet. This occurs in the range 100-150 K and the Néel temperature T_N depends on the level of calcium doping. Neutron studies suggest that this phase is a CE type antiferromagnet with a checkerboard arrangement of spins [5].

Charge ordered samples have been reported for many different manganites in the bulk form. The two most common experimental techniques for observing CO are via superlattice reflections in electron diffraction patterns [40,41] and resistivity measurements [31,42]. If the conduction mechanism in the insulating paramagnetic and charge-ordered phases is due to thermally activated carriers, then the activation energy should be different for the two phases. A transition from the paramagnetic to charge-ordered states would then show up via a sudden change of gradient in the logarithm of resistance versus temperature. Charge-ordering has also been seen in real space via atomic resolution scanning tunnelling microscopy [43].

It is possible to 'melt' the charge ordered phase by applying an external magnetic field. A 25 T field was required to melt fully the charge-ordered state seen in bulk $Pr_{0.5}Ca_{0.5}MnO_3$ and induce metallic behaviour [44]. The melting of the CO state can result in the highest MR values, e.g. a change of 10 orders of magnitude ($\Delta\rho/\rho(3\text{ T})=10^{12}\%$) was seen at 40 K in a $Pr_{0.67}Ca_{0.33}MnO_3$ single crystal [45].

In contrast to the bulk material, there were few reports until recently of charge order in any manganite thin films. One of the earliest was in 1999, when Prellier *et al*. inferred a charge ordered state from resistivity measurements in 50 nm and 200 nm epitaxial films of $Nd_{0.5}Sr_{0.5}MnO_3$ grown on $LaAlO_3$ [46]. The charge-ordering temperature T_{CO} was 170 K. Rather surprisingly, the 200 nm film showed metallic behaviour at lower temperatures. A 20 nm film remained insulating at all temperatures and did not charge-order. These results suggest that strain and film thickness are critical in determining film properties. More recently, the first direct evidence of charge ordering in a manganite film was reported when superlattice reflections were seen below 170 K in a $La_{0.50}Ca_{0.50}MnO_3$ film on $NdGaO_3$ [47].

Furthermore, the size of the wavevector was found to be 3% smaller in a stress-free rectangle produced by focussed ion beam milling than in the remainder of the film.

2.3.5 0.9<*x*<1 Antiferromagnetic insulator

The end-member $CaMnO_3$, like $LaMnO_3$, is an antiferromagnetic insulator. Woolan and Koehler found that $CaMnO_3$ was a G-type antiferromagnet [5], in which every spin is antiparallel to its nearest neighbours. Again, there is uncertainty as to whether there is phase separation or canted spins for values of x just below 1. Note that all the manganese ions at x=1 are Mn^{4+} and, as such, there will be no Jahn-Teller distortions.

2.3.6 High-temperature phase - paramagnetic insulator

For all values of x the various low-temperature phases seen in $La_{1-x}Ca_xMnO_3$ eventually give way on warming to a paramagnetic insulating (PMI) state when the entropy increase caused by randomising the atomic manganese spins outweighs the associated increase in magnetic interaction energy. In the PMI phase the extra e_g electrons on the Mn^{3+} ions are arranged at random throughout the lattice. The Mn^{3+} ions that result can lower their energy by undergoing a Jahn-Teller distortion (see Section 2.2.2 for more details on the Jahn-Teller distortion). This leads to a coupling between the Jahn-Teller distortions and the e_g electrons. The paramagnetic state in $La_{1-x}Ca_xMnO_3$ is effectively a polaronic liquid that is insulating. In contrast, the high temperature paramagnetic phase in the similar compound $La_{1-x}Sr_xMnO_3$ is metallic. This difference is due to the larger bandwidth in $La_{1-x}Sr_xMnO_3$. The Sr^{2+} ion is larger than Ca^{2+}, which alters the degree of electron-lattice coupling and increases the bandwidth.

For bulk $La_{1-x}Ca_xMnO_3$ the paramagnetic state occurs above 200-265 K, although the transition temperature depends on the value of x. The maximum Curie temperature reported for the bulk material was 265 K for x=0.375 [8]. However, a thin film of $La_{0.8}Ca_{0.2}MnO_3$ on $LaAlO_3$ (001) grown by Shreekala *et al.* had a reported T_C of 280 K [48], which is the highest reported Curie temperature for any composition and type of sample (polycrystalline, bulk single crystal or thin film) in the $La_{1-x}Ca_xMnO_3$ system. $LaAlO_3$ is a substrate that has slightly smaller lattice parameters than $La_{0.8}Ca_{0.2}MnO_3$, so the film will be compressively strained in-plane.

$LaAlO_3$ is also prone to forming twins, and this makes it unsuitable for studying intrinsic effects.

2.3.7 Conduction in the high-temperature paramagnetic phase

The method of conduction in the high-temperature paramagnetic phase is not well understood. The electrical transport properties of the material depend on the bandwidth, e.g. in $La_{1-x}Sr_xMnO_3$ the relatively large bandwidth results in a metallic paramagnetic state, whereas a smaller bandwidth, as seen in $La_{1-x}Ca_xMnO_3$, generally leads to a paramagnetic insulating state. The insulating state in $La_{1-x}Ca_xMnO_3$ has a well-defined activation energy E_a in the range 0.1-0.25 eV [49]. Furthermore, the activation energy has been shown to increase with increasing Mn-O bond length and decreasing Ca doping from the optimal value [49]. Thus, it seems that the behaviour above T_C depends solely on the bandwidth.

There are three possible mechanisms for conduction in the paramagnetic phase with each model supported by some experimental evidence. The possible mechanisms are a thermally activated model [50], a nearest neighbour hopping model [51] and a variable range hopping (VRH) model [52]. All of the experimental observations have been carried out in a narrow temperature range just above T_C and it has been difficult to distinguish these three mechanisms from each other over a narrow temperature range. Consequently, there is no agreement as to the actual mechanism. Measurements over a wider temperature range are required to provide further insight into the nature of the electrical transport. Each of the three mechanisms is discussed in turn below.

2.3.7.1 Thermally activated carriers

In this model, the carriers are thermally excited across the band-gap from the valence band to the conduction band. The resistivity ρ will follow the Boltzmann law and result in equation 2.4 where E_g is the energy gap and ρ_∞ is the resistivity as the temperature tends to infinity.

$$\rho = \rho_\infty \exp\left(\frac{E_g}{kT}\right) \tag{2.4}$$

This simple Arrhenius model is potentially a crude assumption. The resistivity is given by $\rho=(ne\mu)^{-1}$ where n is the carrier density in the conduction band, e is the charge of an electron and μ is the carrier mobility. The dominant factor is normally the thermally activated form of n, and μ is assumed to be independent of temperature. It would be reasonable for the mobility to show some temperature dependence, which would introduce additional factors into equation 2.4.

2.3.7.2 Nearest-neighbour hopping

The e_g electrons in the paramagnetic state are thought to have a lattice distortion associated with them (i.e. they form a polaron) and electrical conduction proceeds via the movement of these polarons. In this model, the lattice distortions are of a similar size to a unit cell, and the polarons move a distance a between nearest neighbour sites. The energy required to move the polaron is E_p so the probability P of an electron hopping is

$$P = \frac{\exp(-E_p / kT)}{1+\exp(-E_p / kT)} \approx \exp(-E_p / kT)\,. \qquad (2.5)$$

The final step in equation 2.5 assumes that $E_p/kT \ll 1$. If the polaron attempts to hop with a frequency ω that is much faster than the lattice vibrations (the so-called adiabatic limit) then the chance of hopping per unit time is given by $\omega\exp(-E_p/kT)$. The polarons then diffuse through the crystal with a diffusion coefficient D given by

$$D = \frac{a^2\omega}{6}\exp\left(\frac{-E_p}{kT}\right), \qquad (2.6)$$

where a is the hopping distance. By using the Einstein relation $\mu=eD/kT$ and $\rho=(ne\mu)^{-1}$, the resistivity is given by equation 2.7, where A is a constant.

$$\rho = AT\exp\left(\frac{E_p}{kT}\right) \qquad (2.7)$$

However, the strong electron-phonon coupling seen in the $La_{1-x}Ca_xMnO_3$ system means that the motion of the charge-carriers is slow compared with the lattice vibrations. The motion of the electrons and the lattice cannot be separated and the

analysis for the adiabatic limit is no longer valid. In the nonadiabatic limit the analysis is more complicated [53] and the drift mobility is found to be

$$\mu = AT^{-3/2} \exp\left(\frac{E_p}{kT}\right). \tag{2.8}$$

The resistivity in the nonadiabatic limit is then obtained from the relationship $\rho=(ne\mu)^{-1}$ and is given by equation 2.9, in which A' is a constant.

$$\rho = A'T^{3/2} \exp\left(-\frac{E_p}{kT}\right) \tag{2.9}$$

2.3.7.3 Variable range hopping

If the activation energies for hopping to neighbouring atoms are not the same, then it may be that hopping to a non-nearest neighbour has a smaller activation energy. This is particularly true at low temperatures [54]. This variable range hopping is potentially more complicated to describe quantitatively, but the following derivation due to Mott is seen to work [53].

Within a radius R of an atom at the Fermi surface there will be $N=(4/3)\pi R^3 n(E_F)\Delta E$ accessible states where $n(E_F)$ is the number density of states at the Fermi level and ΔE is the range of available energy states. If the electron hops a distance R then the lowest activation energy available to it is

$$\delta E = \frac{\Delta E}{N} = \frac{3}{4\pi R^3 n(E_F)}. \tag{2.10}$$

However, hopping over a large distance requires quantum mechanical tunnelling, so the probability of hopping contains a factor of $\exp(-2\alpha R)$, where $1/\alpha$ is the decay length of the localised wavefunction. The overall hopping probability is proportional to

$$P \propto \exp(-2\alpha R)\exp(-\delta E / kT). \tag{2.11}$$

Minimisation of equation 2.11 with respect to R gives $R \propto T^{-1/4}$. By substituting this expression into equations 2.10 and 2.11 and using the fact $\rho \propto P^{-1}$ the resistivity is

then found to be

$$\rho = \rho_{\infty} \exp\left(\frac{T_0}{T}\right)^{1/4}, \qquad (2.12)$$

where T_0 is a characteristic temperature. One drawback of this model is that the values of T_0 are often implausibly high, e.g. 1.6×10^8 K for polycrystalline $La_{0.29}Ca_{0.71}MnO_3$ in the charge-ordered region [55]. Another drawback with VRH is that it was originally proposed for short distance hopping at low temperatures.

There is a further complication in that the mechanism may depend on the type of sample (single crystal, polycrystalline, or thin film). Ziese *et al.* found that polycrystalline films of $La_{0.7}Ca_{0.3}MnO_3$ obeyed a variable range hopping measurement [17]. The same group reported that the resistance of epitaxial $La_{0.7}Ca_{0.3}MnO_3$ films showed thermally activated behaviour. This discrepancy is probably due to the presence of grain boundaries in the polycrystalline sample.

2.4 Oxygenation of samples

Any oxygen vacancies present in the lattice will lead to small off-stoichiometries. As a result, there is often a slight difference between the fraction of Mn^{4+} ions and the fraction of divalent ions present. During film deposition, there will be an equilibrium between gaseous oxygen and oxygen vacancies.

$$O^{2-} \leftrightarrow \tfrac{1}{2}O_2 + 2e^- + vacancy \qquad (2.13)$$

Thus, a low oxygen partial pressure during deposition will lead to additional vacancies being formed. To combat any effects of a low oxygen partial pressure during deposition, samples grown as described in Chapter 4 were always annealed *in-situ* to promote full oxygenation. If the chemical formula is written as

$$(La^{3+})_{1-x}(Ca^{2+})_x(Mn^{3+})_{1-y}(Mn^{4+})_y(O^{2-})_{3-\delta}, \qquad (2.14)$$

where δ is the number of oxygen vacancies per formula unit, then conservation of charge leads to the relationship

$$y = x - 2\delta. \qquad (2.15)$$

The number of potentially itinerant electrons, which are associated with Mn^{3+} ions, is therefore proportional to 1-*y*. The number of oxygen vacancies and the level of divalent atom doping have opposing effects on the number of potential carriers, with an increase in oxygen vacancies increasing the carrier density. It has been reported that $La_{0.7}Ca_{0.3}MnO_3$ is stable for values of δ up to δ=0.05±0.005 [56]. Above this value, this compound decomposed. It should be noted that excess oxygen is manifested as cation vacancies and will decrease the number of potential carriers [57].

There have been numerous studies on the effects of annealing manganite samples, most of which report an improvement in the properties after annealing in oxygen. For example, Prellier *et al.* saw an increase in T_C from 240 K in an as-grown film of $La_{0.75}Ca_{0.25}MnO_3$ to 270 K after subsequent oxygen annealing [58], and a similar increase (250 K to 280 K) in T_{MI}. It is also possible to reduce the oxygen content by annealing in a reducing atmosphere of nitrogen [59] or under vacuum [60], although previous studies have shown that very low oxygen partial pressures and high temperatures, as shown in Figure 2.14, were required to alter the oxygen content significantly [61]. However, the metal-insulator transition temperature for $La_{0.7}Ca_{0.3}MnO_3$ films on $LaAlO_3$ was sensitive to the oxygen partial pressure during annealing, as shown in Figure 2.15.

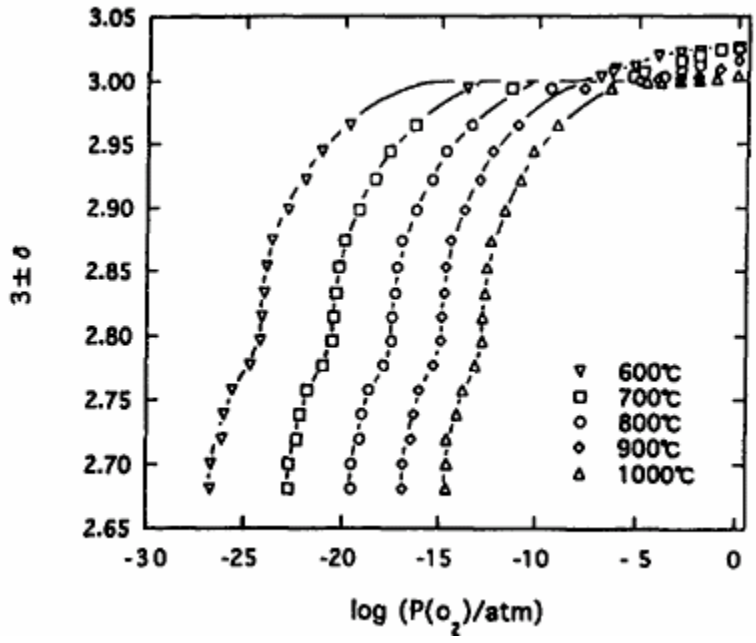

Figure 2.14. Reduction in oxygen content after annealing for $La_{0.7}Sr_{0.3}MnO_3$ films. (Taken from [61].)

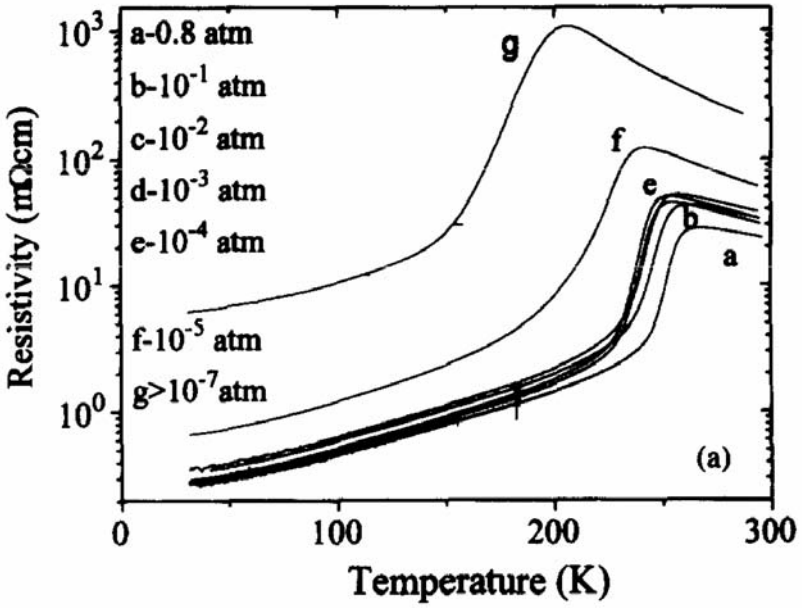

Figure 2.15. Temperature dependence of resistivity for $La_{0.7}Ca_{0.3}MnO_3$ films after annealing under various oxygen partial pressures. (Taken from [61].)

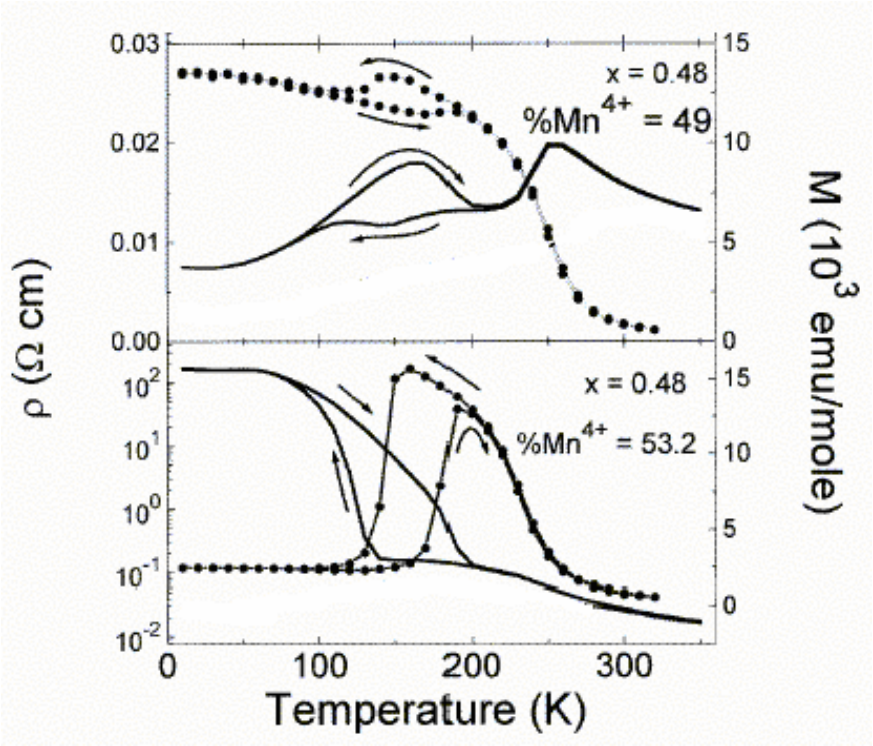

Figure 2.16. The two panels show ρ(T) in B=0 (solid markers) and M(T) for B=1 T (solid lines) for two polycrystalline samples of $La_{1-x}Ca_xMnO_3$ with x=0.48 but different concentrations of Mn^{4+} ions. (Adapted from [62].)

Roy *et al.* performed a systematic study on polycrystalline samples of $La_{1-x}Ca_xMnO_3$, concentrating on the region near x=0.5 [62]. They found discrepancies between the numbers of Mn^{4+} ions and the notional carrier content, as predicted by the calcium content, which were attributed to oxygen vacancies. The resulting sample properties could not be predicted by either solely the Ca content or the number of Mn^{4+} ions, but a combination of the two. This was especially relevant close to the low-temperature boundary between the FM and AF states. Figure 2.16 illustrates the differences in electrical and magnetic properties between two polycrystalline $La_{1-x}Ca_xMnO_3$ samples with x=0.48 but differing percentages of Mn^{4+} ions.

Additionally, it seems that the onset of ferromagnetism can be influenced by the oxygen isotope mass [63]. Partial replacement of ^{16}O with ^{18}O was shown to reduce T_C, which was attributed to the reduced amplitude of positional oscillations for the heavier ^{18}O ion. From this, it seems that the transport in the metallic state depends on

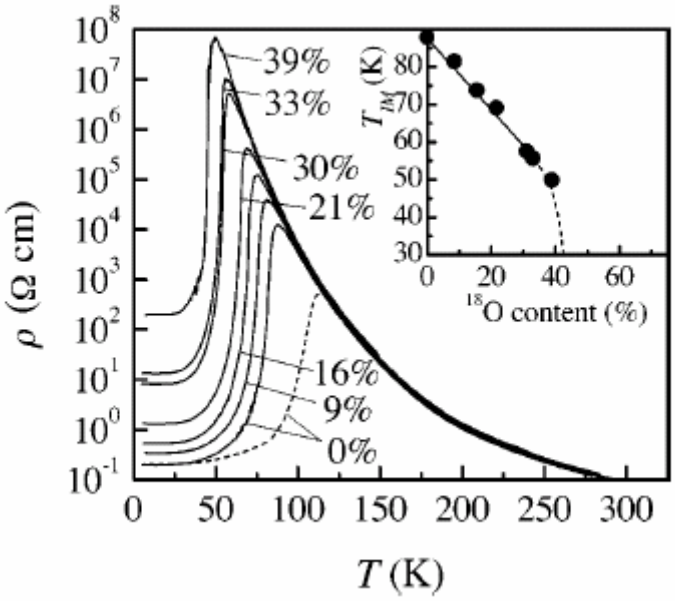

Figure 2.17. Temperature dependence of resistivity for $(La_{0.25}Pr_{0.75})_{0.7}Ca_{0.3}MnO_3$ samples with different percentages of ^{18}O. The solid curves are for cooling, and the dashed line for 0% ^{18}O on warming is given to illustrate the hysteresis. Inset: Metal-insulator transition temperature (taken to be the inflection point in $\rho(T)$) as a function of oxygen content. (Taken from [64].)

the dynamics of the oxygen ions, which would not be the case for a theory where static Jahn-Teller distortions cause the ferromagnetic transition in combination with double exchange. Babushkina *et al.* also reported a dependence on oxygen isotope [64]. They found that introducing ^{18}O into bulk samples of $(La_{0.25}Pr_{0.75})_{0.7}Ca_{0.3}MnO_3$ increased the resistivity and reduced T_C, as shown in Figure 2.17. Furthermore, for low levels of ^{18}O there was an appreciable ferromagnetic signal, whereas above 60% ^{18}O the magnetic behaviour was typical of an antiferromagnet. This behaviour suggested a percolation-type phase-separated system, with a mixture of a FM metal and an AF insulator.

2.5 Thin film manganites and the effect of strain

If the lattice parameters of the film and substrate are sufficiently well matched, then the film should grow epitaxially, i.e. the in-plane lattice parameters of the film should match those of the substrate. Epitaxial growth of thin films will lead to an in-plane strain (either tensile or compressive) in the film that is likely to alter the film properties, as the electron-lattice interaction in the manganites is particularly crucial. Theoretical calculations predict that a lattice mismatch of 1% will reduce T_C by 10% [65]. It is possible to have an epitaxial strain of over 1%, e.g. $La_{0.7}Ca_{0.3}MnO_3$ grown on $SrTiO_3$ (001), and a wide range of values for T_C (75-280 K) is observed. Various studies have shown that the substrate [66], film thickness [46,66] and coherency of strain [67,68] can all influence the transition temperature and even the ground state itself [69]. Figure 2.18 shows resistivity ρ versus temperature curves for $La_{0.67}Sr_{0.33}MnO_3$ films of varying thickness and grown on different substrates. The resistivity decreased as the film thickness increased. Furthermore, for films of the same thickness, ρ was smaller for films deposited on $NdGaO_3$ (lattice mismatch 0.83%) than for those deposited on $LaAlO_3$ (mismatch -1.9%). In particular, the 1.5 nm thick film on $LaAlO_3$ had a significantly enhanced resistivity below 150 K.

The resistivity for the films on $LaAlO_3$ will be artificially enhanced by twin boundaries. In the absence of this effect, the resistivity for the films on $LaAlO_3$ should be lower than for the films on $NdGaO_3$, as the compressive in-plane stain for films on $LaAlO_3$ will reduce the in-plane Mn-O-Mn bond length and promote ferromagnetism. Conversely, the out-of-plane bond length will be longer, thereby

reducing the hopping probability and inhibiting metallicity in the direction normal to the film surface. The anisotropic nature of the resistivity was investigated by Klein *et al.* [70], who found metallic behaviour in-plane but insulating behaviour and non-linear current-voltage characteristics perpendicular to the film. However, this effect is ignored by most authors.

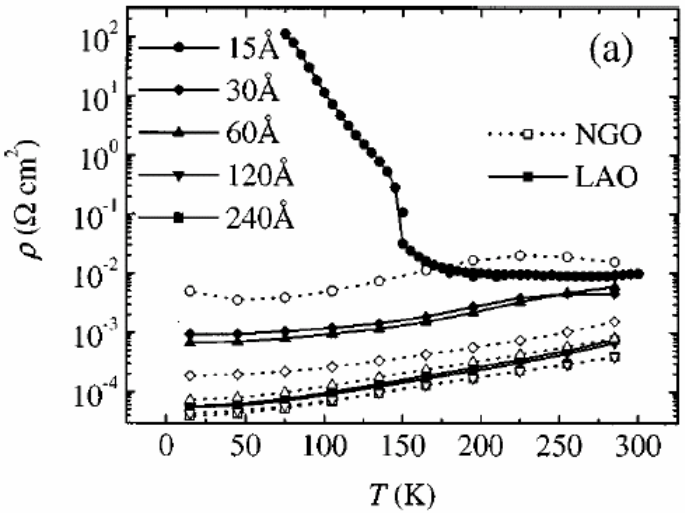

Figure 2.18. Temperature dependent resistivity for $La_{0.67}Sr_{0.33}MnO_3$ films of different thicknesses on $NdGaO_3$ (NGO) and $LaAlO_3$ (LAO). Note that bulk $La_{0.67}Sr_{0.33}MnO_3$ has a T_C above 300 K. (Taken from [66].)

2.5.1 Crystal symmetry

The end members of the $La_{1-x}Ca_xMnO_3$ series, namely $LaMnO_3$ (x=0) and $CaMnO_3$ (x=1), both have orthorhombic *Pnma* crystal symmetry. To a first approximation as we increase the calcium fraction the pseudo-cubic lattice parameter varies linearly between the two end values (Vegard's Law). All of the substrates used in this study have crystal structures that lead to a pseudo-cubic lattice parameter similar to that of $La_{1-x}Ca_xMnO_3$. This is especially true around x=0.5. Thus, there should be a high degree of epitaxy in the films. Table 2.1 shows the lattice parameters and crystal symmetry of the substrates used in this study and for certain compositions in the $La_{1-x}Ca_xMnO_3$ series.

If a film is compressively strained in the in-plane direction then there will be an associated tensile strain in the direction perpendicular to the film surface and vice versa. If we can assume that the film is epitaxial, then the out of plane strain ε_{zz} will

Compound	Crystal Symmetry	Lattice parameter / Å		
$SrTiO_3$	Cubic	*a*=3.905		
$NdGaO_3$	Orthorhombic *Pbnm*	*a*=5.4322	*b*=5.5034	*c*=7.7155
$LaAlO_3$	Rhombohedral	*a*=5.3648	*c*=13.1113	
$LaMnO_3$	Orthorhombic *Pbnm*	*a*=5.5367	*b*=5.7473	*c*=7.6929
$La_{0.6}Ca_{0.4}MnO_3$	Orthorhombic *Pnma*	*a*=5.4434	*b*=7.6830	*c*=5.4537
$La_{0.5}Ca_{0.5}MnO_3$	Orthorhombic *Pnma*	*a*=5.4182	*b*=7.6389	*c*=5.4269
$CaMnO_3$	Orthorhombic *Pnma*	*a*=5.2819	*b*=7.4547	*c*=5.2658

Table 2.1. Crystal symmetries and lattice parameters for the substrates used in this work, together with data for certain compositions of $La_{1-x}Ca_xMnO_3$. Data is taken from [71].

be related to the two components of the in-plane strain ε_{xx} and ε_{yy} by equation 2.16, in which ν is Poisson's ratio.

$$\varepsilon_{zz} = -\frac{\nu(\varepsilon_{xx} + \varepsilon_{yy})}{1-\nu} \qquad (2.16)$$

For $La_{0.8}Ca_{0.2}MnO_3$ and $La_{0.67}Ca_{0.33}MnO_3$ ν was found to be approximately 0.38 [72,73]. If we can assume that this value applies to the compositions studied here, then the out-of plane strain and lattice parameters can be predicted. It should be noted that, because ν<½, the unit cell volume is reduced compared to the bulk material.

In practice, the film microstructure may not be constant throughout the thickness. This is particularly true for thicker films (above ~100 nm) and films grown on substrates with a greater lattice mismatch. As the thickness increases, the associated strain energy also increases, and, beyond a critical thickness, it becomes energetically favourable for the film to relax by including misfit dislocations. The degree of relaxation will affect the crystal structure of the film and hence the physical properties. Figure 2.19 illustrates how the microstructure varies with the degree of relaxation.

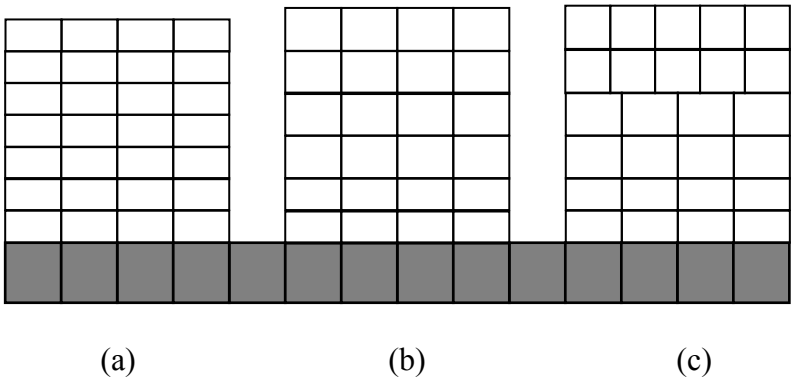

Figure 2.19. Schematic diagram showing the microstructure of an epitaxial film that is (a) coherently strained, (b) partially relaxed and (c) fully relaxed.

Finally it should be noted that the lattice parameter, and hence local strain state, have been shown to vary by up to 0.5% within 1 μm of a grain boundary in a film grown on a $SrTiO_3$ (001) bicrystal substrate [74]. Furthermore, this variation of strain resulted in a 20 K difference in T_C as determined by temperature dependent magnetic force microscopy images [75]. This result emphasises how sensitive the physical properties of the manganites are to strain.

References for Chapter 2

[1] J.H. van Santen and G.H. Jonker, *Electrical conductivity of ferromagnetic compounds of manganese with perovskite structure.* Physica **16**, 599-600 (1950).

[2] G.H. Jonker and J.H. van Santen, *Ferromagnetic compounds of manganese with perovskite structure.* Physica **16**, 337-49 (1950).

[3] C. Zener, *Interaction between the d-shells in the Transition Metals. II. Ferromagnetic Compounds of Manganese with the Perovskite Structure.* Phys. Rev. **82**, 403-5 (1951).

[4] J. Volger, *Further experimental investigations on some ferromagnetic oxidic compounds of manganese with perovskite structure.* Physica **20**, 49-66 (1954).

[5] E.O. Wollan and W.C. Koehler, *Neutron Diffraction Study of the Magnetic Properties of the Series of Perovskite-Type Compounds [(1-x)La, xCa]MnO_3.* Phys. Rev. **100**, 545-63 (1955).

[6] R von Helmolt, J. Wecker, B. Holzapfel, L. Schultz and K. Samwer, *Giant Negative Magnetoresistance in Perovskitelike $La_{2/3}Ba_{1/3}MnO_x$ Ferromagnetic Films.* Phys. Rev. Lett. **71**, 2331-3 (1993).

[7] S. Jin, T.H. Tiefel, M. McCormack, R.A. Fastnacht, R. Ramesh and L.H. Chen, *Thousandfold Change in Resistivity in Magnetoresistive La-Ca-Mn-O Films.* Science **264**, 413-5 (1994).

[8] S.-W. Cheong and C.H. Chen, *Striped Charge & Orbital Ordering in Perovskite Manganites,* in *Colossal Magnetoresistance, Charge Ordering and Related Properties of Manganese Oxides* (Ed. C.N.R. Rao and B. Raveau), World Scientific. p. 241-78 (1998).

[9] M. McCormack, S. Jin, T.H. Tiefel, R.M. Fleming, J.M. Phillips and R. Ramesh, *Very large magnetoresistance in perovskite-like La-Ca-Mn-O thin films.* Appl. Phys. Lett. **64**, 3045-7 (1994).

[10] R.D. Shannon, *Revised Effective Ionic Radii and Systematic Studies of Interatomic Distances in Halides and Chalcogenides.* Acta Crystallogr. A **32**, 751-67 (1976).

[11] L.M. Rodríguez-Martínez and J.P. Attfield, *Disorder-induced orbital ordering in $La_{0.7}M_{0.3}MnO_3$ perovskites.* Phys. Rev. B **63**, 024424 (2000).

[12] W.E. Pickett and D.J. Singh, *Electronic structure and half-metallic transport in the $La_{1-x}Ca_xMnO_3$ system.* Phys. Rev. B **53**, 1146-60 (1996).

[13] J.P. Attfield, *'A' cation control of perovskite properties.* Cryst. Eng. **5**, 427-38 (2002).

[14] H.Y. Hwang, S.-W. Cheong, P.G. Radaelli, M. Marezio and B. Batlogg, *Lattice Effects on the Magnetoresistance in Doped $LaMnO_3$.* Phys. Rev. Lett. **75**, 914-7 (1995).

[15] J. Fontcuberta, B. Martínez, A. Seffar, S. Piñol, J.L. García-Muñoz and X. Obradors, *Colossal Magnetoresistance of Ferromagnetic Manganites: Structural Tuning and Mechanisms.* Phys. Rev. Lett. **76**, 1122-5 (1996).

[16] M. Uehara, S. Mori, C.H. Chen and S.-W. Cheong, *Percolative phase separation underlies colossal magnetoresistance in mixed-valent manganites.* Nature **399**, 560-3 (1999).

[17] M. Ziese and C. Srinitawarawong, *Polaronic effects on the resistivity of manganite thin films.* Phys. Rev. B **58**, 11519-25 (1998).

[18] P.W. Anderson and H. Hasegawa, *Considerations on Double Exchange.* Phys. Rev. **100**, 675-81 (1955).

[19] P.-G. de Gennes, *Effects of Double Exchange in Magnetic Crystals.* Phys. Rev. **118**, 141-54 (1960).

[20] A.J. Millis, P.B. Littlewood and B.I. Shraiman, *Double Exchange Alone Does Not Explain the Resistivity of $La_{1-x}Sr_xMnO_3$.* Phys. Rev. Lett. **74**, 5144-7 (1995).

[21] A. Urushibara, Y. Moritomo, T. Arima, A. Asamitsu, G. Kido and Y. Tokura, *Insulator-metal transition and giant magnetoresistance in $La_{1-x}Sr_xMnO_3$.* Phys. Rev. B **51**, 14103-9 (1995).

[22] H. Röder, J. Zang and A.R. Bishop, *Lattice Effects in the Colossal-Magnetoresistance Manganites.* Phys. Rev. Lett. **76**, 1356-9 (1996).

[23] M.F. Hundley, M. Hawley, R.H. Heffner, Q.X. Jia, J.J. Neumeier, J. Tesmer, J.D. Thompson and X.D. Wu, *Transport-magnetism correlations in the ferromagnetic oxide $La_{0.7}Ca_{0.3}MnO_3$.* Appl. Phys. Lett. **67**, 860-2 (1995).

[24] A.V. Boris, N.N. Kovaleva, A.W. Bazhenov, P.J.M. van Bentum, Th. Rasing, S.-W. Cheong, A.V. Samoilov and N.-C. Yeh, *Infrared studies of a $La_{0.67}Ca_{0.33}MnO_3$ single crystal: Optical magnetoconductivity in a half-metallic ferromagnet.* Phys. Rev. B **59**, R697-700 (1999).

[25] M. Quijada, J. Cerne, J.R. Simpson, H.D. Drew, K.H. Ahn, A.J. Millis, R. Shreekala, R. Ramesh, M. Rajeswari and T. Venkatesan, *Optical conductivity of manganites: Crossover from Jahn-Teller small polaron to coherent transport in the ferromagnetic state.* Phys. Rev. B **58**, 16093-102 (1998).

[26] A.J. Millis, B.I. Shraiman and R. Mueller, *Dynamic Jahn-Teller Effect and Colossal Magnetoresistance in $La_{1-x}Sr_xMnO_3$.* Phys. Rev. Lett. **77**, 175-8 (1996).

[27] H.L. Ju, H.-C. Sohn and K.M. Krishnan, *Evidence for O_{2p} Hole-Driven Conductivity in $La_{1-x}Sr_xMnO_3$ ($0 \leq x \leq 0.7$) and $La_{0.7}Sr_{0.3}MnO_z$ Thin Films.* Phys. Rev. Lett. **79**, 3230-3 (1997).

[28] V. Ferrari, M. Towler and P.B. Littlewood, *Oxygen stripes in $La_{0.5}Ca_{0.5}MnO_3$ from ab initio calculations.* Phys. Rev. Lett. **92**, 227202 (2003).

[29] A.S. Moskvin and I.L. Avvakumov, *Doped manganites beyond conventional double-exchange model.* Physica B **322**, 371-89 (2002).

[30] S.-W. Cheong and H.Y. Hwang, *Colossal magnetoresistance Oxides,* (Ed. Y. Tokura), Gordon & Breach, New York (1997).

[31] P. Levy, F. Parisi, G. Polla, D. Vega, G. Leyva, H. Lanza, R.S. Freitas and L. Ghivelder, *Controlled phase separation in $La_{0.5}Ca_{0.5}MnO_3$.* Phys. Rev. B **62**, 6437-41 (2000).

[32] J.C. Loudon, N.D. Mathur and P.A. Midgley, *Charge-ordered ferromagnetic phase in $La_{0.5}Ca_{0.5}MnO_3$.* Nature **420**, 797-800 (2002).

[33] M. Castro, R. Burriel and S.-W. Cheong, *Magnetic and heat-capacity anomalies of $La_{7/8}Ca_{1/8}MnO_3$.* J. Magn. Magn. Mater. **196-197**, 512-4 (1999).

[34] P.A. Joy and S.K. Date, *On the low-temperarture anomaly in the AC susceptibility of $La_{0.9}Ca_{0.1}MnO_3$.* J. Magn. Magn. Mater. **220**, 106-14 (2000).

[35] B.B. van Aken, O.D. Jurchescu, A. Meetsma, Y. Tomioka, Y. Tokura and T.T.M. Palstra, *Orbital-Order-Induced Metal-Insulator Transition in $La_{1-x}Ca_xMnO_3$.* Phys. Rev. Lett. **90**, 066403 (2003).

[36] J. Dho, I. Kim, S. Lee, K.H. Kim, H.J. Lee, J.H. Jung and T.W. Noh, *Zero-field ^{139}La nuclear magnetic resonance in $La_{1-x}Ca_xMnO_3$ for $0.125 \leq x \leq 0.5$.* Phys. Rev. B **59**, 492-6 (1999).

[37] C.H. Chen, S.-W. Cheong and H.Y. Hwang, *Charge-ordered stripes in $La_{1-x}Ca_xMnO_3$ with $x>0.5$.* J. Appl. Phys. **81**, 4326-30 (1999).

[38] S. Mori, C.H. Chen and S.-W. Cheong, *Pairing of charge-ordered stripes in (La,Ca)MnO_3.* Nature **392**, 473-6 (1998).

[39] J.C. Loudon, S. Cox, A.J. Williams, J.P. Attfield, P.B Littlewood, P.A. Midgley and N.D. Mathur, *Weak charge-lattice coupling requires reinterpretation of stripes of charge order in $La_{1-x}Ca_xMnO_3$.* Phys. Rev. Lett. **94**, 097202 (2005).

[40] T. Asaka, S. Yamada, S. Tsutsumi, C. Tsuruta, K. Kimoto, T. Arima and Y. Matsui, *Charge/Orbital Ordering Structure of $Pr_{1-x}Ca_xMnO_3$ ($x=3/8$) Examined by Low-Temperature Transmission Electron Microscopy.* Phys. Rev. Lett. **88**, 097201 (2002).

[41] A.P. Ramirez, P. Schiffer, S.-W. Cheong, C.H. Chen, W. Bao, T.T.M. Palstra, P.L. Gammel, D.J. Bishop and B. Zegarski, *Thermodynamic and Electron Diffraction Signatures of Charge and Spin Ordering in $La_{1-x}Ca_xMnO_3$.* Phys. Rev. Lett. **76**, 3188-92 (1996).

[42] M.T. Fernández-Díaz, J.L. Martínez, J.M. Alonso and E. Herrero, *Structural, thermal, transport, and magnetic properties of the charge-ordered $La_{1/3}Ca_{2/3}MnO_3$ oxide.* Phys. Rev. B **59**, 1277-84 (1999).

[43] Ch. Renner, G. Aeppli, B.-G. Kim, Y.-A. Soh and S.-W. Cheong, *Atomic-scale images of charge ordering in a mixed-valence manganite.* Nature **416**, 518-21 (2002).

[44] M. Tokunaga, N. Miura, Y. Tomioka and Y. Tokura, *High-magnetic-field study of the phase transition of $R_{1-x}Ca_xMnO_3$ (R=Pr, Nd).* Phys. Rev. B **57**, 5259-64 (1998).

[45] A. Anane, J.-P. Renard, L. Reversat, C. Dupas, P. Veillet, M. Viret, L. Pinsard and A. Revcolevschi, *Colossal resistive relaxation effects in a $Pr_{0.67}Ca_{0.33}MnO_3$ single crystal.* Phys. Rev. B **59**, 77-80 (1999).

[46] W. Prellier, A. Biswas, M. Rajeswari, T. Venkatesan and R.L. Greene, *Effect of substrate-induced strain on the charge-ordering transition in $Nd_{0.5}Sr_{0.5}MnO_3$.* Appl. Phys. Lett. **75**, 397-9 (1999).

[47] S. Cox, E.J. Rosten, J.C. Loudon, J.C. Chapman, S. Kos, M.J. Calderón, D.J. Kang, P.B. Littlewood, P.A. Midgley and N.D. Mathur, *Control of $La_{0.5}Ca_{0.5}MnO_3$ superstructure through epitaxial strain release.* cond-mat/0504476 (submitted to Phys. Rev. Lett.) (2005).

[48] R. Shreekala, M. Rajeswari, R.C. Srivastava, K. Ghosh, A. Goyal, V.V. Srinivasu, S.E. Lofland, S.M. Bhagat, M. Downes, R.P. Sharma, S.B. Ogale, R.L. Greene, R. Ramesh, T. Venkatesan, R.A. Rao and C.B. Eom, *Ferromagnetism at room temperature in $La_{0.8}Ca_{0.2}MnO_3$ thin films.* Appl. Phys. Lett. **74**, 1886-8 (1999).

[49] R. Mahendiran, S.K. Tiwary, A.K. Raychaudhuri, T.V. Ramakrishnan, R. Mahesh, N. Rangavittal and C.N.R. Rao, *Structure, electron-transport properties, and giant magnetoresistance of hole-doped $LaMnO_3$ systems.* Phys. Rev. B **53**, 3348-58 (1996).

[50] R.M. Kusters, J. Singleton, D.A. Keen, R. McGreevy and W. Hayes, *Magnetoresistance measurements on the magnetic semiconductor $Nd_{0.5}Pb_{0.5}MnO_3$.* Physica B **155**, 362-5 (1989).

[51] G.J. Snyder, R. Hiskes, S. DiCarolis, M.R. Beasley and T.H. Geballe, *Intrinsic electrical transport and magnetic properties of $La_{0.67}Ca_{0.33}MnO_3$ and $La_{0.67}Sr_{0.33}MnO_3$ MOCVD thin films and bulk material.* Phys. Rev. B **53**, 14434-44 (1996).

[52] M. Viret, L. Ranno and J.M.D. Coey, *Magnetic localization in mixed-valence manganites.* Phys. Rev. B **55**, 8067-70 (1997).

[53] N.F. Mott, *Conduction in Non-Crystalline Materials*, Clarendon Press, Oxford (1993).

[54] N.F. Mott, *Conduction in glasses containing transition metal ions.* J. Non-Cryst. Solids **1**, 1-17 (1968).

[55] J.C. Loudon, *An investigation of the unconventional phases in the lanthanum calcium manganite system,* Ph.D. Thesis, University of Cambridge (2003).

[56] Y.H. Li, F. Damay, L.F. Cohen, K.A. Thomas, A.K.M. Hossain and J.L. MacManus-Driscoll, *Structure and Magnetic Properties of* $La_{0.7}Ca_{0.3}MnO_{3-\delta}$ *for* $(3-\delta) < 3.0$. J. Am. Ceram. Soc. **84**, 747-52 (2001).

[57] P. Murugavel, T.W. Noh and J.G. Yoon, *Thickness dependent and annealing effects of underdoped lanthanum manganite thin films grown on Si substrates.* J. Appl. Phys. **95**, 2536-9 (2004).

[58] W. Prellier, M. Rajeswari, T. Venkatesan and R.L. Greene, *Effects of annealing and strain on* $La_{1-x}Ca_xMnO_3$ *thin films: A phase diagram in the ferromagnetic region.* Appl. Phys. Lett. **75**, 1446-8 (1999).

[59] Y.G. Zhao, W. Cai, J. Zhao, X.P. Zhang, R. Fan, B.S. Cao, M.H. Zhu, T. Wu, S.B. Ogale, S.R. Shinde, T. Venkatesan, Q.Y. Tu, T.K. Mandal and J. Gopalakrishnan, *Insulator-metal transition and magnetoresistance of* $La_{0.5}Ca_{0.5}MnO_y$ *induced by tuning the oxygen content.* J. Appl. Phys. **92**, 5391-4 (2002).

[60] K. Dörr, J.M. De Teresa, K.H. Müller, D. Eckert, T. Walter, E. Vlakhov, K. Nenkov and L. Schultz, *Preparation and properties of epitaxial* $La_{0.7}Ca_{0.3}MnO_{3-\delta}$ *films with reduced carrier density.* J. Phys.: Condens. Mat. **12**, 7099-109 (2000).

[61] N. Malde, P.S.I.P.N. de Silva, A.K.M. Akther Hossain, L.F. Cohen, K.A. Thomas, J.L. MacManus-Driscoll, N.D. Mathur and M.G. Blamire, *Influence of oxygen stoichiometry on Raman phonon spectroscopy, lattice parameters and physical properties of* $La_{0.7}Ca_{0.3}MnO_3$ *thin films.* Solid State Commun. **105**, 643-8 (1998).

[62] M. Roy, J.F. Mitchell, A.P. Ramirez and P. Schiffer, *A study of the magnetic and electrical crossover region of* $La_{0.5+/-\delta}Ca_{0.5-/+\delta}MnO_3$. J. Phys.: Condens. Mat. **11**, 4843-59 (1999).

[63] G.-M. Zhao, K. Conder, H. Keller and K.A Müller, *Giant oxygen isotope shift in the magnetoresistive perovskite* $La_{1-x}Ca_xMnO_{3+y}$. Nature **381**, 676-8 (1996).

[64] N.A. Babushkina, A.N. Taldenkov, L.M. Belova, E.A. Chistotina, O.Yu. Gorbenko, A.R. Kaul, K.I. Kugel and D.I. Khomskii, *Partial $^{16}O \rightarrow ^{18}O$ isotope substitution and phase separation in $(La_{0.25}Pr_{0.75})_{0.7}Ca_{0.3}MnO_3$ manganite.* Phys. Rev. B **62**, R6081-4 (2000).

[65] A.J. Millis, T. Darling and A. Migliori, *Quantifying strain dependence in "colossal" magnetoresistance manganites.* J. Appl. Phys. **83**, 1588-91 (1998).

[66] J.Z. Sun, D.W. Abraham, R.A. Rao and C.B. Eom, *Thickness-dependent magnetotransport in ultrathin manganite films.* Appl. Phys. Lett. **74**, 3017-9 (1999).

[67] N.K. Todd, N.D. Mathur and M.G. Blamire, *Dependence on film thickness of grain boundary low-field magnetoresistance in thin films of $La_{0.7}Ca_{0.3}MnO_3$.* J. Appl. Phys. **89**, 6970-2 (2001).

[68] B. Wiedenhorst, C. Höfener, Y. Lu, J. Klein, M.S.R. Rao, B.H. Freitag, W. Mader, L. Alff and R. Gross, *High-resolution transmission electron microscopy study on strained epitaxial manganite thin films and heterostructures.* J. Magn. Magn. Mater. **211**, 16-21 (2000).

[69] E.B. Nyeanchi, I.P. Krylov, X.-M. Zhu and N. Jacobs, *Ferromagnetic ground state in $La_{0.5}Ca_{0.5}MnO_3$ thin films.* Europhys. Lett. **48**, 228-32 (1999).

[70] J. Klein, J.B. Philipp, D. Reisinger, M. Opel, A. Marx, A. Erb, L. Alff and R. Gross, *Orbital order and anisotropic transport properties in doped manganites induced by epitaxial coherency strain.* J. Appl. Phys. **93**, 7373-5 (2003).

[71] *Powder Diffraction FIle*, International Centre for Diffraction Data, Pennsylvania, USA

[72] R.A. Rao, D. Lavric, T.K. Nath, C.B. Eom, L. Wu and F. Tsui, *Effects of film thickness and lattice mismatch on strain states and magnetic properties of $La_{0.8}Ca_{0.2}MnO_3$.* J. Appl. Phys. **85**, 4794-6 (1999).

[73] J. O'Donnell, M.S. Rzchowski, J.N. Eckstein and I. Bozovic, *Magnetoelastic coupling and magnetic anisotropy in $La_{0.67}Ca_{0.33}MnO_3$ films.* Appl. Phys. Lett. **72**, 1775-7 (1998).

[74] Y.-A. Soh, P.G. Evans, Z. Cai, B. Lai, C.-Y. Kim, G. Aeppli, N.D. Mathur, M.G. Blamire and E.D. Isaacs, *Local Mapping of strain at grain boundaries in colossal magnetoresistive films using x-ray microdiffraction.* J. Appl. Phys. **91**, 7742-4 (2002).

[75] Y.-A. Soh, G. Aeppli, N.D. Mathur and M.G. Blamire, *Mesoscale magnetism at the grain boundaries in colossal magnetoresistive films.* Phys. Rev. B **63**, 020402(R) (2000).

Chapter 3 Phase coexistence in manganites

Although the three basic phases (paramagnetic insulator, ferromagnetic metal and charge-ordered antiferromagnetic insulator) seen in the $La_{1-x}Ca_xMnO_3$ system initially appear to be quite distinct, it is nevertheless possible to have multiple phases coexisting over surprisingly small lengthscales. The free energies of the phases involved are remarkably similar and the system may be intrinsically inhomogeneous with competition between the various phases. There has been extensive work, both theoretical and experimental, over the past few years that has probed this delicate balance and found that phase coexistence occurs in a remarkably wide region of the phase diagram and not just close to the phase boundaries as might be first thought.

3.1 Multi-phase coexistence

Multi-phase coexistence in the manganites has been investigated using theoretical models that use many different Hamiltonians and computational techniques. Early attempts [1,2] relied on different mechanisms to explain phase separation, namely electronic phase separation on a nanometre lengthscale and disorder-induced inhomogeneity (usually due to the random distribution of the A-site cations) on a micrometre scale. However, the presence of two distinct lengthscales for phase separation was in disagreement with the majority of the rapidly accumulating experimental evidence. Additionally, charge segregation on a nanometre scale has a prohibitively high Coulomb energy. More recently, Mathur and Littlewood [3] used a Landau theory to explain the coexistence using three coupled parameters: the strain state, the charge-modulation vector and the magnetic field, although they assumed that the magnetic contribution to the overall free energy would be negligible. Their emphasis was on strain as the underlying parameter and they were able to predict phase separation on a mesoscopic lengthscale. Then in 2004 Ahn *et al.* presented a model in which everything was parameterised in terms of the strain in the sample [4]. Their model also predicted micron-scale coexistence, which suggests that strain is indeed the most important factor in determining whether phase separation will occur. However, by completely neglecting the magnetic and electronic interactions, this last model is incomplete. More recently, Milward *et al.*

have used coupled parameters in a Landau theory to understand the richness of the phase diagram [5].

There has been a vast amount of experimental work concerned with the phenomenon of phase coexistence in the manganites. This body of evidence increasingly points towards a scenario where manganite physics is governed by multi-phase coexistence. However, experimental evidence will always be slightly unsatisfactory as the effect of any defects, e.g. grain boundaries or dislocations, within the sample introduced during the preparation or measurement processes will be unclear. Such defects can alter the delicate balance between the competing phases, e.g. by acting as nucleation sites, and cause *extrinsic* phase separation, as opposed to *intrinsic* phase separation. There are also considerations as to the limit of the spatial extent of a phase. For example, a single stripe within a charge ordered region is too small to be a separate thermodynamic entity and cannot be considered as a separate phase. Most of the interest has been centred on the first-order phase transition that occurs at low temperature between the ferromagnetic (FM) and charge-ordered (CO) states (e.g. near x=0.5 for the bulk $La_{1-x}Ca_xMnO_3$ system) and some of the more significant experimental results are discussed in the remainder of this chapter.

Levy *et al*. studied polycrystalline samples of $La_{0.5}Ca_{0.5}MnO_3$ with varying grain sizes [6]. In zero field, the electrical transport properties depended on the average grain size as shown in Figure 3.1. For grain sizes above 450 nm, there was a sharp increase in resistivity at about 140 K as the material entered a CO insulating state. For the samples with a smaller grain size, no sharp increase was observed. All the samples showed metallic behaviour (defined as $d\rho/dT > 0$) at low temperatures, which suggests that there was still some metallic material present for all the grain sizes studied. The metal-insulator transition temperature T_{MI} also showed a dependence on the grain size and decreased as the grain size increased.

Magnetisation data on the same series of samples (shown in Figure 3.2) also gave evidence for phase coexistence. The magnetic moment fell sharply below 140 K, which is consistent with a CO transition, for the samples with an average grain size of 450 nm or greater, but continued to increase with decreasing temperature for the smaller grain sizes.

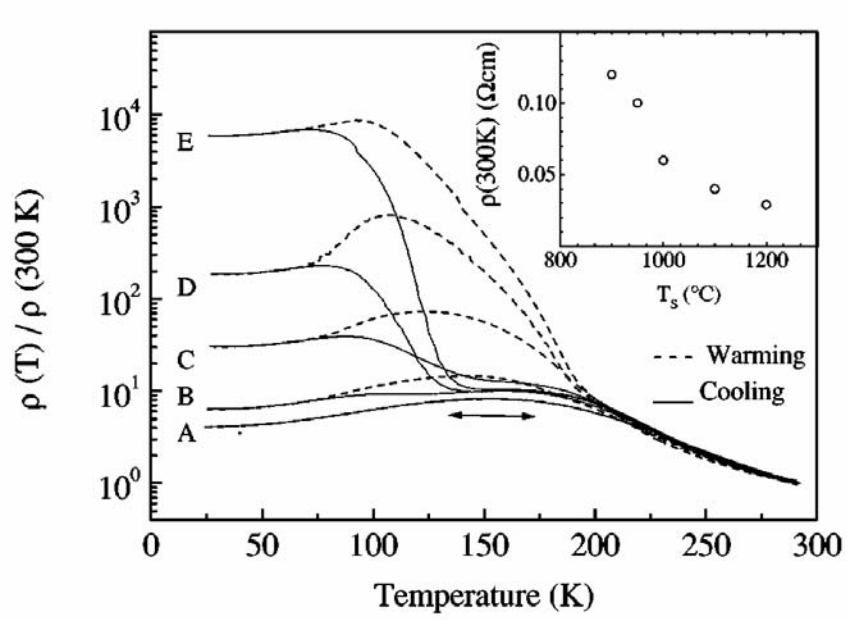

Figure 3.1. Resistivity vs. temperature traces for polycrystalline $La_{0.5}Ca_{0.5}MnO_3$. The average grain sizes were (A) 180 nm, (B) 250 nm, (C) 450 nm, (D) 950 nm and (E) 1300 nm respectively. Inset: room temperature resistivity as a function of final sintering temperature. (Taken from [6].)

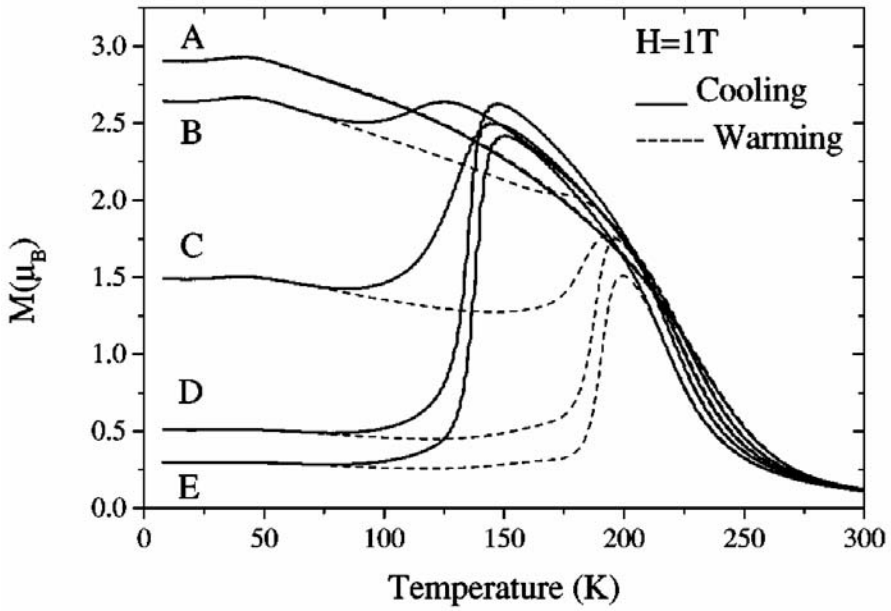

Figure 3.2. Magnetisation curves for polycrystalline samples of $La_{0.5}Ca_{0.5}MnO_3$. The average grain sizes were (A) 180 nm, (B) 250 nm, (C) 450 nm, (D) 950 nm and (E) 1300 nm respectively. (Taken from [6].)[1]

[1] It should be noted throughout this section that the magnetic fields described in the figures are strictly either *B* fields measured in T, or *H* fields measured in A/m.

The transport and magnetisation data from Figures 3.1 and 3.2 are consistent with some fraction of the samples undergoing a transition from a FM state to a CO state on cooling. The residual moment at 20 K was below the theoretical spin-aligned value of 3.5 μ_B/Mn ion for each sample and gave an indication of the fraction of the sample that was in the ferromagnetic state. The residual moment increased as the grain size decreased, which suggests that the structural defects and variation in the strain state introduced by the grain boundaries prevent the charge ordered state from forming. X-ray studies on $La_{0.7}Sr_{0.3}MnO_3$ films grown on bicrystal substrates have shown that the lattice parameter, and hence the strain state, vary close to a grain boundary [7]. There is significant hysteresis in both the magnetisation and transport data, which is indicative, but not conclusive, evidence of phase coexistence.

Visual evidence of phase coexistence is often the most convincing. The TEM work done by Uehara *et al*. on the $La_{1-x-y}Pr_yCa_xMnO_3$ system demonstrates phase coexistence via a dark field image of $La_{1/4}Pr_{3/8}Ca_{3/8}MnO_3$ [8]. Figure 3.3 shows coexistence between charge ordered and charge disordered domains at 20 K. The

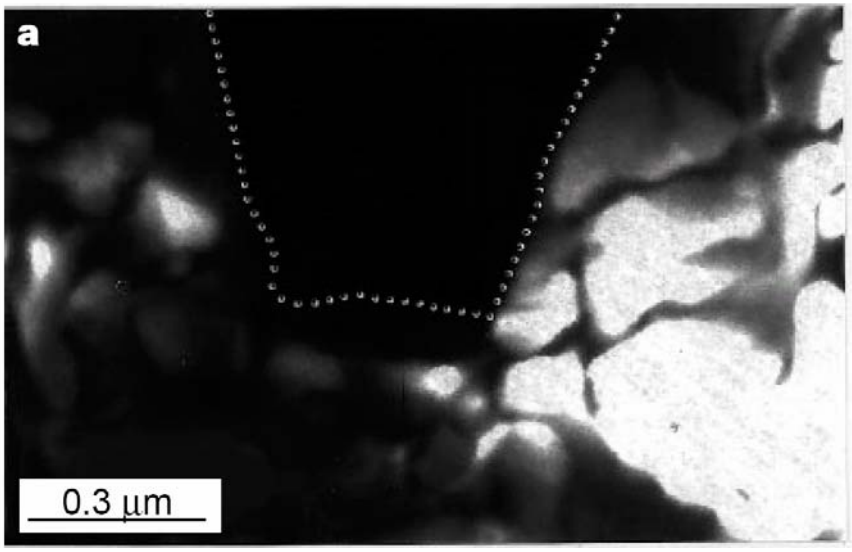

Figure 3.3. A dark field electron microscopy image taken at 20 K of a bulk $La_{1/4}Pr_{3/8}Ca_{3/8}MnO_3$ sample. The image is taken from a superlattice peak arising from additional periodicity due to charge ordering. This shows the coexistence of charge ordered (light) regions and charge disordered (dark) regions. The dotted line indicates the extent of the charge-disordered region. (Taken from [8].)

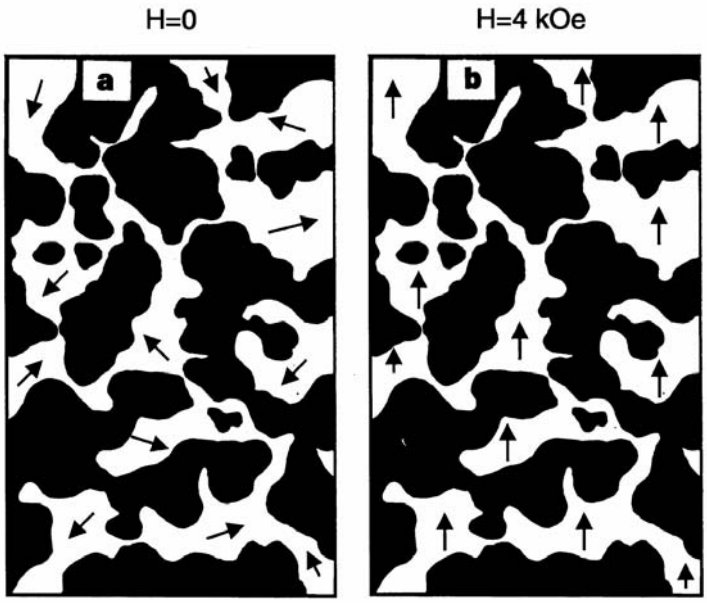

Figure 3.4. A schematic diagram representing the phase coexistence observed at low temperature. The white regions represent the ferromagnetic metallic phase and the dark regions the charge ordered insulator. The magnetic moments (represented by the arrows) align when a field H=4 kOe is applied. The domains are typically 500-1000 nm across. (Taken from [8].)

charge-disordered regions were inferred to be ferromagnetic from resistivity and magnetisation data. They proposed a mechanism, as depicted in Figure 3.4, in which the transition between the two phases when a magnetic field is applied proceeds via a percolative mechanism.

Further visual evidence was provided by scanning tunnelling spectroscopy (STS) measurements on the surface of $La_{0.7}Ca_{0.3}MnO_3$ thin films by Fäth *et al.* [9]. This revealed sub-micrometre coexistence just below T_C between insulating and metallic clusters. The fraction of ferromagnetic material increased with increasing magnetic field, but there were still significant insulating regions in a 9 T field. However, these films were grown on a $YBa_2Ca_3O_{7-\delta}$ buffer layer to provide a conducting layer for the STS measurements. The metal-insulator transition was suppressed to 230 K in zero field, which suggests a low-quality film. The poor quality film is one possible reason for the observed phase separation. In addition, neutron diffraction studies on $(La_{0.25}Pr_{0.75})_{0.7}Ca_{0.3}MnO_3$ showed peaks corresponding to both FM and antiferromagnetic (AF) phases at low temperatures [10]. This gives a useful insight into the spatial extent of these phases, as an area of a few hundred

Ångstroms is required to produce neutron diffraction peaks. Further work by Balagurov *et al.* indicated that the FM and AF regions in this compound were roughly 100 nm in size [11]. These last three techniques (TEM, STS and neutron diffraction) have all suggested that phase coexistence occurs over hundreds of nanometres.

Other techniques have been used to probe phase coexistence. Roy *et al.* studied the specific heat C of various manganite samples at 5.5 K including polycrystalline samples of $La_{1-x}Ca_xMnO_3$ with x=0.33 and x=0.50 [12]. $La_{0.67}Ca_{0.33}MnO_3$ showed behaviour typical of a ferromagnet in which there was a maximum in $C(B)$ at zero field, and the heat capacity decreased monotonically by approximately 10% as the field was increased to 9 T. The sample with x=0.50 showed strong evidence of phase coexistence via magnetic hysteresis and non-equilibrium effects, as shown in Figure 3.5. The heat capacity increased by 19% while the sample was exposed to a 9 T field for 10 minutes, suggesting that the relative fractions of the FM and AF

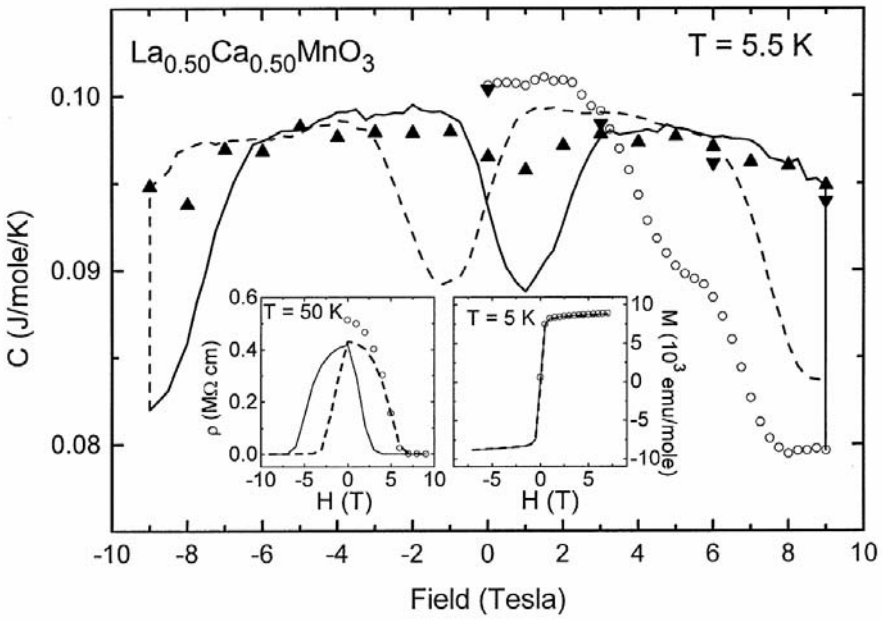

Figure 3.5. The specific heat of $La_{0.50}Ca_{0.50}MnO_3$ as a function of field at T=5.5 K. The sample was measured in continuous mode when the field was swept from 0→9 T (open circles), 9 T→−9 T (solid lines) and −9 T→9 T (dashed lines) and at equilibrium with the field increasing (solid downwards triangles) and decreasing (solid upright triangles). The insets show the resistivity (50 K, left panel) and magnetisation (5 K, right panel) respectively as a function of applied field. (Taken from [12].)

phases were still altering and that the magnetic heat capacity of the FM phase is higher than that of the AF phase. The increase at 9 T was much less pronounced (~2%) when the system was allowed to stabilise for 1 hour at each field before each measurement.

Nuclear magnetic resonance (NMR) studies have also been used to indicate the presence of metallic regions via the narrowing of the ^{55}Mn resonances. Figure 3.6 shows the results of a systematic study of the ^{55}Mn spin spectra for the $La_{1-x}Ca_xMnO_3$ system performed by Kapusta *et al.* [13]. The peak at 380 MHz, which is present for all compositions studied, was attributed to the fast hopping between Mn^{3+} and Mn^{4+} ions mediated by double exchange. The peak was most significant for the metallic compositions $La_{0.67}Ca_{0.33}MnO_3$ and $La_{0.55}Ca_{0.45}MnO_3$. However, NMR is only sensitive to the immediate environment of the nuclei and consequently probes a much

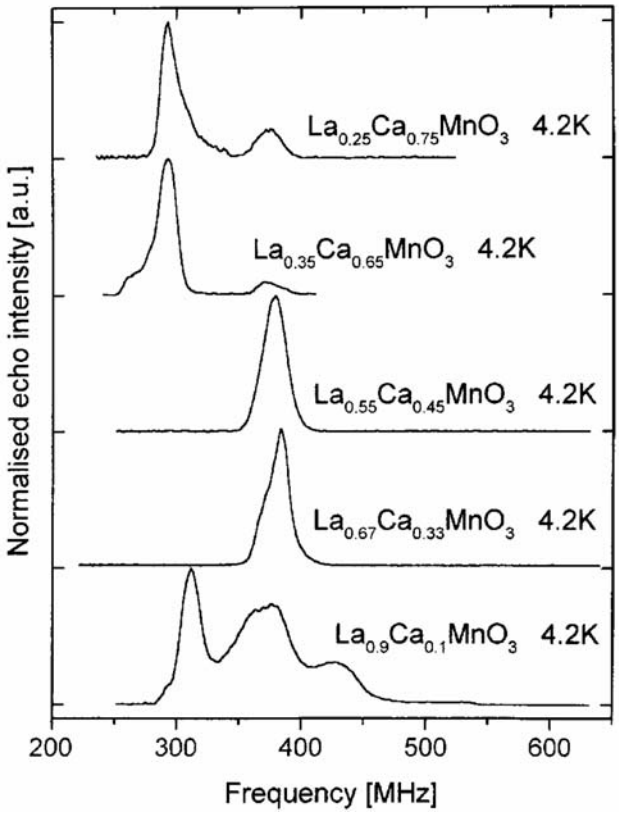

Figure 3.6. The ^{55}Mn spin echo spectra for various $La_{1-x}Ca_xMnO_3$ compositions at 4.2 K and zero external field. The peak at 380 MHz is attributed to the fast hopping between Mn^{3+} and Mn^{4+} ions mediated by double exchange. (Taken from [13].)

shorter lengthscale than most other techniques, e.g. neutron diffraction. Thus, this result does not imply the presence of a thermodynamic metallic phase for all members of the $La_{1-x}Ca_xMnO_3$ family

Until 2002, it was thought that while charge order and ferromagnetism could exist within the same sample, there would be separate CO and FM clusters. Then a surprising discovery was made when TEM and holography studies on polycrystalline $La_{0.50}Ca_{0.50}MnO_3$ revealed a micron-sized region that was both ferromagnetic and charge ordered [14]. The magnetic moment in this region was 3.5±0.2 μ_B per manganese ion, which was in excellent agreement with the fully spin-aligned value of 3.5 μ_B/Mn ion.

From all of the gathered evidence, it now seems clear that for compositions near the low-temperature FM-CO phase boundary there is a local equilibrium with FM regions in an insulating CO matrix. Moreover, there is a remarkably wide range of parameters that can affect the relative proportions of the competing phases, including pressure [15], magnetic field [9,16,17], temperature [17], electric field [18], film thickness [19,20], oxygen isotope [21] and illumination with X-rays [22] or visible light [23]. If the ferromagnetic regions in the sample are sufficiently large and well connected, then it should possible for the itinerant electrons to percolate from one ferromagnetic region to the next. This should reduce the resistivity and lead to metallic behaviour in the sample.

Numerical simulations have predicted percolation in 3-D if the FM fraction is greater than 14% [24]. This is in good agreement with measurements by Kim *et al.* on the $La_{5/8-x}Pr_xCa_{3/8}MnO_3$ system where metallic behaviour was seen when the FM fraction was greater than 17% [25]. While these experimental values have been obtained for a subtly different compound, and recall that minor differences in the manganites can lead to vastly differing properties, the percolation threshold for the $La_{1-x}Ca_xMnO_3$ system should not be too different from the above values.

3.2 Time-dependent behaviour

Section 3.1 above has considered the phenomenon of phase separation in the manganites from the point of view of a static distribution of the competing phases. However, the distribution can also vary with time, particularly immediately after an external parameter is altered, and this can provide further insight into the nature of the phase separation and in particular whether the system was initially in a metastable state. Levy *et al.* studied polycrystalline samples of the B-site doped manganite $La_{0.5}Ca_{0.5}Mn_{0.95}Fe_{0.05}O_3$ [26]. Figure 3.7 shows the variation of resistivity with time and the magnetic history of the sample.

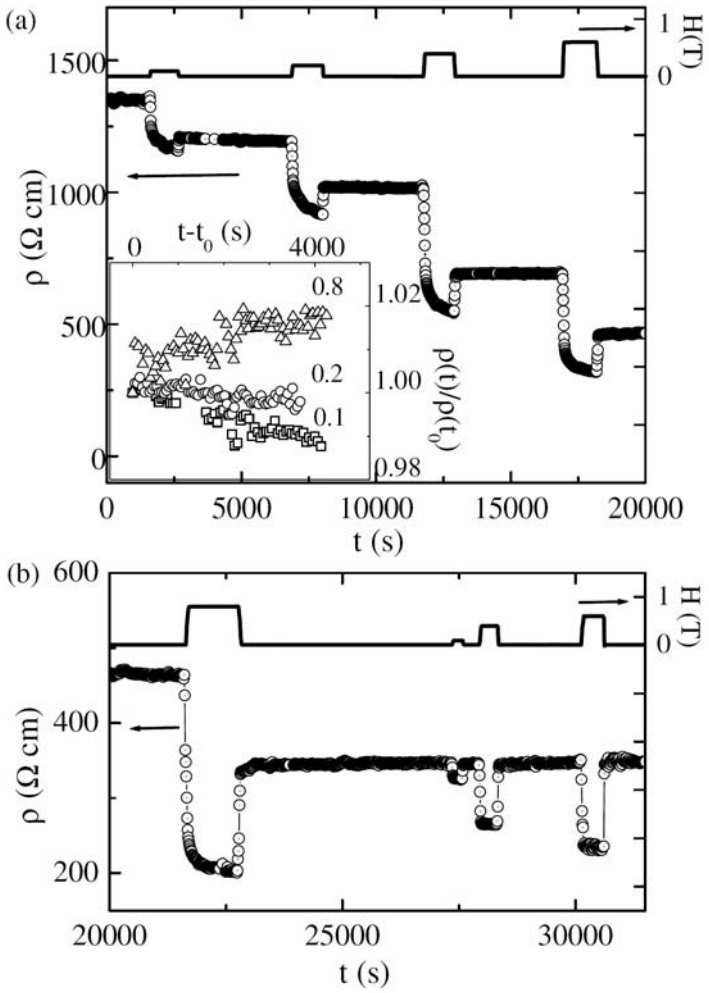

Figure 3.7. Resistivity as a function of time and magnetic history for polycrystalline $La_{0.5}Ca_{0.5}Mn_{0.95}Fe_{0.05}O_3$ at 72 K (a) upon application and removal of B=0.1 T, 0.2 T, 0.4 T and 0.6 T. (Inset: time dependence of ρ(72 K) in zero field normalised to the value after the field was removed; the labels are the B fields. (b) upon application of B=0.1 T, 0.4 T and 0.6 T after B=0.8 T was applied and removed. (Taken from [26].)

Upon application of a magnetic field the resistivity ρ initially dropped sharply due to sudden spin- and domain-alignment. There was a further slow exponential change in ρ while the field was still applied, suggesting that this is a non-equilibrium process and the system is relaxing into its equilibrium state. On removal of the field, ρ did not return to its initial value but rather to a lower value that corresponded to a larger ferromagnetic fraction. The system appeared to 'remember' the highest field that it had experienced, e.g. in the cycle B=0→0.8 T→0→0.1 T→0 the final state depended only on the 0.8 T field.

After the magnetic field had been removed, the resistivity continued to alter (Figure 3.7(a), inset), indicating that the ratio of the two phases was still changing. The sign of the relaxation appeared to depend on the maximum applied field i.e. for preceding fields of 0.1 T and 0.2 T the resistivity continued to fall with time, whereas for B=0.8 T the resistivity increased after removal of the field. This suggests that the 0.8 T field had pushed the sample past its equilibrium point and the system was evolving by reducing the fraction of FM material as opposed to increasing the FM fraction after applying fields of 0.1 T and 0.2 T.

By applying a sequence of magnetic fields, phase-separated materials could possibly be used as memory devices. An external magnetic field would write to the device, with the reading process being via $\rho(T,H)$ measurements. Subsequent attempts to write to the device would either need to use a field that was greater than any previously applied field, or the material would need to be 'reset' by warming it up into the paramagnetic phase and randomising the Mn spins before cooling again. Clearly, this limits the practicality of such a device.

A further study of polycrystalline $La_{0.5}Ca_{0.5}Mn_{0.95}Fe_{0.05}O_3$ showed a standard metal-insulator transition at 80 K on cooling [27]. The resistivity below the transition temperature depended on the cooling rate, but the actual transition temperature (as defined by the peak in the resistivity curve) was unaffected. Furthermore if the temperature was held constant with $T<T_C$ for 1 hour during cooling, then the resistance continued to decrease with a logarithmic time dependence. The authors attributed this relaxation to the continued expansion of FM clusters within a non-FM matrix. On resumption of cooling, the resistance was 'rejuvenated' and merged

smoothly with the curve obtained with cooling at a constant rate. A phenomenological model was proposed in which the expansion of the FM regions against the host material proceeded via a step-wise movement of phase boundaries through energy barriers. In this model, the slope of the resistivity curve had a static contribution from $d\rho/dT$ for fixed fractions of each type of phase, and a dynamical term related to the change in size of the FM clusters.

Fluctuations with time in the ratio of the two phases have also been reported. Raquet *et al.* reported two-level fluctuations in resistance below T_C in a thin film of $La_{2/3}Ca_{1/3}MnO_3$ grown on $LaAlO_3$ [28]. Figure 3.8 depicts the fluctuations observed at different temperatures. The presence of the fluctuations was attributed to a dynamic mixed-phase percolative conduction process in which clusters within the sample swap between two phases with differing conductivities on a timescale of a few hundreds of milliseconds. Further work by Merithew *et al.* also found resistance

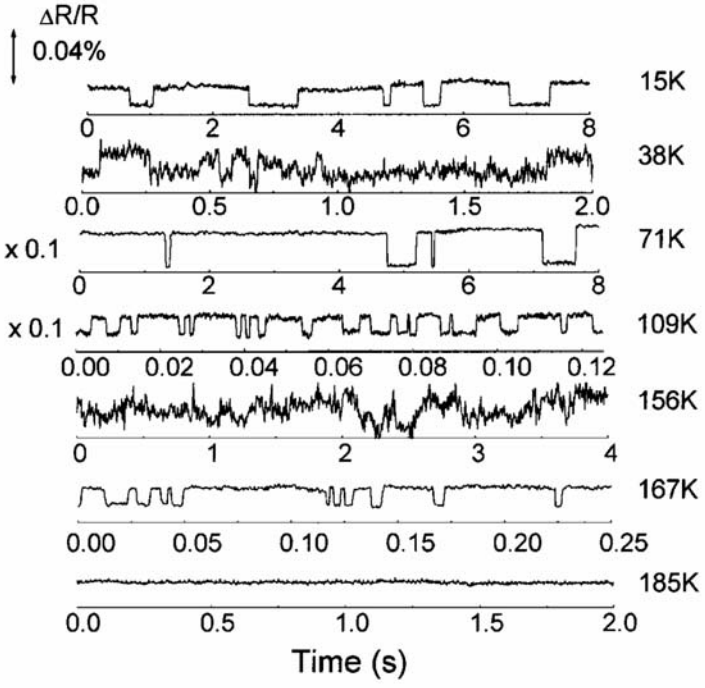

Figure 3.8. Fluctuations in resistance at different temperatures for a $La_{2/3}Ca_{1/3}MnO_3$ film grown on $LaAlO_3$. The noise fluctuated from a strongly non-Gaussian type to random telegraph noise (RTN). The value of $\Delta R/R$ varied from 0.01% to 0.2%. There was no evidence for RTN above 185 K. The Curie temperature was roughly 210 K. (Taken from [28].)

fluctuations in both bulk samples of $La_{0.67}Ca_{0.33}MnO_3$ and films grown on $SrTiO_3$ [29]. The regions that experienced fluctuations were micron sized, and were larger in the bulk sample. This result agrees well with the typical sizes of the phases found by other methods as mentioned in Section 3.1. The effect of strain was investigated further by Reutler *et al.* [30], who found that $La_{0.7}Ca_{0.3}MnO_3$ films on $NdGaO_3$ (001) (lattice mismatch ~0.1%) had a smaller contribution from low frequency $1/f$ noise than similar films on $SrTiO_3$ (001) (lattice mismatch ~1.5%). The noise level was several orders of magnitude higher in the more highly strained film.

References for Chapter 3

[1] J. Burgy, A. Moreo and E. Dagotto, *Relevance of Cooperative Lattice Effects and Stress Fields in Phase-Separation Theories for CMR Manganites.* Phys. Rev. Lett. **92**, 097272 (2004).

[2] A. Moreo, S. Yunoki and E. Dagotto, *Phase Separation Scenario for Manganese Oxides and Related Materials.* Science **283**, 2034-40 (1999).

[3] N.D. Mathur and P.B. Littlewood, *The self-organised phases of manganites.* Solid State Commun. **119**, 271-80 (2001).

[4] K.H. Ahn, T. Lookman and A.R. Bishop, *Strain-induced metal-insulator phase coexistence in perovskite manganites.* Nature **428**, 401-4 (2004).

[5] G.C. Milward, M.J. Calderon and P.B. Littlewood, *Electronically soft phases in manganites.* Nature **433**, 607-10 (2005).

[6] P. Levy, F. Parisi, G. Polla, D. Vega, G. Leyva, H. Lanza, R.S. Freitas and L. Ghivelder, *Controlled phase separation in $La_{0.5}Ca_{0.5}MnO_3$.* Phys. Rev. B **62**, 6437-41 (2000).

[7] Y.-A. Soh, P.G. Evans, Z. Cai, B. Lai, C.-Y. Kim, G. Aeppli, N.D. Mathur, M.G. Blamire and E.D. Isaacs, *Local Mapping of strain at grain boundaries in colossal magnetoresistive films using x-ray microdiffraction.* J. Appl. Phys. **91**, 7742-4 (2002).

[8] M. Uehara, S. Mori, C.H. Chen and S.-W. Cheong, *Percolative phase separation underlies colossal magnetoresistance in mixed-valent manganites.* Nature **399**, 560-3 (1999).

[9] M. Fäth, S. Freisem, A.A. Menovsky, Y. Tomioka, J. Aarts and J.A. Mydosh, *Spatially Inhomogeneous Metal-Insulator Transition in Doped Manganites.* Science **285**, 1540-2 (1999).

[10] A.M. Balagurov, V.Yu. Pomjakushin, D.V. Sheptyakov, V.I. Aksenov, N.A. Babushkina, L.M. Belova, A.N. Taldenkov, A.V. Inyushkin, P. Fischer, M. Gutmann, I. Keller, O.Yu. Gorbenko and A.R. Kaul, *Effect of oxygen isotope substitution on the magnetic structure of $(La_{0.25}Pr_{0.75})_{0.7}Ca_{0.3}MnO_3$.* Phys. Rev. B **60**, 383-7 (1999).

[11] A.M. Balagurov, V.Yu. Pomjakushin, D.V. Sheptyakov, V.L. Aksenov, P. Fischer, L. Keller, O.Yu. Gorbenko, A.R. Kaul and N.A. Babushkina, *Long-scale phase separation versus homogeneous magnetic state in $(La_{1-y}Pr_y)_{0.7}Ca_{0.3}MnO_3$: A neutron diffraction study.* Phys. Rev. B **64**, 024420 (2001).

[12] M. Roy, J.F. Mitchell, S.J. Potashnik and P. Schiffer, *Field dependent specific heat of rare-earth manganites.* J. Magn. Magn. Mater. **218**, 191-7 (2000).

[13] Cz. Kapusta, P.C. Riedi, W. Kocemba, M.R. Ibarra and J.M.D. Coey, *Nuclear magnetic resosance study of magnetic phase separation in $La_{1-x}Ca_xMnO_3$.* J. Appl. Phys. **87**, 7121-3 (2000).

[14] J.C. Loudon, N.D. Mathur and P.A. Midgley, *Charge-ordered ferromagnetic phase in $La_{0.5}Ca_{0.5}MnO_3$.* Nature **420**, 797-800 (2002).

[15] H.Y. Hwang, T.T.M. Palstra, S.-W. Cheong and B. Batlogg, *Pressure effects on the magnetoresistance in doped manganese perovskites.* Phys. Rev. B **52**, 15046-9 (1995).

[16] A. Asamitsu, Y. Moritomo, Y. Tomioka, T. Arima and Y. Tokura, *A structural phase transition induced by an external magnetic field.* Nature **373**, 407-9 (1995).

[17] N.A. Babushkina, L.M. Belova, D.I. Khomskii, K.I. Kugel, O.Yu. Gorbenko and A.R. Kaul, *Low-temperature transition to a metallic state in $(La_{0.5}Pr_{0.5})_{0.7}Ca_{0.3}MnO_3$ films.* Phys. Rev. B **59**, 6994-7000 (1999).

[18] A. Asamitsu, Y. Tomioka, H. Kuwahara and Y. Tokura, *Current switching of resistive states in magnetoresistive manganites.* Nature **388**, 50-2 (1997).

[19] R. Rauer, J. Bäckström, D. Budelmann, M. Kurfiß, M. Schilling, M. Rübhausen, T. Walter, K. Dörr and S.L. Cooper, *Thickness dependent phase separation in $La_{0.7}Ca_{0.3}MnO_3$ films.* Appl. Phys. Lett. **81**, 3777-9 (2002).

[20] M. Bibes, Ll. Balcells, S. Valencia, J. Fontcuberta, M. Wojcik, E. Jedryka and S. Nadolski, *Nanoscale Multiphase Separation at $La_{2/3}Ca_{1/3}MnO_3/SrTiO_3$ Interfaces.* Phys. Rev. Lett. **87**, 067210 (2001).

[21] N.A. Babushkina, A.N. Taldenkov, L.M. Belova, E.A. Chistotina, O.Yu. Gorbenko, A.R. Kaul, K.I. Kugel and D.I. Khomskii, *Partial $^{16}O \rightarrow ^{18}O$ isotope substitution and phase separation in $(La_{0.25}Pr_{0.75})_{0.7}Ca_{0.3}MnO_3$ manganite.* Phys. Rev. B **62**, R6081-4 (2000).

[22] V. Kiryukhin, D. Casa, J.P. Hill, B. Keimer, A. Vigilante, Y. Tomioka and Y. Tokura, *An X-ray-induced insulator-metal transition in a magnetoresistive manganite.* Nature **386**, 813-5 (1997).

[23] V. Moshnyaga, A. Giske, K. Samwer, E. Mishina, T. Tamura, S. Nakabayashi, A. Belenchuk, O. Shapoval and L. Kulyuk, *Giant negative photoconductivity in $La_{0.7}Ca_{0.3}MnO_3$ thin films.* J. Appl. Phys. **95**, 7360-62 (2004).

[24] I. Webman, J. Jortner and M.H. Cohen, *Numerical simulation of continuous percolation conductivity.* Phys. Rev. B **14**, 4737-40 (1976).

[25] K.H. Kim, M. Uehara, C. Hess, P.A. Sharma and S.-W. Cheong, *Thermal and Electronic Transport Properties and Two-Phase Mixtures in $La_{5/8-x}Pr_xCa_{3/8}MnO_3$.* Phys. Rev. Lett. **84**, 2961-4 (2000).

[26] P. Levy, F. Parisi, L. Granja, E. Indelicato and G. Polla, *Novel Dynamical Effects and Persistent Memory in Phase Separated Manganites.* Phys. Rev. Lett. **89**, 137001 (2002).

[27] L. Granja, E. Indelicato, P. Levy, G. Polla, D. Vega and F. Parisi, *Dynamical effects in magnetic and transport properties of phase separated* $La_{0.5}Ca_{0.5}Mn_{0.95}Fe_{0.05}O_3$. Physica B **320**, 94-6 (2002).

[28] B. Raquet, A. Anane, S. Wirth, P. Xiong and S. von Molnár, *Noise Probe of the Dynamic Phase Separation in* $La_{2/3}Ca_{1/3}MnO_3$. Phys. Rev. Lett. **84**, 4485-8 (2000).

[29] R.D. Merithew, M.B. Weissman, F.M. Hess, P. Spradling, E.R. Nowak, J. O'Donnell, J.N. Eckstein, Y. Tokura and Y. Tomioka, *Mesoscopic Thermodynamics of an Inhomogeneous Colossal-Magnetoresistive Phase.* Phys. Rev. Lett. **84**, 3442-5 (2000).

[30] P. Reutler, A. Bensaid, F. Herbstritt, C. Höfener, A. Marx and R. Gross, *Local magnetic order in magnanite thin films studied by 1/f noise measurements.* Phys. Rev. B **62**, 11619-25 (2000).

Chapter 4 Experimental methods

The doped perovskite manganite films studied in this dissertation were all grown by pulsed laser deposition (PLD). PLD is a complex non-equilibrium process and to understand it fully would require a deep understanding of plasma physics, thermodynamics, and the nucleation of the particles on the substrate amongst other factors. In a typical deposition, the laser beam is focused onto the surface of the target. The surface is then heated rapidly to a temperature much higher than the evaporation point of all the constituent elements, thereby giving a plume of ablated particles. One of the many advantages of PLD over sputtering techniques is that is it possible to have stoichiometric transfer from the target to the film, and PLD has been widely used in the development of complex materials such as high-temperature superconductors and the mixed valence manganites where small differences in composition can lead to significant differences in the resultant physical properties. A further advantage is that it only requires a moderate vacuum (10^{-6} mbar) unlike a typical sputtering process where a base pressure of 10^{-8} mbar or better is needed to reduce the level of impurities. Hence, PLD is a relatively quick and easy deposition technique. Nevertheless, PLD does have some negative features. Due to the narrow angular size of the plume, PLD does not scale up so well and consequently it is used mainly as a research tool rather than an industrial production method. There is also the risk of micron-sized particulates from the target hitting the film and impairing the quality of the sample. This can be overcome by using an off-axis geometry, but the deposition rate is then much reduced.

4.1 Substrate and target preparation

Commercially available $NdGaO_3$ (001) and $SrTiO_3$ (001) (Crystal GmbH, Berlin) substrates were used in this study. One side of the substrate was epi-polished by the manufacturers. This side was cleaned with acetone and iso-propanol and then sprayed with iso-propanol and compressed air. This treatment was found to be sufficient for $NdGaO_3$. However, for $SrTiO_3$ this level of surface preparation did not lead to consistently smooth films and a further level of substrate preparation was required. Following the procedure of Kawasaki *et al*. [1], the $SrTiO_3$ substrates were immersed in a NH_4F-HF buffer solution for 30 seconds, rinsed in deionised water and

subsequently annealed in flowing oxygen at 950ºC for one hour. The authors found that this process lead to the surface terminations being predominately TiO_2 (as opposed to SrO) and made it easier to obtain high quality films with integer unit cell terrace step heights. Figure 4.1 shows atomic force microscopy (AFM) scans for a $SrTiO_3$ (001) substrate before and after etching in the NH_4F-HF buffer solution and annealing. The first scan shows a 5×5 μm^2 scan of a substrate after cleaning with acetone and iso-propanol. Although the surface is smooth, no atomic terraces are visible. The second image was taken on the same substrate after etching and annealing. This image clearly shows atomic-scale terraces. Atomic force microscopy is discussed in more detail in Section 4.3.1. Whilst the growth mode is not necessarily vital for measuring the properties of plain films (unlike for multilayers in which a smooth interface between adjacent layers is critical), a high quality surface is still required since it indicates a high quality sample and high quality samples should lead to a better understanding of the intrinsic physics.

There have been many instances of manganite films being grown using $LaAlO_3$ as a substrate [2-5]. However, $LaAlO_3$ readily forms twins [6] and consequently films deposited on $LaAlO_3$ will inevitably be twinned themselves. A twinned film will have many twin boundaries in it, which will alter the electrical transport properties. This aspect is seldom considered in the literature. Neither the $SrTiO_3$ nor $NdGaO_3$ substrates used were twinned, so sufficiently thin epitaxial films grown on these substrates should be coherently strained without twin boundaries.

The targets used in this study were polycrystalline discs 3 cm in diameter (Praxair Surface Technologies, US, 99.9% purity). The surface of the target was prepared by grinding on fine emery paper immersed in acetone.

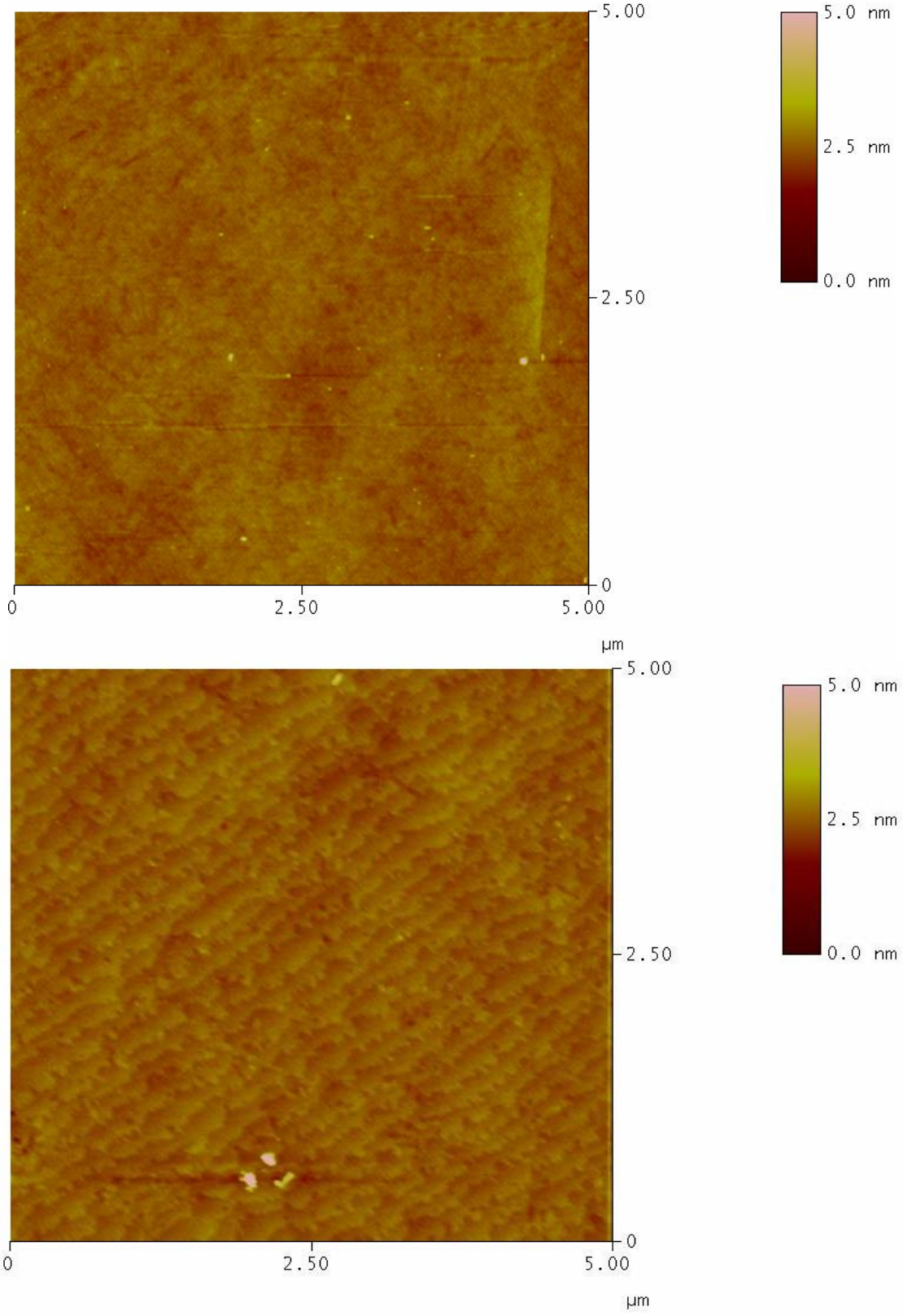

Figure 4.1. AFM scans for a $SrTiO_3$ (001) substrate before (upper diagram) and after (lower diagram) immersion in the NH_4F-HF buffer solution and annealing.

4.2 Film deposition

The films were deposited in the 'Mark X' deposition system, which is a dedicated chamber for oxide deposition. A schematic diagram of the deposition system used is given in Figure 4.2. The actual growth procedure was as follows. The substrates were positioned on a 0.05 mm thick pre-oxidised Fecralloy foil. Fecralloy is a commercially available alloy of Fe and Cr that is highly oxidation resistant. An electric current was passed through the foil and, due to Joule heating, the foil acted as a heater. The temperature of the foil was estimated by optical and infra-red pyrometry to be 1100°C. The substrate temperature was estimated to be 700-800°C, due primarily to radiative coupling between the heater foil and substrate. The target-substrate distance was maintained at 80 mm.

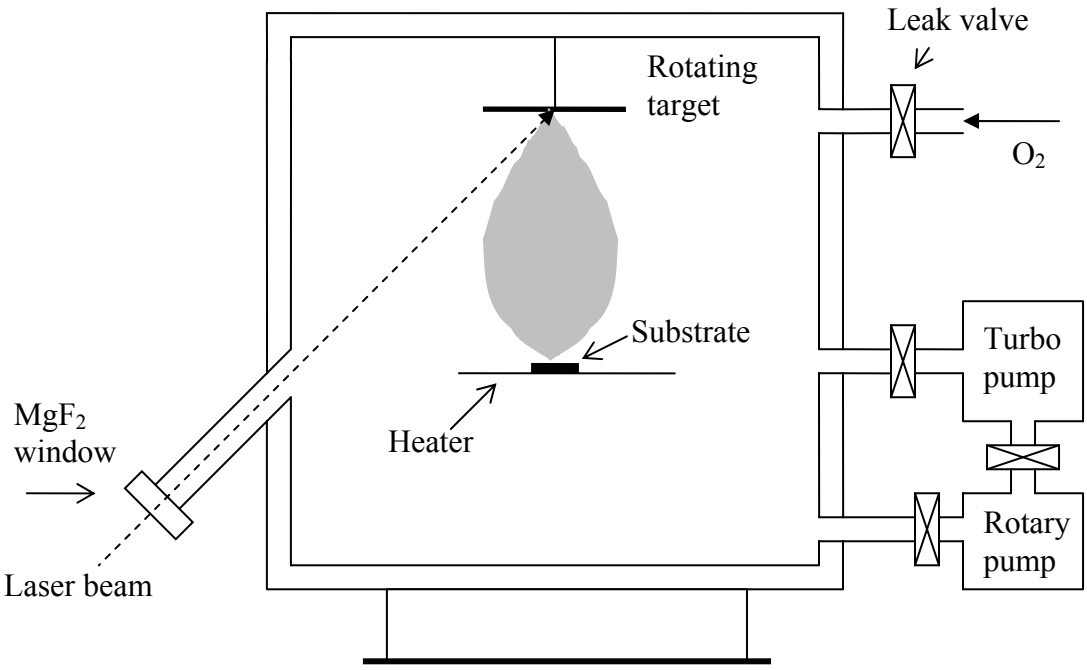

Figure 4.2. A schematic diagram of the 'Mark X' PLD deposition system used in this study.

The vacuum chamber was pumped down to 10^{-6} mbar overnight, (as opposed to 10^{-10} mbar after baking-out an ultra-high vacuum system). A current of 34 A was passed through the heater for an hour to outgas the chamber and to heat the substrate to its deposition temperature.

A Lambda Physik KrF excimer laser (λ=248 nm) was then used to fire 20 ns pulses at a frequency of 1 Hz through an MgF_2 window onto the rotating target. The rotation of the target ensured that the beam did not leave an unduly deep trench in the target. The laser beam carried enough energy to vaporise the target material, and produce a plume of ablated species. The particles gain energy from the beam and fall onto the substrate below. The *maximum* laser beam energy was set to roughly 220 mJ, as measured after passing along the external optical pathway but before entering the chamber. The energy of the beam incident on the target was 90% of 220 mJ (i.e. about 198 mJ). The other 10% was absorbed in passing through the MgF_2 window, whose transmittance was checked periodically between depositions. The *average* beam energy was 216±1 mJ before entering the chamber, (194±1 mJ after entering the chamber). The beam was incident upon a region approximately 15 mm^2, which gave a laser fluence of 1.4 Jcm^{-2}. The target was pre-ablated for 200 pulses to remove any foreign material from the surface. A typical deposition lasted for around 35 minutes and produced a film about 60 nm thick. The actual film thickness was determined by high-resolution X-ray diffraction, as is discussed in Section 4.3.2 below.

During the deposition 15 Pa of flowing oxygen was leaked through the chamber. The pressure was kept to within 0.1 Pa of the desired value by means of a needle valve (input) and gate valve (output). The oxygen was required for two reasons. Firstly, it helped prevent film deoxygenation as oxygen is relatively more mobile than the other ablated components. Secondly, it helped to thermalise the plume, and prevent high-energy particles from the target hitting the sample and possibly damaging it. The high-energy particles will lose energy during collisions with the oxygen molecules, thereby reducing the chance of damage to the sample.

The as-grown films were then annealed *in situ* for a further hour in approximately 60 kPa of oxygen at the deposition temperature. This was to promote full oxygenation of the sample as inferred from the Curie temperature of $La_{0.7}Ca_{0.3}MnO_3$ films [7]. Finally, the samples were cooled to room temperature over a 60 second period. This cooling rate did not lead to cracking in the film surface as determined by optical microscopy.

4.3 Sample characterization

After growth, the surface of each sample was characterised by atomic force microscopy and the crystallinity and film thickness were investigated by X-ray diffraction.

4.3.1 Atomic force microscopy

The surface morphology of each sample was investigated by tapping mode atomic force microscopy (AFM). AFM is a non-destructive technique that produces a topological map of the film surface. One of the major advantages of this technique is that the image obtained directly corresponds to the surface profile. It is therefore possible to extract quantitative data, e.g. surface roughness or terrace step height, about the surface from the image.

The image is produced by dragging a vibrating cantilever with a Si_3N_4 tip across the surface. There are inter-atomic interactions between the tip and the sample surface that cause the tip to deflect from its equilibrium position. A laser beam is reflected off the back of the cantilever and onto a piezoelectric transducer. The degree of deflection of the tip can be measured by using this piezoelectric transducer together with a feedback loop. The output voltage signal is then used to produce a profile of the surface. The lateral resolution is of the order of a few nanometres and the resolution in the vertical direction is better than 0.1 nm. This makes it possible to observe whether step-flow growth had occurred in the films. Step-flow growth is characterised by uniformly spaced terraces separated by steps of unit cell height. Figure 4.3 shows an image and cross-section for a $La_{0.57}Ca_{0.43}MnO_3$ film on $SrTiO_3$ (001) that exhibited step-flow growth. The lateral spacing between adjacent terraces is ~140 nm and the height of each terrace is 0.4 nm (roughly one unit cell).

One common method of parameterising the smoothness of the film surface is using the root mean square (r.m.s.) roughness. Firstly, a plane is fitted to the data to offset any tilt in the image. The r.m.s value is then given by equation 4.1, where z_i is the deviation from the median plane of the i^{th} data point and n is the number of

.

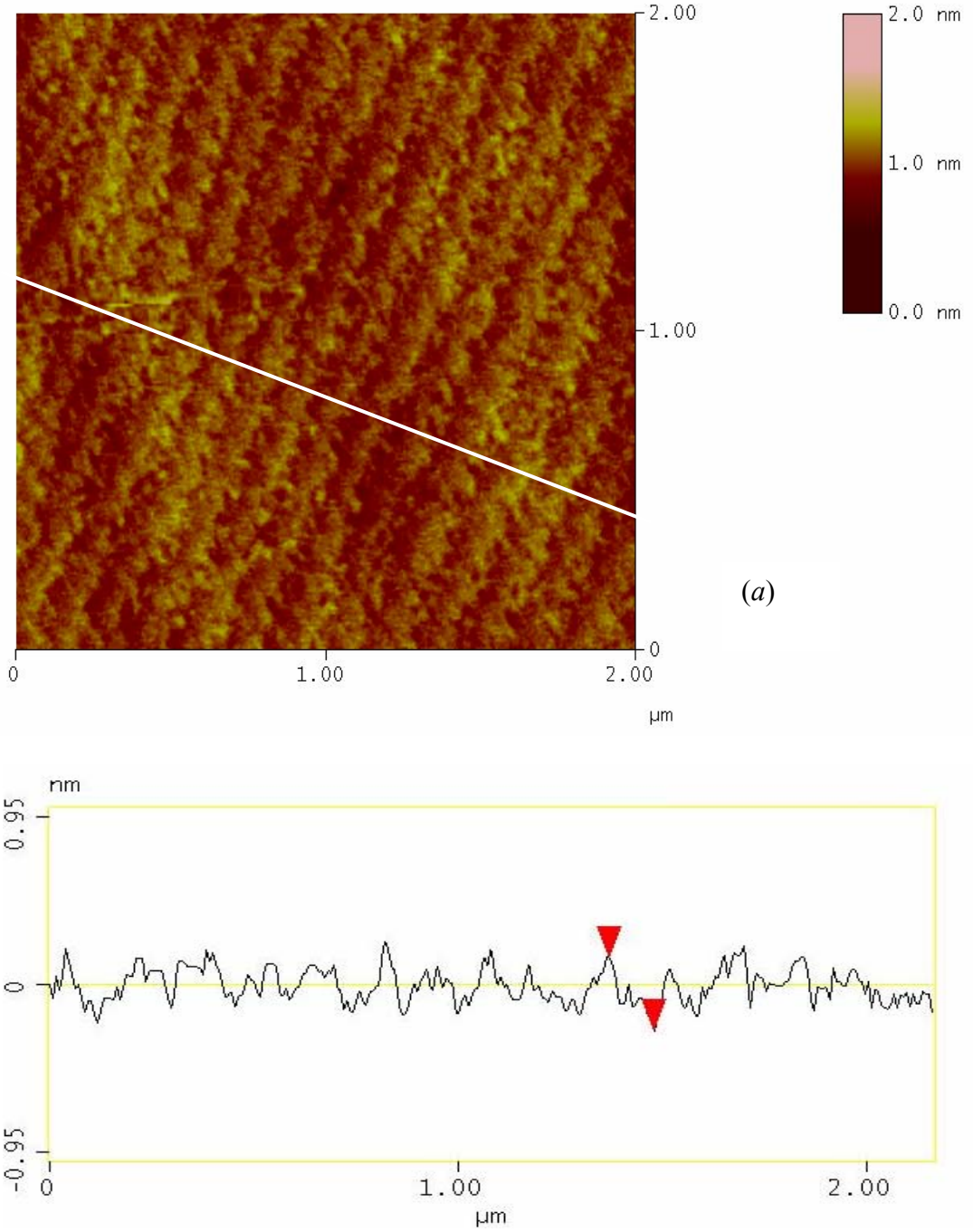

Figure 4.3. (a) A 2 µm × 2 µm atomic force microscope image of a 60 nm film of $La_{0.57}Ca_{0.43}MnO_3$ grown on $SrTiO_3$ (001) that exhibits step-flow growth. (b) A cross section of the scan taken along the white line in (a). The markers correspond to a unit-cell height step.

datapoints in the sample.

$$z_{rms} = \sqrt{\sum_i \frac{z_i^2}{n}} \qquad (4.1)$$

The roughness is closely related to the standard deviation of a statistical distribution. As an example, the roughness of the 2×2 μm^2 area in Figure 4.3(a) is 0.108 nm.

However, roughness on its own is not a very useful quantity for films that show step-flow growth as the roughness value will trivially depend on the spacing between adjacent terraces. This spacing depends on the precise vicinal offcut angle for each substrate. For the film in Figure 4.3, the vicinal offcut angle was calculated to be 0.2º. A more reliable check of the surface quality was the presence (or absence) of step-flow growth and confirmation that the observed step-heights were consistent with the pseudo-cubic unit cell dimension of 3.85 Å for $La_{0.60}Ca_{0.40}MnO_3$. Step-flow growth was seen much more frequently for the films deposited on NH_4F-HF treated $SrTiO_3$ (001).

4.3.2 X-ray diffraction

X-ray diffraction is another powerful tool that can be used to extract quantitative information about the microstructure of laser-ablated thin films. It has a number of advantages as a characterisation technique, namely that it is non-destructive and probes a range of lengthscales from Ångstroms up to micrometres. A beam of X-rays is used to probe reciprocal (**q**) space and extract structural information about the interplanar spacing and hence the crystal structure.

The data were taken using a high-resolution diffractometer[1] using Cu $K_{\alpha 1}$ radiation (λ=0.154056 nm) selected via a 4-bounce germanium (220) monochromator. The inter-planar spacing was probed by means of a θ-2θ scan with the standard Bragg-Brentano geometry. In such a scan, the sample and detector angles are changed in a constant ratio of 1:2. There is constructive interference between the beams diffracted from adjacent atomic planes when the Bragg condition is met. As a

[1] Philips E'Pert MRD PW3050/20

result, there is an intensity peak at angle 2θ in the scan, and the interplanar spacing can be calculated from the Bragg equation 4.2. In this equation, λ is the X-ray wavelength and d_{hkl} is the distance in real space between successive (*hkl*) planes.

$$\lambda = 2d_{hkl}\sin\theta \tag{4.2}$$

One limitation of a θ-2θ scan is that it is difficult to resolve closely matched out-of-plane lattice spacings. In a ω scan (or rocking curve), the 2θ angle is fixed, and the sample is rocked, as depicted in Figure 4.4. This allows small changes in the component of the scattering vector normal to the film surface, and hence small variations in the out-of-plane lattice parameter to be investigated. This is particularly important for epitaxial thin films as the width of the film peak in a ω scan gives information about the coherency of the strain in the film.

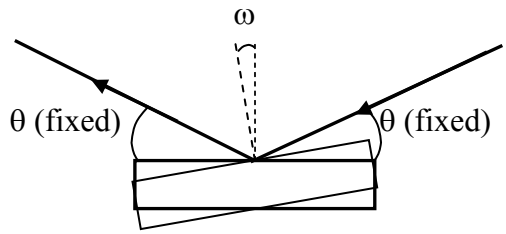

Figure 4.4. Diagram showing the geometry for a ω-scan. The incoming and outgoing beam directions (2θ angle) are held constant.

Due to the finite thickness of the film layer, secondary interference fringes were seen around the layer peak. The film thickness *t* can be found by using equation 4.3 if the X-ray wavelength λ, fringe spacing $\delta\omega$, 2θ and ω values are known [8].

$$t = \frac{\lambda\sin(2\theta-\omega)}{\delta\omega\sin(2\theta)} \tag{4.3}$$

Figure 4.5 shows a typical X-ray scan for a manganite film grown on $NdGaO_3$ (001) which shows a sharp substrate peak (S), a peak due to the manganite layer (L) and interference fringes (F). As can be seen, the number of counts recorded for these secondary fringes is typically 10 counts per second (cps). This count rate is much lower than that recorded for the substrate peak (10^5-10^6 cps) or the main film peak itself (10^3 cps). The error in the positions of the interference fringes is consequently much higher than for the film and substrate peaks and this manifests itself in the thickness calculations. The error in the mean thickness obtained from five pairs of adjacent fringes was typically about 5-10%. This resulted in an absolute uncertainty of 3-6 nm for a typical 60 nm film.

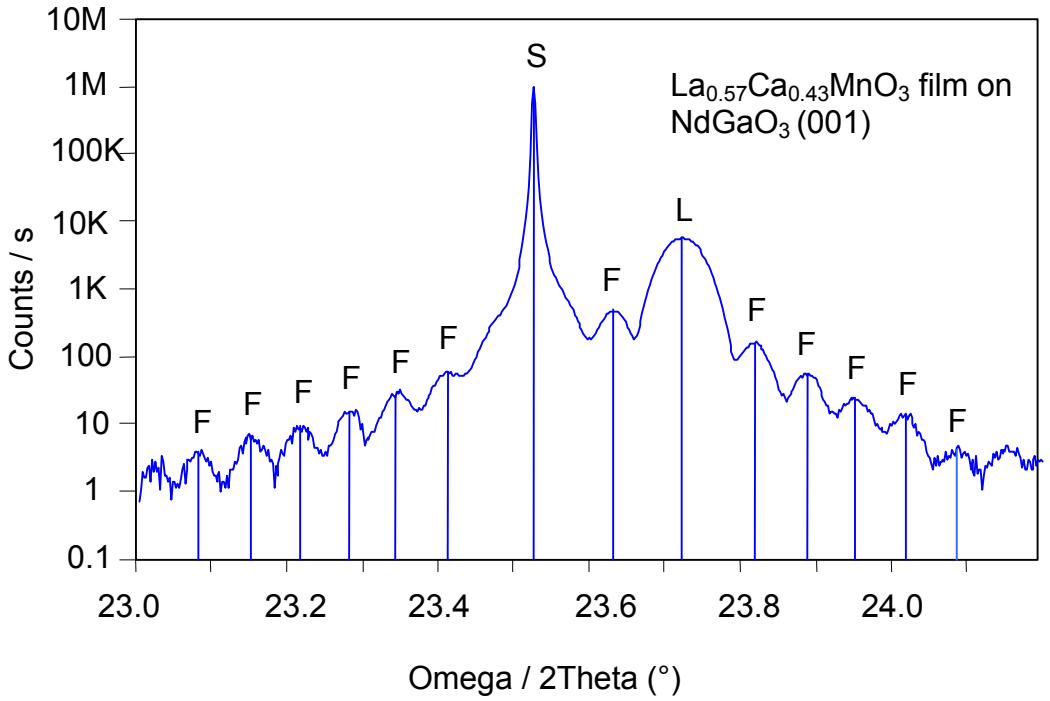

Figure 4.5. An X-ray scan for a 73 nm $La_{0.57}Ca_{0.43}MnO_3$ film grown on $NdGaO_3$ (001). The peak labels refer to the substrate (S), film layer (L), and interference fringes (F) respectively. The thickness is calculated from the spacing between adjacent interference fringes. (The fringe near ω=23.6° does not feature in the calculations.)

4.4 Magnetic measurements

The magnetic properties of the samples were investigated using a Princeton Measurements Corporation vibrating sample magnetometer (VSM)[2]. The VSM vibrates a sample vertically at 83 Hz between four pick-up coils as shown in Figure 4.6. The stray field from the sample dynamically cuts these pick-up coils, and generates an e.m.f. as described below.

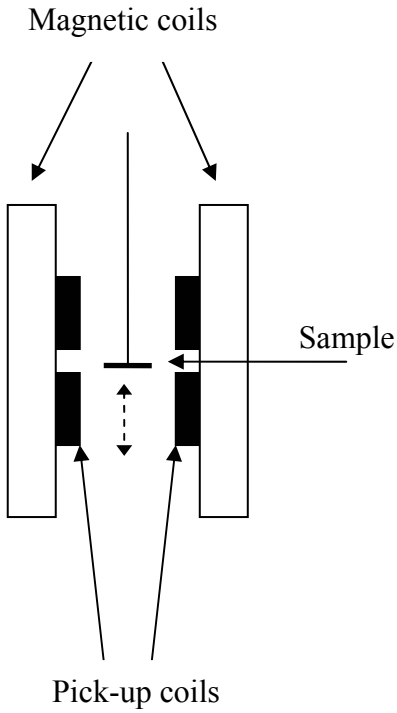

Figure 4.6. Schematic of the VSM.

In SI units, the magnetisation **M** is related to the **H** and **B** fields by

$$\mathbf{B} = \mu_0 (\mathbf{H} + \mathbf{M}) . \qquad (4.4)$$

The external field **H** is set to a known value, so any change in the flux density **B** inside the sample will be due to a change in **M**. The **B** field inside the sample will then generate an e.m.f. in the pick-up coils as the sample vibrates. The e.m.f. ε per turn is then given by Faraday's law.

$$\varepsilon = -\frac{d\Phi}{dt} = -\frac{\partial}{\partial t}\left(\int \mathbf{B} \cdot \mathbf{dS}\right) \qquad (4.5)$$

[2] MicroMag™ 2900

In equation 4.5 Φ is the flux linked by the coils and **dS** is an element of vector area. The magnetic moment of the sample was then found by comparing the e.m.f. thus obtained with that for a small nickel calibration sample. It should be noted that it is only the component of the moment parallel to the direction of the applied field that is detected using this technique due to the orientation of the coils with respect to the applied field.

4.4.1 Cryogenic operation

The VSM has a facility for cooling samples down to 8.5 K. Figure 4.7 shows the experimental set-up used for magnetisation measurements with liquid helium cooling. What follows is a detailed description of the procedure.

A transfer tube was inserted into a storage dewar of liquid helium. The dewar was pressurised to about 500 mbar with gaseous helium, forcing cold helium along two capillary tubes. The delivery capillary ends in the sample zone, whereas the shield capillary doubles back along the transfer line. The shield capillary provides insulation against heat loss from the delivery capillary, and gives an indirect indication of the flow rate along the delivery capillary.

After passing along the delivery capillary, the gaseous He flowed out of a porous copper diffuser and over the sample. The copper diffuser contains a heater and thermocouple to set and measure the temperature respectively. The temperature was maintained by balancing the cooling power from the helium and heating effects due to the heater. Note that the temperature that was recorded was strictly that of the copper diffuser. The sample should not be at a significantly different temperature provided the set temperature is not altered too fast. The helium flow could be regulated by opening or closing a valve. The flow rate was set such that the heater current needed to maintain a constant temperature was about 100 mA. If the heater current were higher, then the helium flow rate would have been higher. This would have wasted helium. Additionally, because the sample zone is a small enclosed space and the sample itself is liable to be buffeted by the helium injected into the sample zone. However, this is not a major problem for robust samples of the type used here. After flowing past the sample, the helium was pumped away to the atmosphere by an

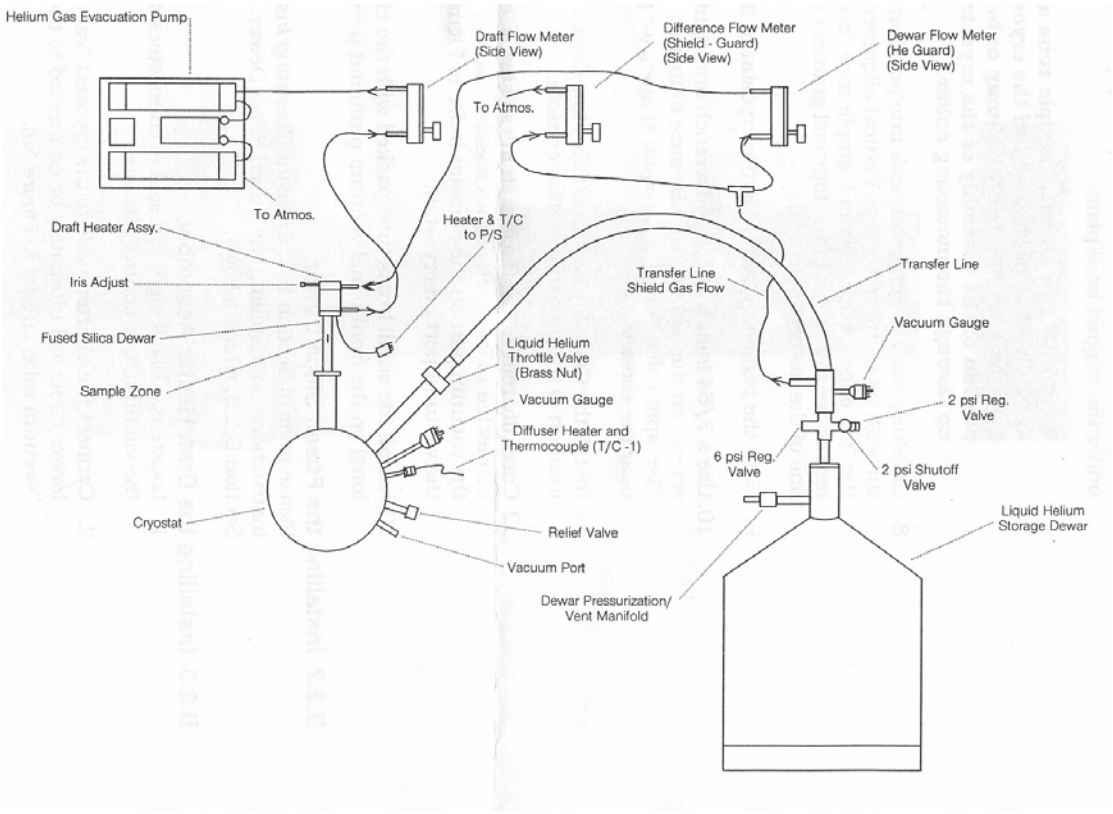

Figure 4.7. Diagram showing the experimental set-up for the VSM with liquid He cooling. (Taken from [9].)

extractor unit. To avoid the extractor unit becoming too cold and covered in frost, room temperature helium from the shield line was flowed into the extractor unit. This mixture of cold and room temperature gas was then pumped away to atmosphere.

4.5 Electrical transport measurements

The d.c. electrical resistivity of the samples was measured as a function of temperature and applied magnetic field. Gold contact pads were deposited using an Emitech K550 sputter coater using a simple metal mask and connected to the sample holder by aluminium wire bonds. Figure 4.8 shows the configuration of contact pads used.

The data were taken using a Keithley 2410 source meter with remote voltage sensing. In this method, the current is altered so that there is a pre-determined constant voltage across the outer pair of contacts. The current required to obtain this

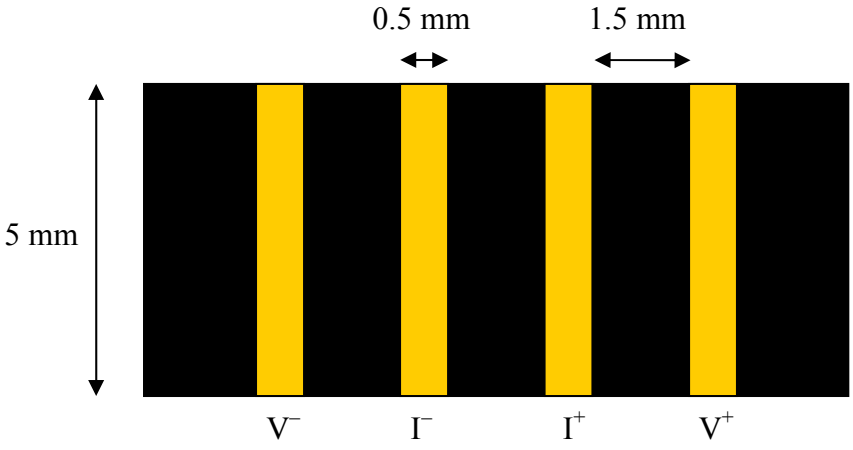

Figure 4.8. A schematic diagram showing the geometry of the gold contact pads used in this study.

voltage is then recorded. By using a 4-point configuration (as opposed to only 2 contacts), there should be no contribution to the measured resistance from the wire-gold pad interface, the so-called contact resistance. The measured resistance R was then converted into resistivity ρ values by using equation 4.6, where A is the cross-sectional area that the current flows through and l is the distance between the current contacts.

$$\rho = \frac{RA}{l} \tag{4.6}$$

There is some degree of ambiguity as to the appropriate cross-sectional area to use in equation 4.6, as the value will depend on the precise path the current takes through the film. Throughout this work, it has been assumed that the current flows uniformly throughout the width of the film. The resistivity values obtained should be treated an upper bound, as the area the current travels through may be restricted, e.g. if there is phase separation. However, it should be noted that the main aim of the electrical transport measurements was to determine the temperature (if any) of a transition from an insulating state (defined as $d\rho/dT < 0$) to a metallic state (defined as $d\rho/dT > 0$). This can be done from resistance values alone, but the absolute resistivity values are included for comparison with other materials.

The sample resistance was measured as a function of temperature using a continuous flow cryostat similar to that used for the magnetic measurements. In

addition, it was possible to apply a variable magnetic field of up to 400 mT. The cooling and heating rate and the applied magnetic field were all computer controlled by a LabView™ program written by Dr Gavin Burnell. It is important to note that R and hence ρ were measured along the [100] direction of the film. The film is highly oriented and the resistivity is anisotropic. This anisotropy means that it is not feasible to use the Van der Pauw technique for obtaining the resistivity of a uniform sheet from resistance data [10].

References for Chapter 4

[1] M. Kawasaki, K. Takahashi, T. Maeda, R. Tsuchiya, M. Shinohara, O. Ishiyama, T. Yonezawa, M. Yoshimoto and H. Koinuma, *Atomic Control of the $SrTiO_3$ Crystal Surface.* Science **266**, 1540-2 (1994).

[2] R. Shreekala, M. Rajeswari, R.C. Srivastava, K. Ghosh, A. Goyal, V.V. Srinivasu, S.E. Lofland, S.M. Bhagat, M. Downes, R.P. Sharma, S.B. Ogale, R.L. Greene, R. Ramesh, T. Venkatesan, R.A. Rao and C.B. Eom, *Ferromagnetism at room temperature in $La_{0.8}Ca_{0.2}MnO_3$ thin films.* Appl. Phys. Lett. **74**, 1886-8 (1999).

[3] W. Prellier, M. Rajeswari, T. Venkatesan and R.L. Greene, *Effects of annealing and strain on $La_{1-x}Ca_xMnO_3$ thin films: A phase diagram in the ferromagnetic region.* Appl. Phys. Lett. **75**, 1446-8 (1999).

[4] G.J. Snyder, R. Hiskes, S. DiCarolis, M.R. Beasley and T.H. Geballe, *Intrinsic electrical transport and magnetic properties of $La_{0.67}Ca_{0.33}MnO_3$ and $La_{0.67}Sr_{0.33}MnO_3$ MOCVD thin films and bulk material.* Phys. Rev. B **53**, 14434-44 (1996).

[5] K. Dörr, J.M. De Teresa, K.-H. Müller, D. Eckert, T. Walter, E. Vlakhov, K. Nenkov and L. Schultz, *Preparation and properties of epitaxial $La_{0.7}Ca_{0.3}MnO_{3-\delta}$ films with reduced carrier density.* J. Phys.: Condens. Mat. **12**, 7099-109 (2000).

[6] M.G. Norton and J. Bentley, *Reflection electron microscopy observations of twinning in $LaAlO_3$.* J. Mater. Sci. Lett. **15**, 1851-3 (1996).

[7] N. Malde, P.S.I.P.N. de Silva, A.K.M. Akther Hossain, L.F. Cohen, K.A. Thomas, J.L. MacManus-Driscoll, N.D. Mathur and M.G. Blamire, *Influence of oxygen stoichiometry on Raman phonon spectroscopy, lattice parameters and physical properties of $La_{0.7}Ca_{0.3}MnO_3$ thin films.* Solid State Commun. **105**, 643-8 (1998).

[8] W.J. Bartels and W. Nijman, *X-ray double-crystal diffractometry of $Ga_{1-x}Al_xAs$ epitaxial layers.* J. Cryst. Growth **44**, 518-25 (1978).

[9] *Princeton Measurement Corporation MicroMag™ 2900 Vibrating Sample Magnetometer Manual*. p. 102.

[10] L.J. van der Pauw, *A Method of Measuring the Resistivity and Hall Coefficient on Lamellae of Arbitrary Shape.* Philips Tech. Rev. **20**, 220-4 (1958-9).

Chapter 5 Pinpointing the ferromagnetic / charge-order phase boundary in thin film samples of $La_{1-x}Ca_xMnO_3$

5.1 Introduction

The compositions in the $La_{1-x}Ca_xMnO_3$ family that exhibit the greatest number of exciting features are typically found close to a phase boundary. This is especially true for compositions near the low-temperature phase boundary between the ferromagnetic and charge-ordered phases. In the bulk material this phase boundary occurs close to x=0.50 and there is a mixed-phase region around the boundary. It is likely that the same interesting phenomena are also present around the FM-CO phase boundary in epitaxial $La_{1-x}Ca_xMnO_3$ films, although the location of this boundary is unclear at present. In this section, the effect of the substrate-induced strain is investigated and a preliminary phase diagram produced for coherently strained $La_{1-x}Ca_xMnO_3$ films grown on $SrTiO_3$ (001).

5.2 Motivation

Electron-lattice coupling in the manganites has been shown to have a major influence on properties. The strain induced in an epitaxial film can alter the degree of coupling. Furthermore, the type of strain (compressive or tensile) has been shown to influence the ground state of films [1]. A further example of the effect of the substrate is found in the magnetic anisotropy of epitaxial films. Studies have shown that the magnetic anisotropy of epitaxial films follows the symmetry of the substrate with 4-fold symmetry for $La_{0.7}Sr_{0.3}MnO_3$ films on $SrTiO_3$ (001) [2], and 2-fold symmetry for $La_{0.7}Ca_{0.3}MnO_3$ films on $NdGaO_3$ (001) [3] and $La_{0.7}Sr_{0.3}MnO_3$ films on $SrTiO_3$ (110) [2]. However, it should be noted that the effects of stress-induced anisotropy and crystalline anisotropy cannot be easily separated. Unstrained $La_{0.7}Ca_{0.3}MnO_3$ [3] and single crystals of $La_{0.7}Sr_{0.3}MnO_3$ [2] have been shown to possess uniaxial anisotropy. However, twinning in single crystals adds further complications. Further evidence for the substrate dependence was seen by Wu *et al.* [4]. They studied various compositions of $La_{0.67-x}Pr_xCa_{0.33}MnO_3$ films grown on $SrTiO_3$, $NdGaO_3$ and $LaAlO_3$ and found that the make-up of a phase-separated mixture depended on the type of strain via the choice of substrate.

In the manganites, there is competition between the double exchange (DE) mechanism and Jahn-Teller (JT) distortions. DE favours (pseudo-)cubic symmetry and will lead to a ferromagnetic metallic state. Conversely, the JT distortion reduces the symmetry of the MnO_6 octahedra to orthorhombic and localises the e_g electron on the Mn^{3+} ion. Polaron hopping leads to insulating behaviour ($d\rho/dT < 0$), as shown in Section 2.3.7. The principle effects of substrate-induced strain are to alter the crystal symmetry and change the lattice parameters. These changes can alter the balance between the competing effects of DE and JT and thus alter the properties of the ground state.

While the $La_{1-x}Ca_xMnO_3$ system has been extensively studied, the majority of work has been on the bulk material and the behaviour of the bulk material, if not the underlying physical processes, is relatively well understood. The work on epitaxial manganite films has largely been restricted to simple studies comparing the film properties with those of bulk samples [5,6] or films of the same composition grown on different substrates [1,7,8]. There have been very few systematic studies of films of different compositions grown on the same substrate. In one such study, Prellier *et al.* investigated the properties of $La_{1-x}Ca_xMnO_3$ films in the range $0<x<0.5$ grown on $LaAlO_3$ (100) [9]. They observed ferromagnetic *metallic* behaviour for $x<0.2$ as shown in Figure 5.1, which is in contrast with the bulk material which is a ferromagnetic *insulator*. They attributed this behaviour to the compressive strain (~1%) from the substrate and the effects of post-annealing the films in oxygen. The compressive strain will increase the bandwidth and make the ferromagnetic metallic phase more stable. However, as mentioned previously, $LaAlO_3$ readily forms twins and this complicates the picture. It is interesting to note that T_C increased after subsequent annealing, which is further evidence that the exact oxygen stoichiometry can affect the properties of the film.

The low-temperature phase boundary between the ferromagnetic and charge-ordered phases is a common region for phase separation studies [10,11]. The precise location of this boundary may vary between bulk polycrystalline samples and thin films. In this chapter a systematic study of films grown on $SrTiO_3$ (001) with compositions in the range x=0.40-0.45 is performed. The films are characterised by their magnetic and electrical properties and a simple phase diagram produced.

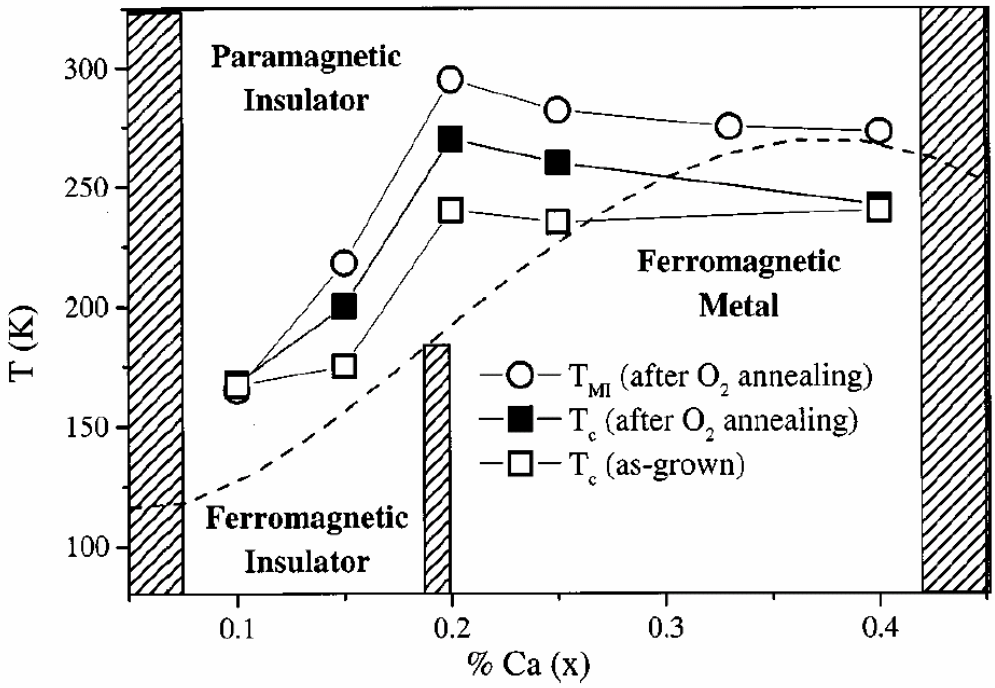

Figure 5.1. A phase diagram for $La_{1-x}Ca_xMnO_3$ films deposited on $LaAlO_3$ (001). T_C and T_{MI} are taken to be the inflection points in M(T) and ρ(T) respectively. The dashed line refers to the expected phase boundary for bulk $La_{1-x}Ca_xMnO_3$ from the phase diagram in reference [12]. The shaded regions indicate possible coexistence regions. (Taken from [9].)

5.3 Film deposition and characterisation

To investigate the position and nature of the low-temperature FM-CO phase boundary, a series of $La_{1-x}Ca_xMnO_3$ films was grown on $SrTiO_3$ (001) and $NdGaO_3$ (001) substrates by PLD. Preliminary studies had found that $La_{0.60}Ca_{0.40}MnO_3$ showed metallic behaviour at low temperatures and that $La_{0.55}Ca_{0.45}MnO_3$ did not have a metallic ground state, so films with nominal doping levels of x=0.40, 0.41, 0.42, 0.43, 0.44 and 0.45 were used. The film thicknesses were in the range 50-60 nm and the exact thickness for each film was obtained from high-resolution X-ray diffraction scans. It was found that 60 nm films were generally coherently strained and that thicker films were likely to have partially relaxed.

5.3.1 X-ray diffraction

X-ray diffraction scans revealed single narrow peaks, confirming that the films were coherently strained. Figure 5.2 shows ω scans for the (002) film peak for a $La_{0.60}Ca_{0.40}MnO_3$ film on $SrTiO_3$ and the (002) $SrTiO_3$ substrate peak. The FWHM value was 0.11º for the film and 0.012º for the substrate.

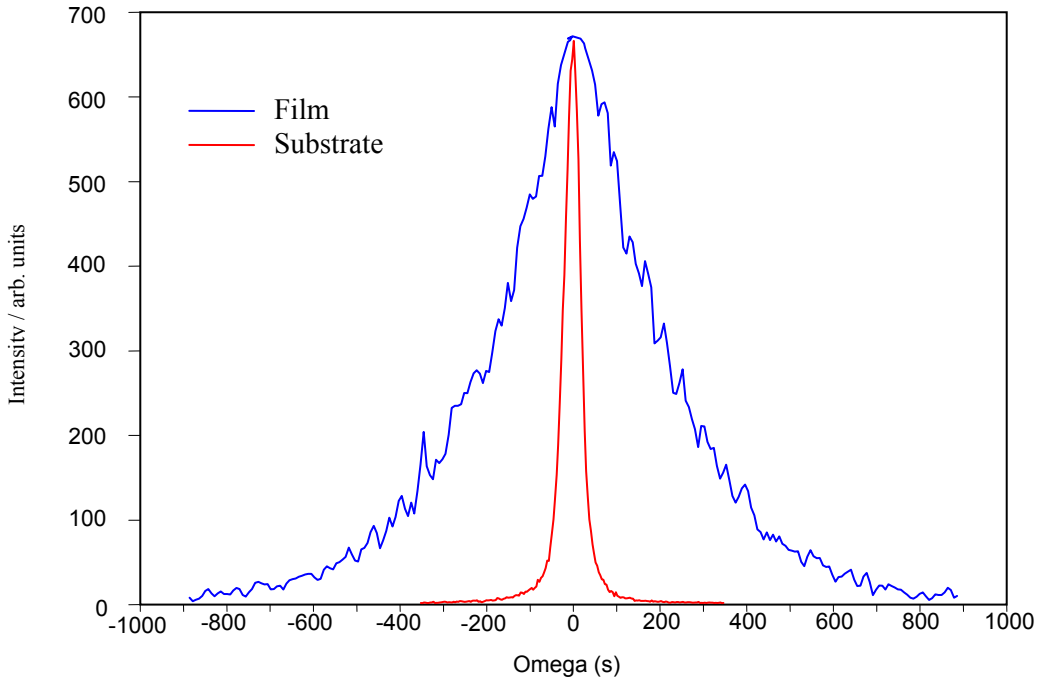

Figure 5.2. Rocking curve for the (002) peaks for a $La_{0.60}Ca_{0.40}MnO_3$ film on $SrTiO_3$ (001) and the substrate itself.

Figure 5.3 shows the variation in the spacing of the d_{001} planes as a function of calcium doping for nominally 60 nm films grown on $SrTiO_3$ (001) and $NdGaO_3$ (001). The indexing of the film refers to the pseudo-cubic unit cell. There is evidence for a systematic decrease in c with increasing calcium content for the films grown on both substrates. This follows the same trend as the bulk material. The d_{001} spacing is closer to the bulk value for the films on $NdGaO_3$. This is consistent with the relative lattice mismatches (~0.1% for $NdGaO_3$ and ~1% for $SrTiO_3$) and associated strain states.

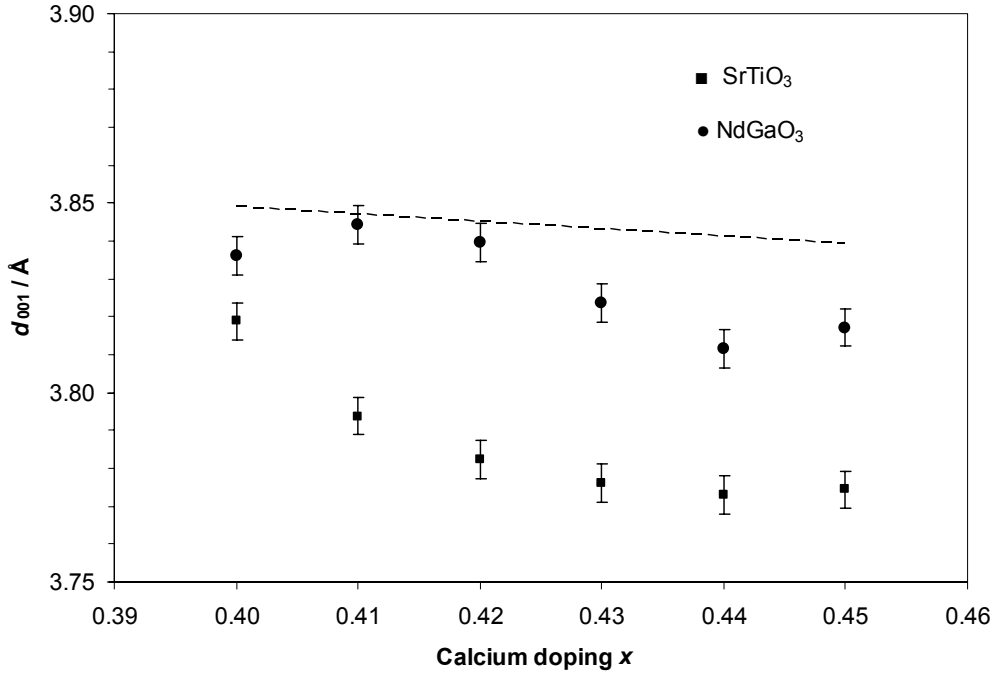

Figure 5.3 Out-of-plane lattice parameter vs. composition for nominally 60 nm $La_{1-x}Ca_xMnO_3$ films grown on $SrTiO_3$ (001) (■) and $NdGaO_3$ (001) (●). The dotted line gives a rough indication of the pseudo-cubic lattice parameter for bulk $La_{1-x}Ca_xMnO_3$.

The reduction in the out-of-plane lattice parameter compared with the bulk value can be quantified by considering Poisson's ratio ν and the components of the in-plane strain ε_{xx} and ε_{yy} and the out-of-plane strain ε_{zz}. The relationship between the components of the strain tensor and ν is given by equation 5.1.

$$\varepsilon_{zz} = -\frac{\nu(\varepsilon_{xx} + \varepsilon_{yy})}{1-\nu} \qquad (5.1)$$

The in-plane strain was calculated by comparing the in-plane lattice parameters of the film and the substrate, and the out-of-plane strain was found by comparing the observed d_{001} spacing with the bulk pseudo-cubic lattice parameter for each $La_{1-x}Ca_xMnO_3$ composition. Note that the precise strain state will depend on the level of Ca doping as the lattice parameters of $La_{1-x}Ca_xMnO_3$ vary with x. For the films deposited on cubic $SrTiO_3$ (001), the in-plane strains ε_{xx} and ε_{yy} are equal and equation 5.1 reduces to

$$\varepsilon_{zz} = -\frac{2\nu\varepsilon_{xx}}{1-\nu}. \qquad (5.2)$$

Figure 5.4 shows the values of ν for the films on $SrTiO_3$ (001) obtained from the calculated strain states. As can be seen, ν lies in the range 0.2-0.3, which is slightly below the value of ν=0.38 obtained for $La_{0.67}Ca_{0.33}MnO_3$ [13] and $La_{0.8}Ca_{0.2}MnO_3$ films [14]. Note that this is still less than the volume preserving value of ν=½.

For the films on $NdGaO_3$ (001), the induced strain is again tensile but due to the orthorhombic crystal symmetry of this substrate, the strain in the [100] and [010] film directions will be unequal and equation 5.1 must be used to calculate ν. Additionally, because the true unit-cell of $La_{1-x}Ca_xMnO_3$ is also orthorhombic, the precise strain will depend on the relative orientation of the film and substrate. Figure 5.4 shows the calculated values of ν for the films on $NdGaO_3$ (001). The values of ν for this set of films lie in the range 0.1-0.4 and in general show little dependence on x. As for the films on $SrTiO_3$, these values are slightly smaller than the values reported in the

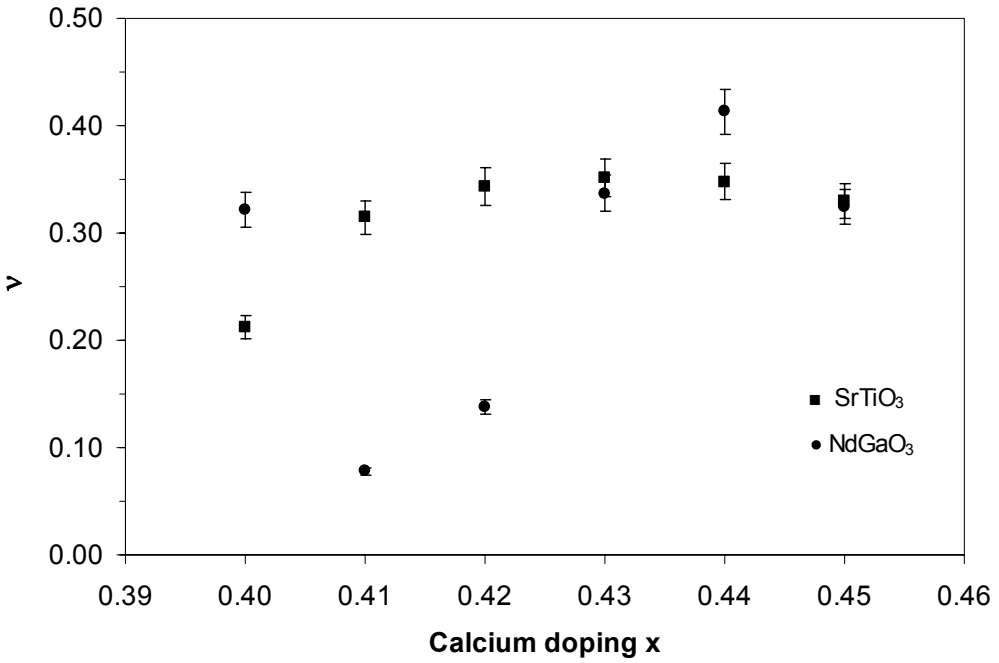

Figure 5.4. Poisson's ratio ν as a function of Ca doping for $La_{1-x}Ca_xMnO_3$ films deposited on $SrTiO_3$ (001) (■) and $NdGaO_3$ (001) (●).

literature [13,14] and are also less than the volume preserving value of ν=½. Note that the $La_{0.59}Ca_{0.41}MnO_3$ and $La_{0.58}Ca_{0.42}MnO_3$ films on $NdGaO_3$ have d_{001} values that are closer to the pseudo-cubic bulk value and the corresponding values for ν are reduced.

The thickness of each film was obtained from the spacing of interference fringes seen in ω-2θ scans as described in Section 4.3.2. Table 5.1 below shows the results for each composition. The values obtained for the films on $SrTiO_3$ and $NdGaO_3$ agreed to within the error of the measurement.

Calcium content	Thickness / nm
0.40	56
0.41	60
0.42	59
0.43	60
0.44	56
0.45	54

Table 5.1. Thicknesses of $La_{1-x}Ca_xMnO_3$ films grown on $SrTiO_3$ as estimated from high resolution X-ray diffraction scans. The error in each of the thicknesses is ±3 nm.

5.3.2 Atomic force microscopy scans

The surface morphology of the films on $SrTiO_3$ was investigated by atomic force microscopy (AFM). The resulting scans are shown in Figure 5.5. None of the films showed strong step-flow growth, although the scan for x=0.40 shows weak unit-cell steps. The remainder of the films showed island-type growth. All of the films were smooth, showed no significant outgrowths and had r.m.s. roughness values in the range 0.1-0.4 nm.

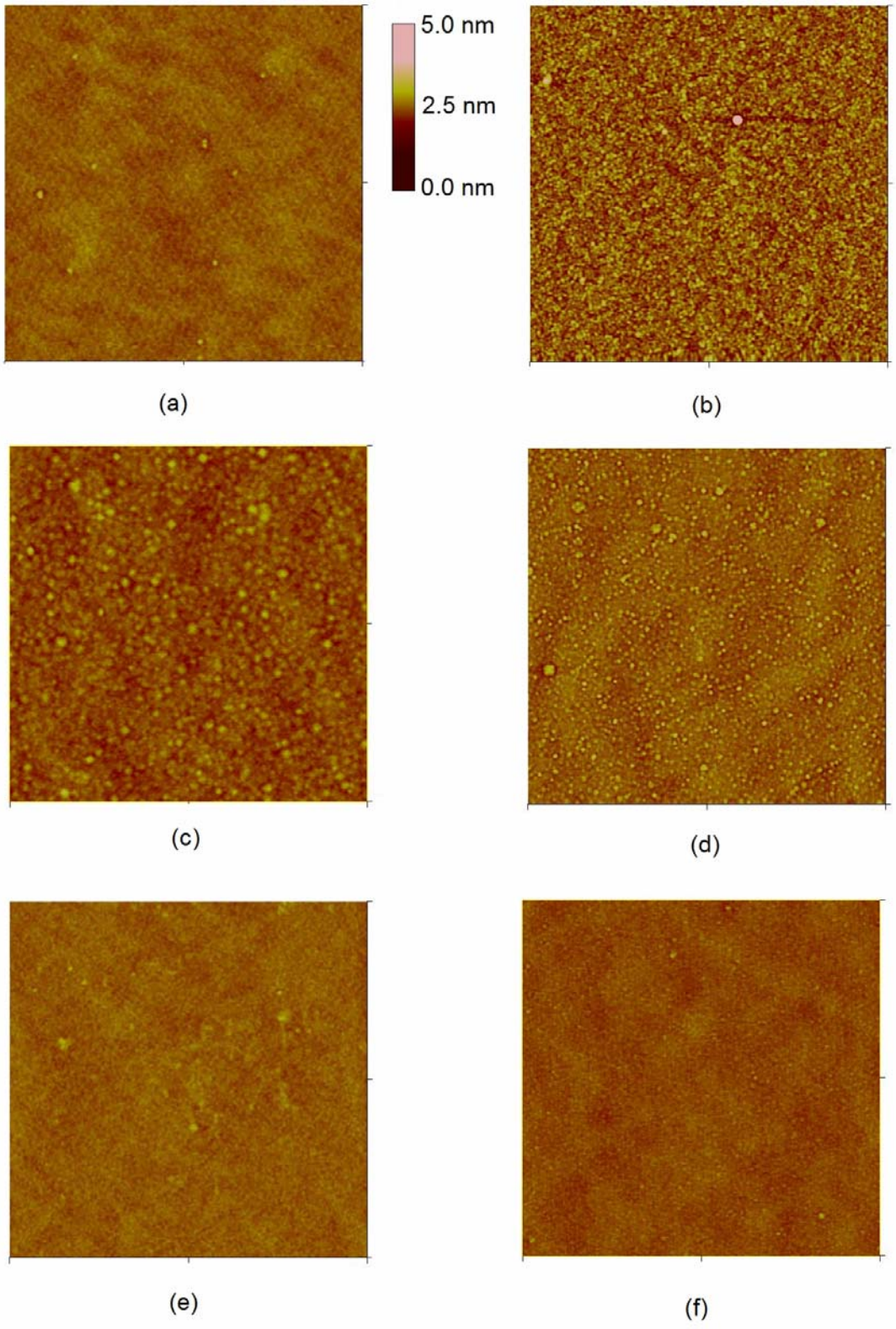

Figure 5.5. 5×5 μm² AFM scans for $La_{1-x}Ca_xMnO_3$ films grown on NH_4F-HF treated $SrTiO_3$ (001) with (a) x=0.40, (b) x=0.41, (c) x=0.42, (2×2 μm² scan) (d) x=0.43, (e) x=0.44 and (f) x=0.45.

5.4 Electrical transport measurements

The majority of the remainder of this chapter is concerned exclusively with the films grown on $SrTiO_3$ (001). Section 5.7 describes briefly the properties of the films on $NdGaO_3$ and offers some comparison between the behaviour of the two sets of films.

The d.c. electrical resistivity of the $La_{1-x}Ca_xMnO_3$ films deposited on $SrTiO_3$ was measured along the [100] film direction as a function of temperature in zero magnetic field. The geometry was as described in Section 4.5. The results are shown in Figure 5.6, from which it can be seen that there is insulating behaviour (defined as $d\rho/dT < 0$) at 300 K for all the compositions. Metallic-like behaviour (defined as $d\rho/dT > 0$) is only observed at low temperature for x=0.40 and 0.41. The resistivities involved (typically 10^6-10^7 μΩcm at room temperature) are much higher than for a good metal, e.g. ρ=1.7 μΩcm for copper at 295 K [15], and are comparable with those

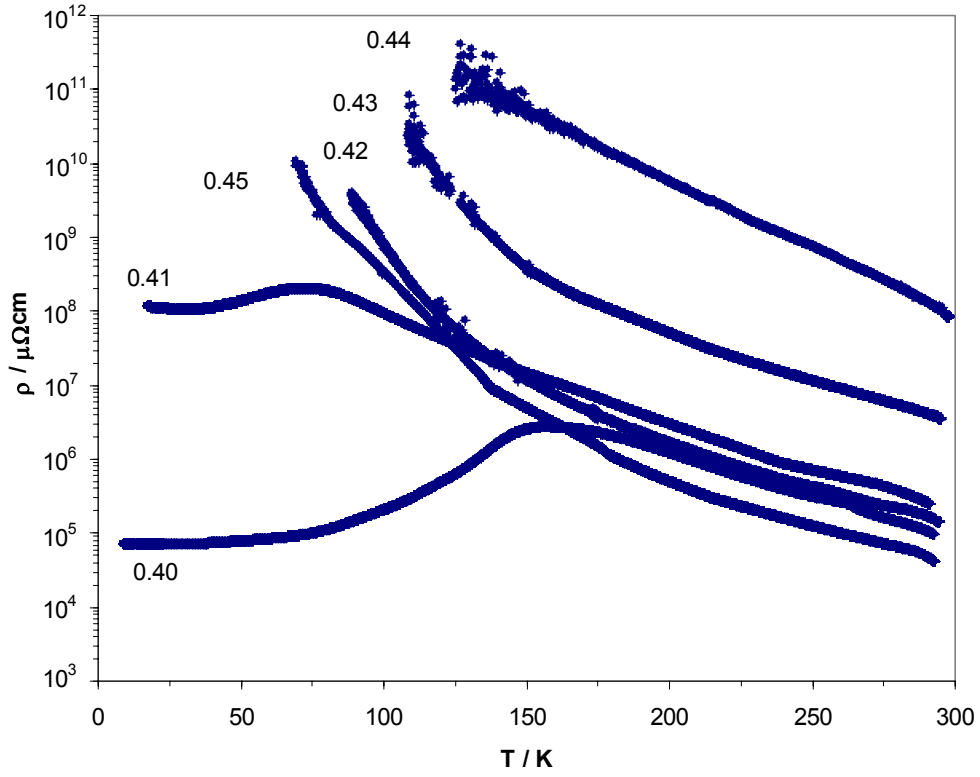

Figure 5.6. Zero field resistivity vs. temperature for approximately 60 nm $La_{1-x}Ca_xMnO_3$ films on $SrTiO_3$ (001).

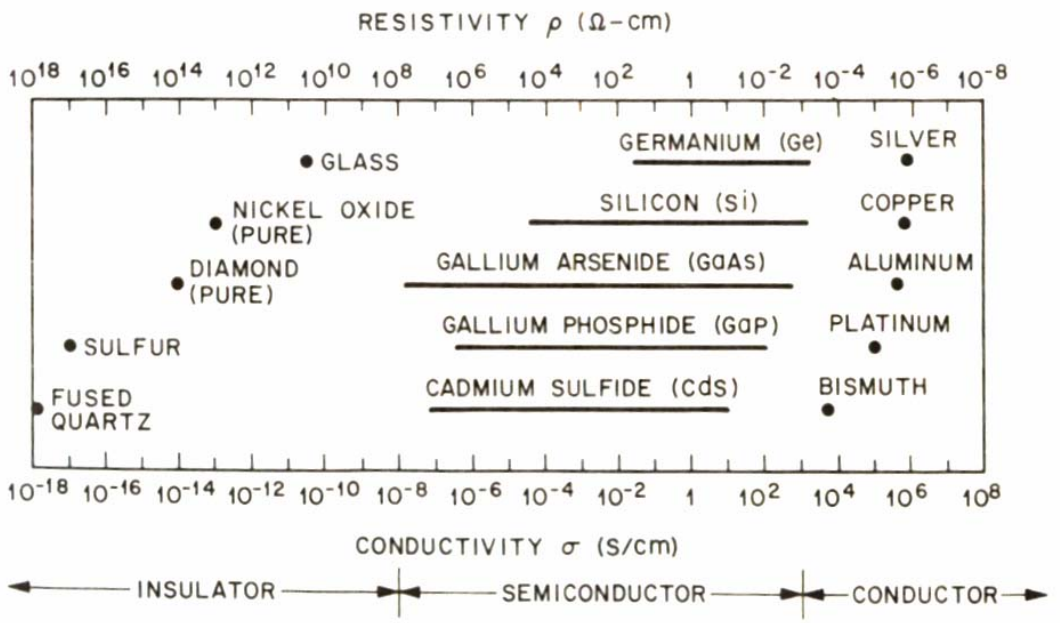

Figure 5.7. Resistivity values at room temperature for some common metals, semiconductors and insulators. (Taken from [16].)

of a typical semiconductor, as shown in Figure 5.7. The residual resistivity of the $La_{0.60}Ca_{0.40}MnO_3$ film was 7×10^4 μΩcm compared with 10^{-4} μΩcm for copper [17]. Furthermore, the residual resistivity for the x=0.40 film is 2 orders of magnitude greater than seen in $La_{2/3}Ca_{1/3}MnO_3$ films [18]. This difference is surprising but not unexpected given that these films appear to be close to the limit of metallic behaviour.

Note that there is a systematic increase in the room-temperature resistivity for the $La_{1-x}Ca_xMnO_3$ films with $0.40<x<0.44$. This is consistent with the supposition that in this region as the Ca content increases the size of the ferromagnetic regions in the sample decreases and consequently the resistivity increases. However, the data for the $La_{0.55}Ca_{0.45}MnO_3$ film does not support this trend. The reason for this anomaly is unclear, although in bulk $La_{1-x}Ca_xMnO_3$ the room-temperature resistivity decreases as the Ca content increases [19].

The metal-insulator transition temperatures T_{MI}, which were taken to be the peak of the $\rho(T)$ curve, were 155 K and 70 K for x=0.40 and 0.41 respectively. Both transition temperatures are suppressed compared with the bulk material (~250 K). The lack of metallic behaviour at low temperature for the films with x=0.42, 0.43, 0.44 and 0.45 is in contrast to the behaviour seen in the bulk material. In the bulk

material, these compositions should undergo a metal-insulator transition at about 230-240 K. The substrate-induced strain appears to have affected the ground state of the $La_{1-x}Ca_xMnO_3$ system and moved the low-temperature boundary between the metallic and insulating states to lower levels of Ca doping. Insulating behaviour has been seen in ultra-thin (2.4 nm) $La_{0.67}Ca_{0.33}MnO_3$ films [18], but the authors attributed this to the thickness of the sample. A 54 nm film from the same work showed the standard metal-insulator transition, albeit slightly suppressed with a T_{MI} of 240 K.

5.5 Magnetic measurements

From the resistivity data in the previous section, it seems that the limit of metallic behaviour for nominally 60 nm $La_{1-x}Ca_xMnO_3$ films on $SrTiO_3$ (001) is now at x=0.41. However, this result does not imply that there are no ferromagnetic clusters for compositions with x>0.41, but rather that any FM clusters present are sufficiently small so that there is not a conductive path throughout the sample. To gain further insight into the phase composition in these films, various magnetic properties were measured using the vibrating sample magnetometer (VSM).

5.5.1 Magnetisation vs. applied field

The magnetisation M was measured as a function of the applied field H. This was done at 20 K, which was the lowest value at which the sample temperature was stable to better than ±0.1 K over a timescale of 1000 s. It was assumed that any phase transitions would have occurred by 20 K and the films would be in their ground state. The results of $M(H)$ measurements are shown in Figure 5.8 with the contribution from the diamagnetic substrate removed.

The large magnetic hysteresis observed for x=0.40 and x=0.41 is behaviour typical of a ferromagnet and suggests that there are significant ferromagnetic regions in these samples. Conversely, the data for x=0.42-0.45 show a much smaller degree of hysteresis, which indicates smaller ferromagnetic regions. The largest saturation moment for the second group of films corresponds to just 5% of the film volume being saturated.

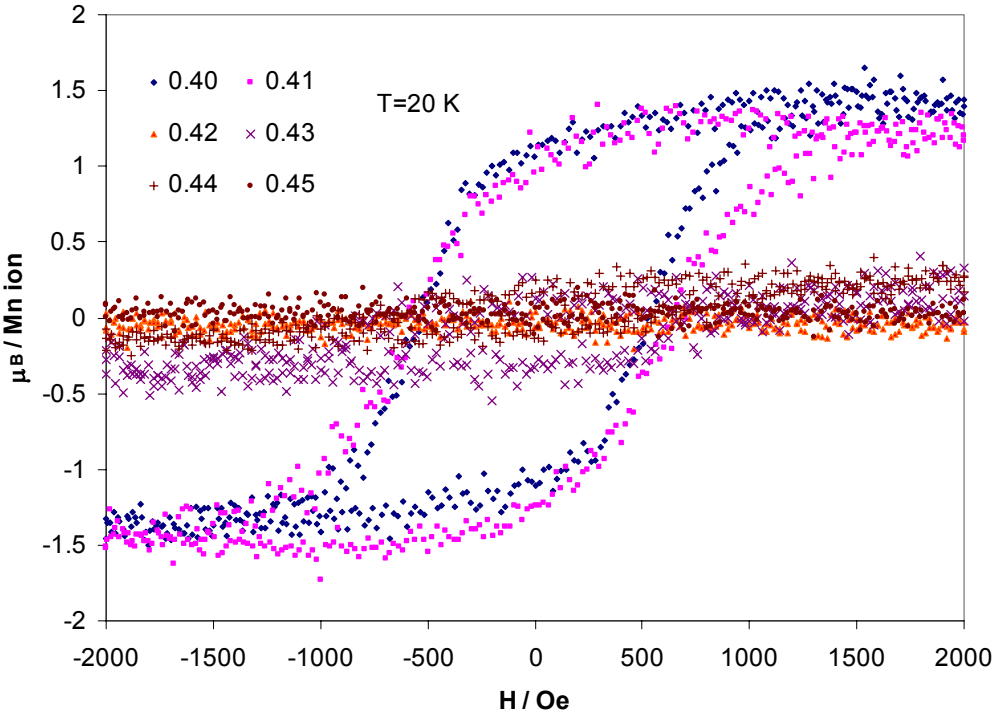

Figure 5.8. Magnetisation vs. applied field at 20 K for $La_{1-x}Ca_xMnO_3$ films on $SrTiO_3$ (001). The contribution from the diamagnetic substrate has been subtracted.

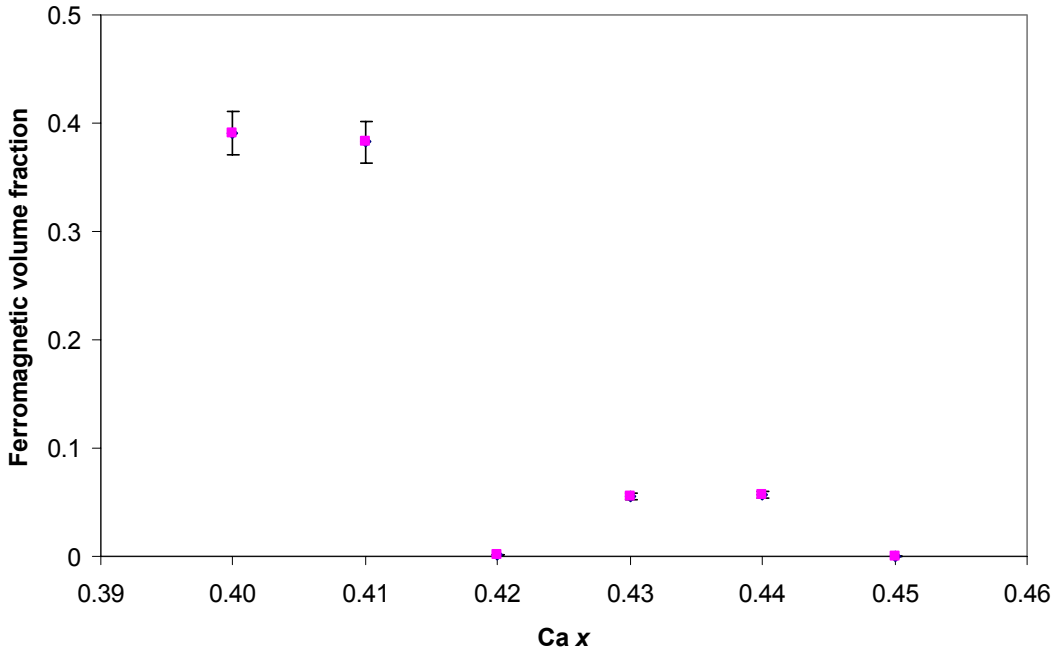

Figure 5.9. Ferromagnetic volume fraction as a function of Ca doping.

The expected saturation moment can be calculated from considering the filling of the Mn 3d orbitals, provided we can assume that the other ions present are non-magnetic and the orbital angular momentum is completely quenched. Due to the strong Hund coupling, all the 3d electrons will be spin-aligned. Each Mn^{3+} ion should therefore contribution 4 μ_B and each Mn^{4+} ion 3 μ_B. Thus, if all of the film is in a ferromagnetic state then there should be an average contribution of (4-x) μ_B per manganese ion. Figure 5.9 shows the ferromagnetic volume fraction (assuming full spin-alignment) as a function of Ca content.

The fully spin-aligned saturation moment was not observed for any of the samples in this study. The saturation moments for the samples with x=0.40 and x=0.41 were 39% and 38% respectively of the value for a fully aligned ferromagnetic film. There are several possible reasons for this reduced magnetic moment.

Firstly, there could be intrinsic phase separation at these compositions in epitaxial thin films. Phase separation has been seen near the low-temperature FM-CO boundary in bulk $La_{0.50}Ca_{0.50}MnO_3$ [20]. This is the most likely explanation given the circumstantial evidence.

Secondly, there is the possibility of a magnetically 'dead' layer within the film close to the film-substrate interface. Such dead layers have been postulated in manganite films from low-temperature conductivity measurements [1,21], or saturation magnetisation values [22] for films of varying thickness. The extent of these dead layers is typically about 4-6 nm for $La_{0.7}Ca_{0.3}MnO_3$ films grown on $SrTiO_3$ [21,22]. While the presence of a dead layer cannot be excluded here, if it were the only factor responsible for the reduction in moment then the dead layer for $La_{0.60}Ca_{0.40}MnO_3$ and $La_{0.59}Ca_{0.41}MnO_3$ would need to be almost 40 nm thick. Such a thick 'dead' layer seems implausible, and is an order of magnitude greater than anything reported to date.

The low temperature state may not be a fully spin aligned ferromagnet, but instead the manganese spins might be canted at an angle. Such a state is inferred in bulk $La_{1-x}Ca_xMnO_3$ below 100-150 K for x<0.1 and x>0.9 [12] and so this is possible in the $La_{1-x}Ca_xMnO_3$ system. Note that Viret *et al.* suggested a spin-canted interfacial

layer [23], which originated from oxygen deficiencies, to explain the reduction in magnetoresistance above 150 K in $SrTiO_3/La_{0.7}Sr_{0.3}MnO_3$ manganite tunnel junctions. The net magnetic moment for a canted antiferromagnet varies as $M_0\cos\theta$, where M_0 is the moment for the fully spin-aligned state (i.e. a classical ferromagnet) and θ is the canting angle as defined in Figure 5.10. The observed moment for x=0.40 is consistent with θ=67º. This high value seems unlikely, so purely a canted spin state is rejected. It should be noted that the three above factors are not mutually exclusive and thus they could all have a contribution towards the reduction in magnetic moment.

Finally, it should be noted that any slight off-stoichiometry in the Mn^{3+}:Mn^{4+} ratio, from either the cation ratio or the oxygenation level, will alter the expected saturation moment and hence the ferromagnetic fraction in the sample. Due to the difficulty of obtaining the exact composition of these films, the effect of off-stoichiometry cannot be excluded.

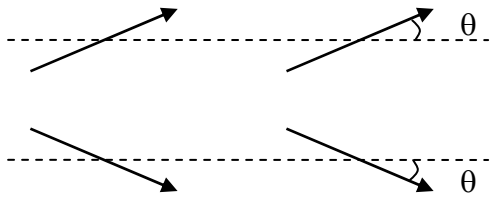

Figure 5.10. Canted manganese spins. A canting angle θ=0º corresponds to a simple ferromagnetic and θ=90º to an antiferromagnet.

The coercive field H_C was 530±10 Oe for x=0.40 and 550±20 Oe for x=0.41 at 20 K, with no significant differences between the forward and reverse directions. This value is greater than the value of 300 Oe at 5 K for $La_{0.7}Ca_{0.3}MnO_3$ films on $SrTiO_3$ (001) [24]. The film is magnetically harder than bulk $La_{0.60}Ca_{0.40}MnO_3$, which has an H_C of roughly 100 Oe at 100 K [25]. Note that the coercive field of a ferromagnet typically decreases with increasing temperature. The shape of the $M(H)$ curves from Figure 5.8 is interesting. The rounded loop (as opposed to a square loop) is typical of a magnetically inhomogeneous material with many pinning sites. This is consistent with the presence of a phase-separated mixture.

The $M(H)$ measurements from this section reinforce the resistivity data from Section 5.4 and suggest that the limit of the ferromagnetic metallic state has been altered from x=0.50 in the bulk material to $x \approx 0.41$ by strain in epitaxial films on $SrTiO_3$ (001). It should be noted that because the type and degree of strain vary according to the substrate, this new limit of metallicity might only be applicable for epitaxial films grown on $SrTiO_3$ (001). In addition, this limit may depend on film thickness.

5.5.2 Magnetisation vs. temperature

The magnetisation of each $La_{1-x}Ca_xMnO_3$ film was also measured as a function of temperature. During the measurements an external magnetic field (H=1000 Oe) was applied to ensure that the sample was single domain. The value of the applied field was chosen to be greater than the coercive field of the sample, yet not so large that there would be a significant diamagnetic contribution from the substrate or any significant increase in the ferromagnetic fraction. $SrTiO_3$ is weakly diamagnetic ($\chi \sim -1\times10^{-6}$) and the contribution to the signal from the substrate was subtracted. All measurements were performed on warming.

Figure 5.11 shows $M(T)$ plots for the series of 60 nm films. The trace for x=0.40 indicates a FM low temperature state, and shows a value at 20 K which agrees to within 1% with the saturation moment from Figure 5.8. The trace for x=0.41 also indicates a low-temperature FM state, but the moment at 20 K was only 60% of the saturation moment from Figure 5.8. The traces for the films with x=0.42, 0.43, 0.44 and 0.45 again show good agreement at 20 K with the values obtained from $M(H)$ measurements. There is no appreciable moment for these four samples and there is little temperature dependence. The Curie temperature, if any, was taken to be the inflection point in the $M(T)$ traces, although this was hard to define accurately. Even for the samples which showed ferromagnetic behaviour at 20 K there was no sudden upturn in M, unlike for bulk samples of $La_{0.60}Ca_{0.40}MnO_3$ [25]. This is further evidence for magnetic inhomogeneity.

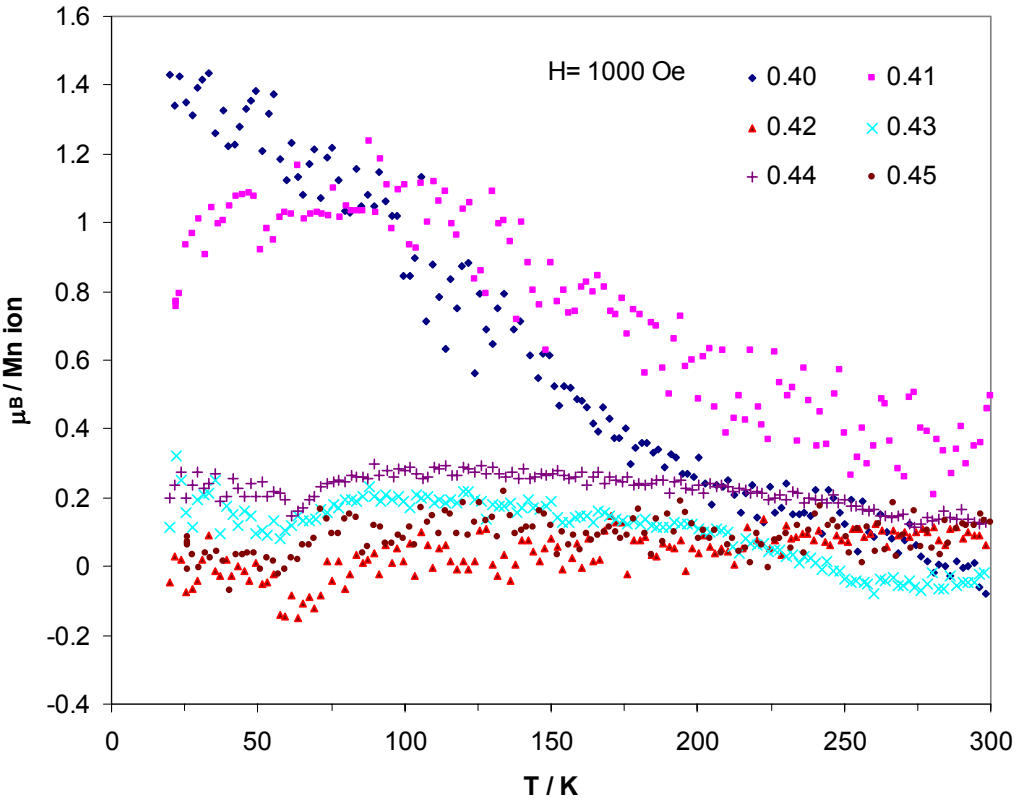

Figure 5.11. Magnetisation vs. temperature for $La_{1-x}Ca_xMnO_3$ films on $SrTiO_3$ (001) in H=1000 Oe. All samples were cooled in zero-field and the data were taken on warming.

Figure 5.12 (overleaf) depicts a slight dependence on the history of the sample for x=0.40 and 0.41. In both cases, the magnetic moment at low temperature was greater when the sample was cooled in a magnetic field of 1000 Oe immediately prior to warming. The increase in moment at low temperature was approximately 25% for $La_{0.60}Ca_{0.40}MnO_3$ and 50% for $La_{0.59}Ca_{0.41}MnO_3$. When the sample was cooled with no external magnetic (ZFC) then when the measuring field is applied at 20 K, the manganese spins are not able to align fully due to having insufficient thermal energy at low temperature. As the temperature is raised, the thermal energy increases and there is better spin alignment. If the sample were cooled in an applied field (FC) then the spins would start to align as the temperature reached T_C and would be aligned better prior to the warming sweep. This type of low-temperature field-history dependent behaviour is typical of a spin glass. Similar dependence on the cooling field was seen by Wu *et al.* for $La_{0.40}Pr_{0.27}Ca_{0.33}MnO_3$ [4].

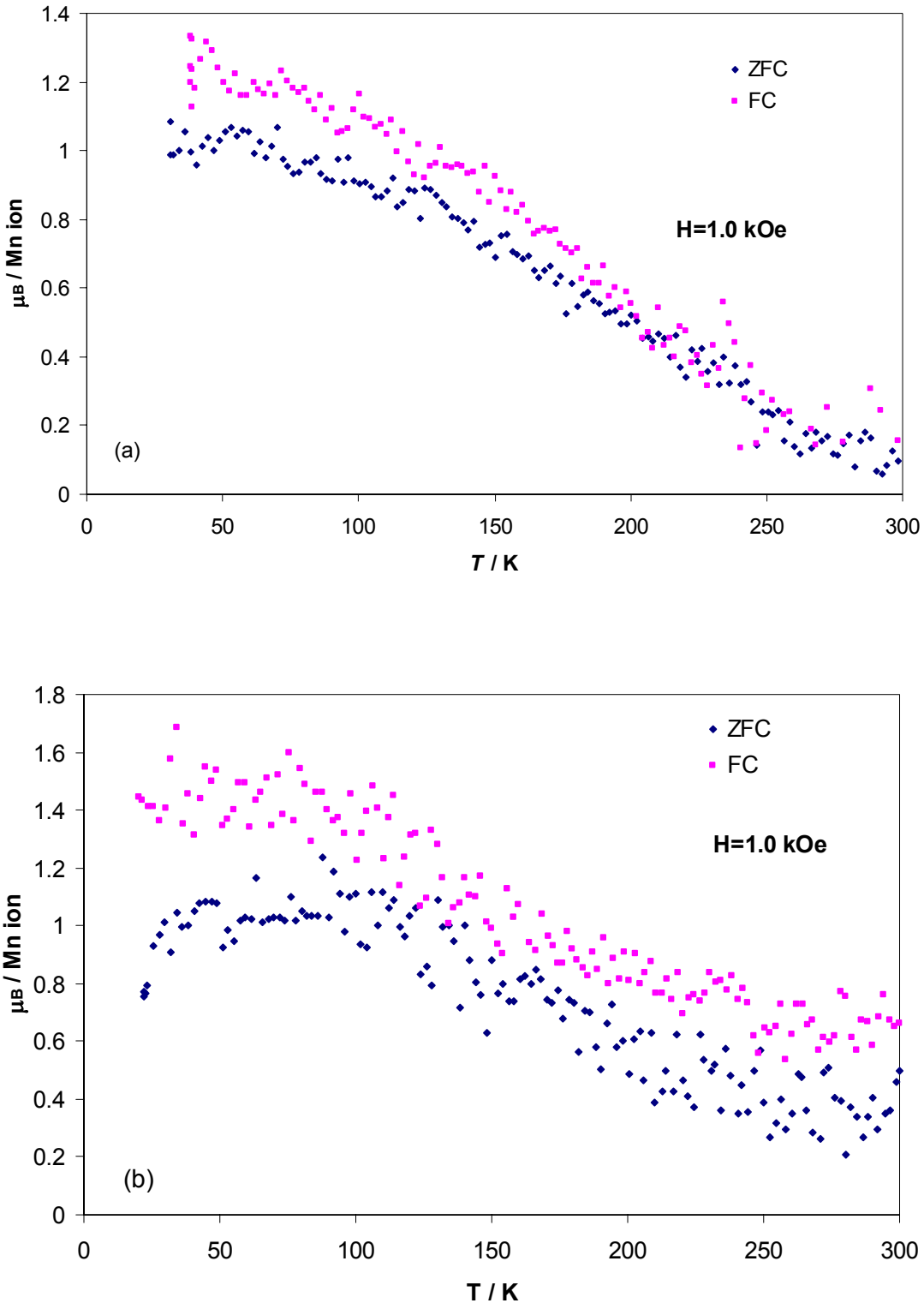

Figure 5.12. Magnetisation vs. temperature for (a) a 59 nm $La_{0.60}Ca_{0.40}MnO_3$ film and (b) a 60 nm $La_{0.59}Ca_{0.41}MnO_3$ film grown on $SrTiO_3$ (001). For each plot the two curves correspond to zero field cooling (ZFC) and field cooling in H=1.0 kOe (FC). In all cases data were taken on warming with H=1.0 kOe

Spin glass behaviour has been seen at low temperatures in many manganite systems [26,27]. Spin glasses are disordered and frustrated magnetic systems with a characteristic freezing temperature T_f. The frustration arises from the competition between ferromagnetic and antiferromagnetic interactions [28]. Below T_f, the spins form clusters in a metastable frozen state without the usual degree of long-range magnetic order. The dynamics of a typical spin glass are slow and aging effects are commonly seen [27,29,30]. Recent studies have suggested that the glassy behaviour of the phase-segregated state can be understood purely from intercluster interactions (as opposed to interactions between individual spins) [31], and cannot be considered as a conventional spin glass, although the low temperature behaviour has many similarities with classical spin glasses. Relaxation effects when the magnetic field is changed will be discussed further in Chapter 7.

5.6 A phase diagram for $La_{1-x}Ca_xMnO_3$ films on $SrTiO_3$ (001)

By combining the transition temperatures and ground states obtained from the electrical transport and magnetisation data above, it is possible to construct a simple phase diagram for nominally 60 nm thick $La_{1-x}Ca_xMnO_3$ films deposited on $SrTiO_3$ (001) in the region $0.40<x<0.45$. Figure 5.13 shows this new phase diagram with an approximate boundary between the phases. Note that the metal or insulator designation refers to transport through the film as a whole.

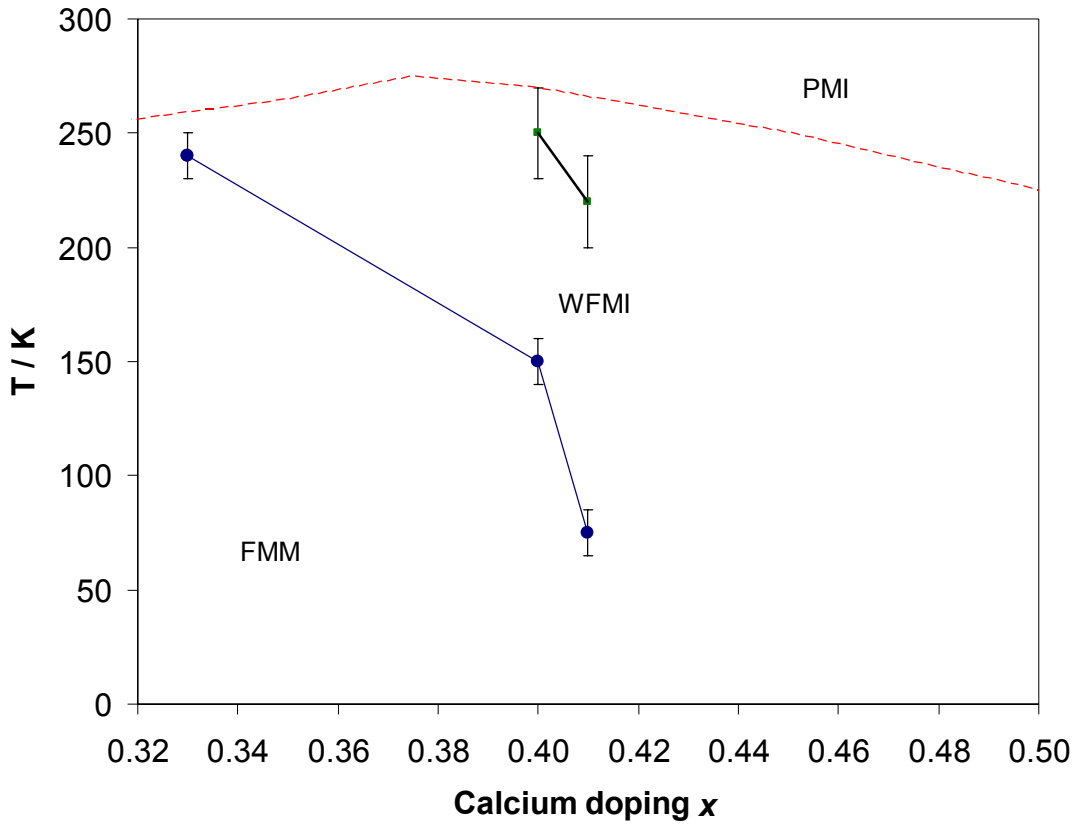

Figure 5.13. The phase diagram for nominally 60 nm $La_{1-x}Ca_xMnO_3$ films on $SrTiO_3$ (001). The transition temperatures are taken from the peak in resistivity (●) and the point of inflection in magnetisation (■) data. No metal-insulator transition was seen for $x>0.41$. The dotted line corresponds to the ferromagnetic metal–paramagnetic insulator phase boundary for bulk $La_{1-x}Ca_xMnO_3$ taken from [12]. The data point for a $La_{0.67}Ca_{0.33}MnO_3$ film is taken from [18]. The labels refer to a ferromagnetic metal (FMM), weakly ferromagnetic insulator (WFMI) and paramagnetic insulator (PMI).

It should be noted that, while the samples with $x>0.41$ remained insulating at all temperatures, and there was a weak ferromagnetic signal at 20 K, it was not possible to assign a Curie temperature to these samples due to the small ferromagnetic signal and high noise level. The extent of the weakly ferromagnetic insulating region shown in Figure 5.13 is therefore slightly uncertain.

There is coexistence for $T_{MI}<T<T_C$ at $x=0.40$ and $x=0.41$, in which there is ferromagnetism in the sample, but the overall electrical transport behaviour is insulating. A possible explanation is a phase-separated mixture of ferromagnetic clusters in a non-ferromagnetic matrix. The limiting composition for metallic behaviour at 20 K is at $x=0.41$ within the resolution of this study, and the saturation moment is reduced to 38±1% of the fully spin-aligned theoretical value. However, some degree of ferromagnetism persisted up to $x=0.45$. This reduced moment suggests that there is a phase-separated mixture for these compositions. The in-plane tensile strain induced in the film by the $SrTiO_3$ substrate has altered the relative stabilities of the ferromagnetic and non-ferromagnetic phases and altered the position and nature of the phase boundary.

The transition temperatures obtained from the resistivity and magnetic measurements do not agree well for either $La_{0.60}Ca_{0.40}MnO_3$ or $La_{0.59}Ca_{0.41}MnO_3$. For both cases, T_C was greater than T_{MI}. The most likely explanation for this is that there is a range of local Curie temperatures where parts of the film become ferromagnetic below T_1 but the film only becomes conducting below T_2 ($<T_1$) when further parts of the film enter the FMM state. Note that, because the two transition temperatures are obtained from different measurement techniques, slight variations in the transition temperature are not unexpected. This is particularly relevant for broad transitions, such as the magnetic transition as seen here.

A possible explanation of the ferromagnetic insulating behaviour in the films is as follows. There is a phase-separated mixture of FMM clusters in an insulating matrix. Conduction occurs by percolation between the clusters, but only if there is a critical volume fraction of FMM clusters to allow percolation throughout the sample. Measurements by Kim *et al.* [32] reveal a percolation threshold of 17% FMM material for $La_{5/8-x}Pr_xCa_{3/8}MnO_3$, and it seems reasonable to assume a similar value

for these $La_{1-x}Ca_xMnO_3$ films. There may be an additional dependence on the quality of the film surface, in that the smoother films tend to have greater saturation moments.

5.7 $La_{1-x}Ca_xMnO_3$ films on $NdGaO_3$ (001)

The preceding three sections have concentrated on characterising the $La_{1-x}Ca_xMnO_3$ films grown on $SrTiO_3$ (001). A similar study was made on the transport and magnetic properties of the set of films on $NdGaO_3$ (001) and the results are presented here for comparison. Zero field resistivity data along the film [100] direction for this set of films is presented in Figure 5.14.

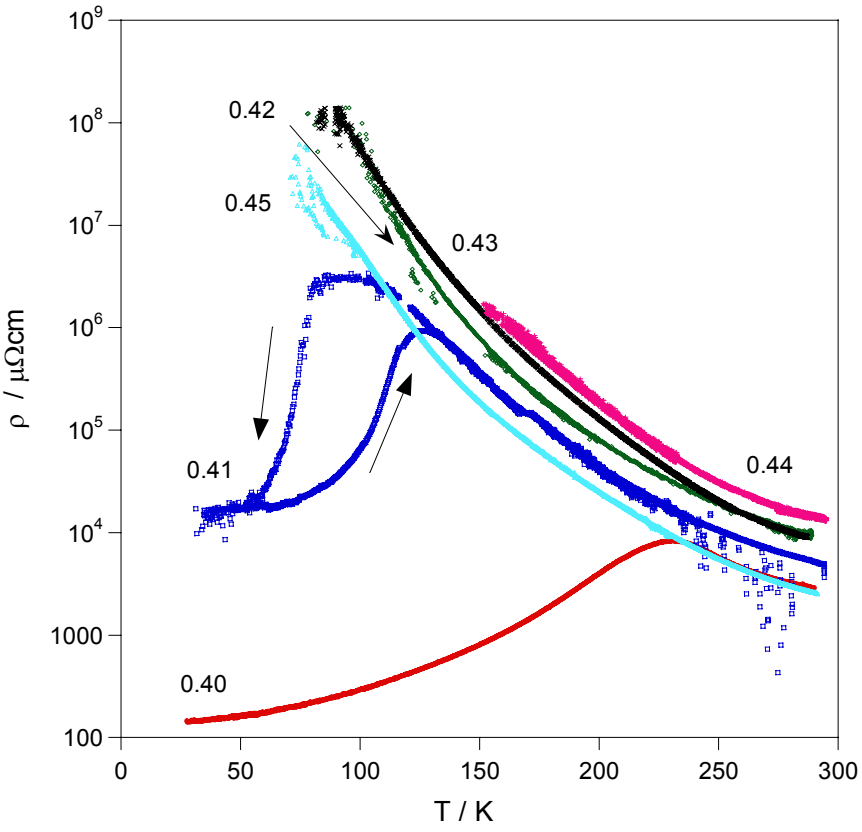

Figure 5.14. Zero field resistivity vs. temperature for nominally 60 nm $La_{1-x}Ca_xMnO_3$ films on $NdGaO_3$ (001).

Two things are immediately obvious from Figure 5.14. Firstly, only the x=0.40 and x=0.41 films showed metallic behaviour at low temperatures while the films with x>0.41 remained insulating down to the limit of the measurement. This is the same limit of metallic behaviour as for the films on $SrTiO_3$ (001). Secondly, the peak in

resistivity for these two curves occurred at 230 K for $La_{0.60}Ca_{0.40}MnO_3$ and at 90 K on cooling and 125 K on warming for the $La_{0.59}Ca_{0.41}MnO_3$ film. These temperatures are higher than for the corresponding film on $SrTiO_3$. The most likely explanation for this is that the strain state for films on $NdGaO_3$ is different, with a uniaxial tensile strain of 0.1%, and the material consequently behaves much more like bulk polycrystalline $La_{1-x}Ca_xMnO_3$. Both the room temperature resistivity values and the residual resistivity for the $La_{0.60}Ca_{0.40}MnO_3$ film are 1-2 orders of magnitude smaller for the films on $NdGaO_3$. The room-temperature resistivity values seen in Figure 5.14 show the same trend as for the films on $SrTiO_3$ (001), in that the room-temperature value increases as the Ca content varies from 40% to 44%, whereas the room-temperature resistivity for the $La_{0.55}Ca_{0.45}MnO_3$ film is comparable with the $La_{0.60}Ca_{0.40}MnO_3$ sample. Again, the reason for this anomaly is unclear.

The magnetic data for this set of films on $NdGaO_3$ is less complete than for the films on $SrTiO_3$. Due to the large value of the angular momentum quantum number (J=9/2), the Nd^{3+} ions have a large paramagnetic moment. Consequently, it was difficult to resolve the magnetic contribution from the film from that of the substrate.

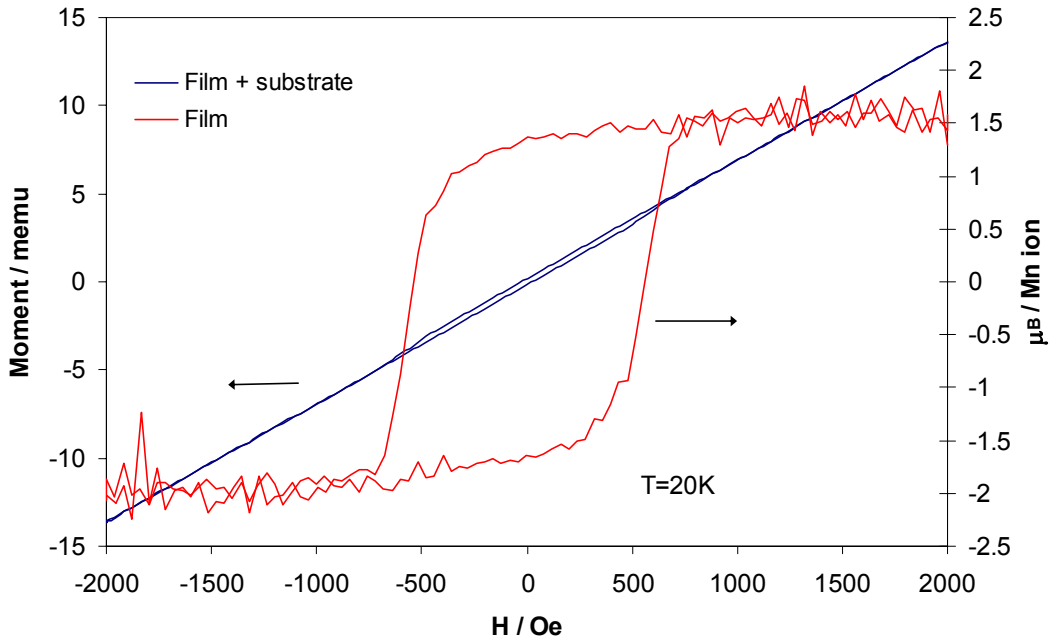

Figure 5.15. M(H) at 20 K for a $La_{0.60}Ca_{0.40}MnO_3$ film on $NdGaO_3$ (001) after correcting for the paramagnetic background. The raw data is shown for comparison.

This is particularly true at low temperatures. For example, at 20 K, the signal from the film is three orders of magnitude smaller than the substrate signal. Figure 5.15 shows a $M(H)$ sweep at 20 K for a $La_{0.60}Ca_{0.40}MnO_3$ film on $NdGaO_3$ (001). The raw data, in which the hysteresis loop can just be seen, is shown in addition for comparison. Note that Figure 5.15 shows data for a metallic sample that had a saturation moment of 1.8 μ_B per Mn ion. The magnetic signal for the insulating films, which was predicted to be 5-10 times smaller, was impossible to resolve from the paramagnetic background.

From the transport data in Figure 5.14 and preliminary magnetic data, it was possible to produce a preliminary phase diagram for nominally 60 nm $La_{1-x}Ca_xMnO_3$ films deposited on $NdGaO_3$ (001). This phase diagram is shown in Figure 5.16. The labels refer to a ferromagnetic metal (FMM), weakly ferromagnetic insulator (WFMI) and paramagnetic insulator (PMI) respectively.

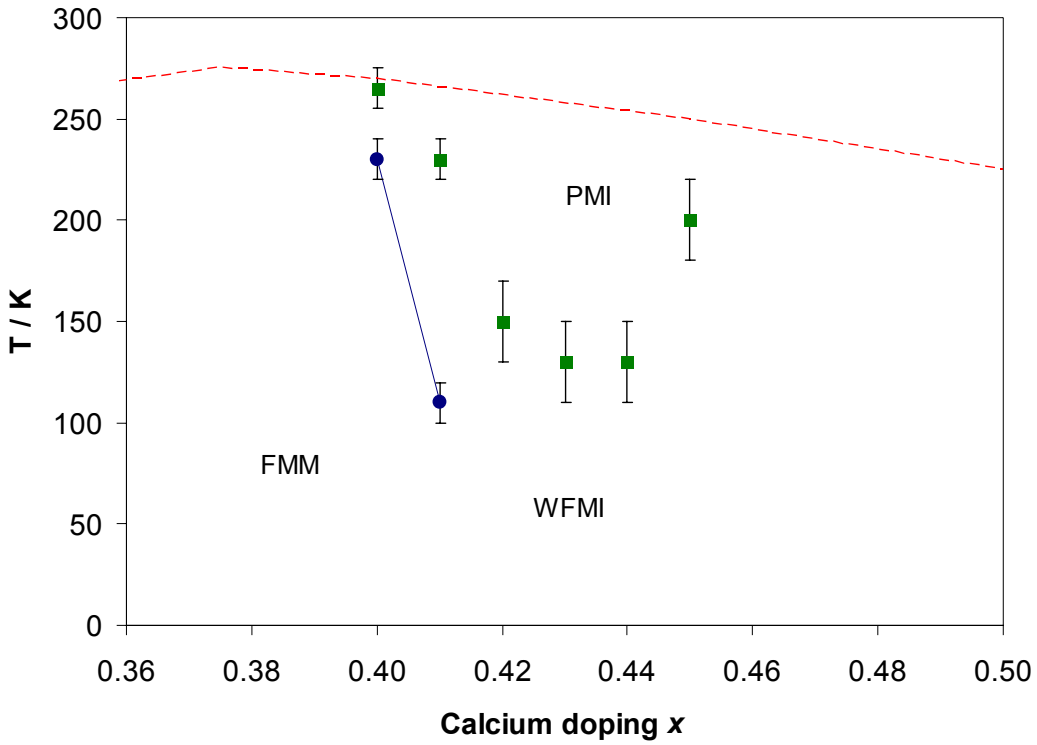

Figure 5.16. A preliminary phase diagram for nominally 60 nm films of $La_{1-x}Ca_xMnO_3$ deposited on $NdGaO_3$ (001). The data points correspond to transport (●) and magnetic (■) transitions respectively. The dotted line corresponds to the ferromagnetic metal–paramagnetic insulator phase boundary for bulk $La_{1-x}Ca_xMnO_3$ and is taken from [12].

5.8 Summary

It has been shown in this chapter that the behaviour of thin films is very different from the bulk polycrystalline material. The magnetic and electronic transitions are suppressed compared with the polycrystalline material. Furthermore, the magnetic and electronic transitions occur at different temperatures. The limit of ferromagnetism and metallic behaviour, which in effect coincide at x=0.50 for polycrystalline material, are now split. Instead of a vertical phase boundary on a T vs. x plot at x=0.50, there is an oblique boundary near x=0.4. The limit of low-temperature metallic behaviour is now at x=0.41 for nominally 60 nm films on both $SrTiO_3$ (001) and $NdGaO_3$ (001).

References for Chapter 5

[1] J.Z. Sun, D.W. Abraham, R.A. Rao and C.B. Eom, *Thickness-dependent magnetotransport in ultrathin manganite films.* Appl. Phys. Lett. **74**, 3017-9 (1999).

[2] Y. Suzuki, H.Y. Hwang, S.-W. Cheong, T. Siegrist, R.B. van Dover, A. Asamitsu and Y. Tokura, *Magnetic anisotropy of doped manganite thin films and crystals.* J. Appl. Phys. **83**, 7064-6 (1998).

[3] N.D. Mathur, M.-H. Jo, J.E. Evetts and M.G. Blamire, *Magnetic anisotropy of thin film $La_{0.7}Ca_{0.3}MnO_3$ on untwinned paramagnetic $NdGaO_3$ (001).* J. Appl. Phys. **89**, 3388-92 (2001).

[4] T. Wu, S.B. Ogale, S.R. Shinde, A. Biswas, T. Polletto, R.L. Greene, T. Venkatesan and A.J. Millis, *Substrate induced strain effects in epitaxial $La_{0.67-x}Pr_xCa_{0.33}MnO_3$ thin films.* J. Appl. Phys. **93**, 5507-13 (2003).

[5] E.B. Nyeanchi, I.P. Krylov, X.-M. Zhu and N. Jacobs, *Ferromagnetic ground state in $La_{0.5}Ca_{0.5}MnO_3$ thin films.* Europhys. Lett. **48**, 228-32 (1999).

[6] Z.Q. Li, E.Y. Jiang, S.W. Ren, D.L. Hou, P. Wu and H.L. Bai, *Magneto-transport properties and electronic structure of $La_{0.85}Na_{0.15}MnO_3$.* Phys. Status Solidi A **195**, 429-33 (2003).

[7] D. Rubi, S. Duhalde, M.C. Terzzoli, G. Leyva, G. Polla, P. Levy, F. Parisi and R.R. Urbano, *Structural and electrical characterisation of $La_{0.5}Ca_{0.5}MnO_3$ thin films grown by pulsed laser deposition.* Physica B **320**, 86-9 (2002).

[8] P.K. Siwach, D.P. Singh, H.K. Singh, N. Khare, A.K. Singh and O.N. Srivastava, *Effect of substrate on magneto-transport properties of polycrystalline manganite films.* J. Phys. D: Appl. Phys. **36**, 1361-5 (2003).

[9] W. Prellier, M. Rajeswari, T. Venkatesan and R.L. Greene, *Effects of annealing and strain on $La_{1-x}Ca_xMnO_3$ thin films: A phase diagram in the ferromagnetic region.* Appl. Phys. Lett. **75**, 1446-8 (1999).

[10] M. Roy, J.F. Mitchell, S.J. Potashnik and P. Schiffer, *Field dependent specific heat of rare-earth manganites.* J. Magn. Magn. Mater. **218**, 191-7 (2000).

[11] P. Levy, F. Parisi, G. Polla, D. Vega, G. Leyva, H. Lanza, R.S. Freitas and L. Ghivelder, *Controlled phase separation in $La_{0.5}Ca_{0.5}MnO_3$.* Phys. Rev. B **62**, 6437-41 (2000).

[12] S.-W. Cheong and H.Y. Hwang, *Colossal magnetoresistance Oxides,* (Ed. Y. Tokura), Gordon & Breach, New York (1997).

[13] J. O'Donnell, M.S. Rzchowski, J.N. Eckstein and I. Bozovic, *Magnetoelastic coupling and magnetic anisotropy in $La_{0.67}Ca_{0.33}MnO_3$ films.* Appl. Phys. Lett. **72**, 1775-7 (1998).

[14] R.A. Rao, D. Lavric, T.K. Nath, C.B. Eom, L. Wu and F. Tsui, *Effects of film thickness and lattice mismatch on strain states and magnetic properties of* $La_{0.8}Ca_{0.2}MnO_3$. J. Appl. Phys. **85**, 4794-6 (1999).

[15] C. Kittel, *Introduction to Solid State Physics*, Wiley, New York. p. 160 (1996).

[16] S.M. Sze, *Semiconductor Devices, Physics and Technology*, Wiley, New York. p. 1 (1985).

[17] E.R. Rumbo, *Transport properties of very pure copper and silver below 8.5 K.* J. Phys. F: Met. Phys. **6**, 85-98 (1976).

[18] M. Bibes, M.-J. Casanove, Ll. Balcells, S. Valencia, B. Martínez, J.-C. Ousset and J. Fontcuberta, *Magnetotransport properties of fully strained epitaxial thin films of* $La_{2/3}Ca_{1/3}MnO_3$ *grown on* $SrTiO_3$. Appl. Surf. Sci. **188**, 202-8 (2002).

[19] G.H. Jonker and J.H. van Santen, *Ferromagnetic compounds of manganese with perovskite structure.* Physica **16**, 337-49 (1950).

[20] For a review of phase separation see Chapter 3 and references within,

[21] M. Bibes, Ll. Balcells, S. Valencia, S. Sena, B. Martínez, J. Fontcuberta, S. Nadolski, M. Wojcik and E. Jedryka, *Thickness dependence of surface roughness and transport properties of* $La_{2/3}Ca_{1/3}MnO_3$ *epitaxial thin films.* J. Appl. Phys. **89**, 6686-8 (2001).

[22] M. Ziese, H.C. Semmelhack, K.H. Han, S.P. Sena and H.J. Blythe, *Thickness dependent magnetic and magnetotransport properties of strain-relaxed* $La_{0.7}Ca_{0.3}MnO_3$ *films.* J. Appl. Phys. **91**, 9930-6 (2002).

[23] M. Viret, M. Drouet, J. Nassar, J.P. Contour, C. Fermon and A. Fert, *Low-field colossal magnetoresistance in manganite tunnel spin valves.* Europhys. Lett. **39**, 545-9 (1997).

[24] G. Campillo, A. Berger, J. Osorio, J.E. Pearson, S.D. Bader, E. Baca and P. Prieto, *Substrate dependence of magnetic properties of* $La_{0.67}Ca_{0.33}MnO_3$ *films.* J. Magn. Magn. Mater. **237**, 61-8 (2001).

[25] X. Bohigas, J. Tejada, M.L. Marínez-Sarrión, S. Tripp and R. Black, *Magnetic and calorimetric measurements on the magnetocaloric effect in* $La_{0.6}Ca_{0.4}MnO_3$. J. Magn. Magn. Mater. **208**, 85-92 (2000).

[26] R.S. Freitas, L. Ghivelder, F. Damay, F. Dias and L.F. Cohen, *Magnetic relaxation phenomena and cluster glass properties of* $La_{0.7-x}Y_xCa_{0.3}MnO_3$ *manganites.* Phys. Rev. B **64**, 144404 (2001).

[27] P. Levy, F. Parisi, L. Granja, E. Indelicato and G. Polla, *Novel Dynamical Effects and Persistent Memory in Phase Separated Manganites.* Phys. Rev. Lett. **89**, 137001 (2002).

[28] J.A. Mydosh, *Spin glasses: An experimental introduction*, Taylor & Francis, London (1993).

[29] N. Kozlova, K. Dörr, D. Eckert, A. Handstein, Y. Skourski, T. Walter, K.-H. Müller and L. Schultz, *Slow relaxation of grain boundary resistance in a ferromagnetic manganite.* J. Appl. Phys. **93**, 8325-7 (2003).

[30] M. Sirena, L.B. Steren and J. Guimpel, *Magnetic relaxation in bulk and film manganite compounds.* Phys. Rev. B **64**, 104409 (2001).

[31] F. Rivadulla, M.A. Lópes-Quintela and J. Rivas, *Origin of the Glassy Magnetic Behavior of the Phase Segregated State of the Perovskites.* Phys. Rev. Lett. **93**, 167206 (2004).

[32] K.H. Kim, M. Uehara, C. Hess, P.A. Sharma and S.-W. Cheong, *Thermal and Electronic Transport Properties and Two-Phase Mixtures in* $La_{5/8-x}Pr_xCa_{3/8}MnO_3$. Phys. Rev. Lett. **84**, 2961-4 (2000).

Chapter 6 A field-dependent study of the resistivity

6.1 Introduction

From the work on epitaxial films of $La_{1-x}Ca_xMnO_3$ on $SrTiO_3$ (001) in the previous chapter, it appears likely that there is phase coexistence at low temperatures between a ferromagnetic metallic phase and a non-ferromagnetic insulating phase near x=0.4. The limit of metallic behaviour has been shifted from the bulk value of x=0.50 to x=0.41 for these nominally 60 nm films. The next logical step is to attempt to alter the relative fractions of the competing phases as has been successfully achieved by using external magnetic fields for various manganites [1-3].

6.2 Motivation

The colossal magnetoresistance (CMR) effect seen in bulk manganites requires fields of several tesla e.g. 6 T [4], and originates in the alignment of the Mn core spins. In contrast, the fields required for the low-field MR effect are often 100 mT or lower [5]. The low-field MR effect is thought to arise from aligning magnetic domains, e.g. domain walls [6], or spin polarized tunnelling between layers in tunnel junctions [5]. MR effects at both low and high fields have been seen in polycrystalline $La_{2/3}Sr_{1/3}MnO_3$ [7].

From the $M(H)$ loops in Section 5.5.1 for the $La_{0.60}Ca_{0.40}MnO_3$ and $La_{0.59}Ca_{0.41}MnO_3$ films, it can be seen that the overall coercive field is roughly 53 mT at 20 K, so fields in this range should be adequate to achieve a low-field response, although the effect of fields up to 400 mT will be investigated.

There have been empirical studies that suggest the number of potential carriers in a typical manganite increases in a magnetic field [8]. This is perhaps surprising, as the main effect of a magnetic field in a double exchange ferromagnet will be to align the Mn spins and reduce scattering. There are reports of a magnetic field increasing the ferromagnetic fraction [9], and therefore the number of carriers, although the carrier density in the ferromagnetic regions is unlikely to alter.

6.3 Results vs. temperature

The resistivity of each sample was measured as a function of temperature in magnetic fields up to 400 mT. In all cases the magnetic field was applied in the plane of the film along the [100] direction, i.e. the magnetic field was parallel to the current. There are two quite different effects of the magnetic field depending on whether any metallic behaviour was observed in the zero-field measurement.

6.3.1 $x > 0.41$ – Insulating films

Figures 6.1-6.4 show the resistivity as a function of temperature in zero field and 400 mT for $La_{1-x}Ca_xMnO_3$ films with x=0.42, 0.43, 0.44 and 0.45 respectively. The resistance went above the limit of the measurement apparatus (corresponding to a resistivity of 10^{10} μΩcm) at low temperatures and remained so down to 20 K. There was negligible difference between data taken on cooling and warming for this set of films. For the films with x>0.41, the magnetic field alone was not sufficient to induce metallic behaviour at any temperature.

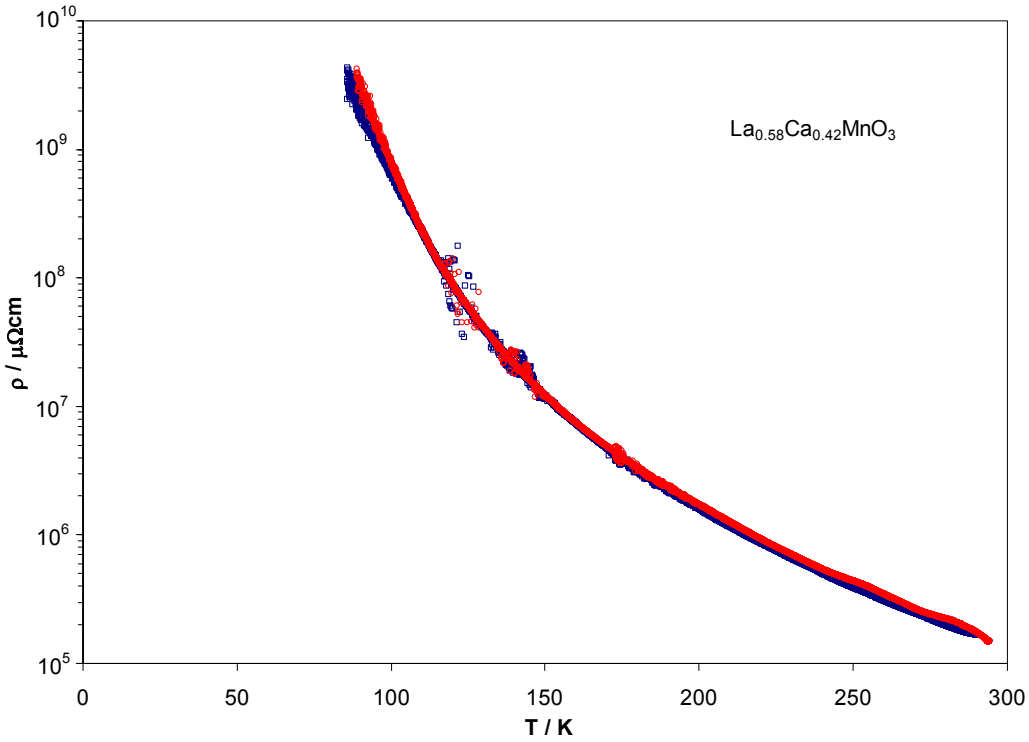

Figure 6.1. Resistivity vs. temperature for a 59 nm $La_{0.58}Ca_{0.42}MnO_3$ film on $SrTiO_3$ (001) in zero field (red) and 400 mT (blue).

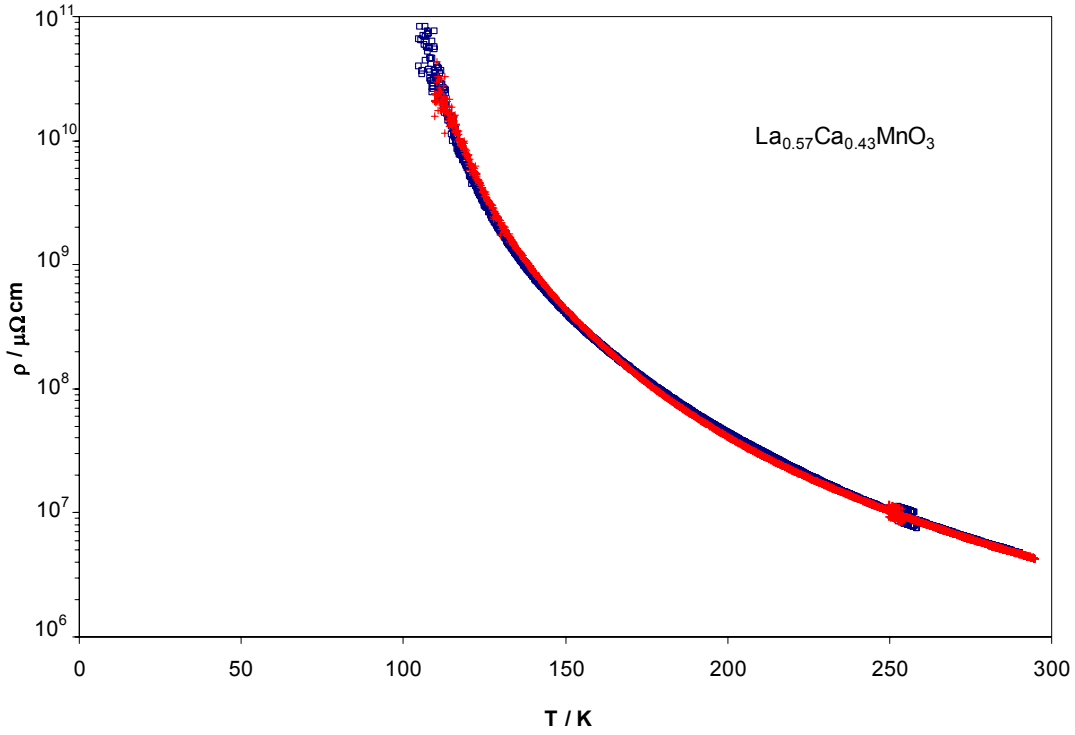

Figure 6.2. Resistivity vs. temperature for a 60 nm $La_{0.57}Ca_{0.43}MnO_3$ film on $SrTiO_3$ (001) in zero field (red) and 400 mT (blue).

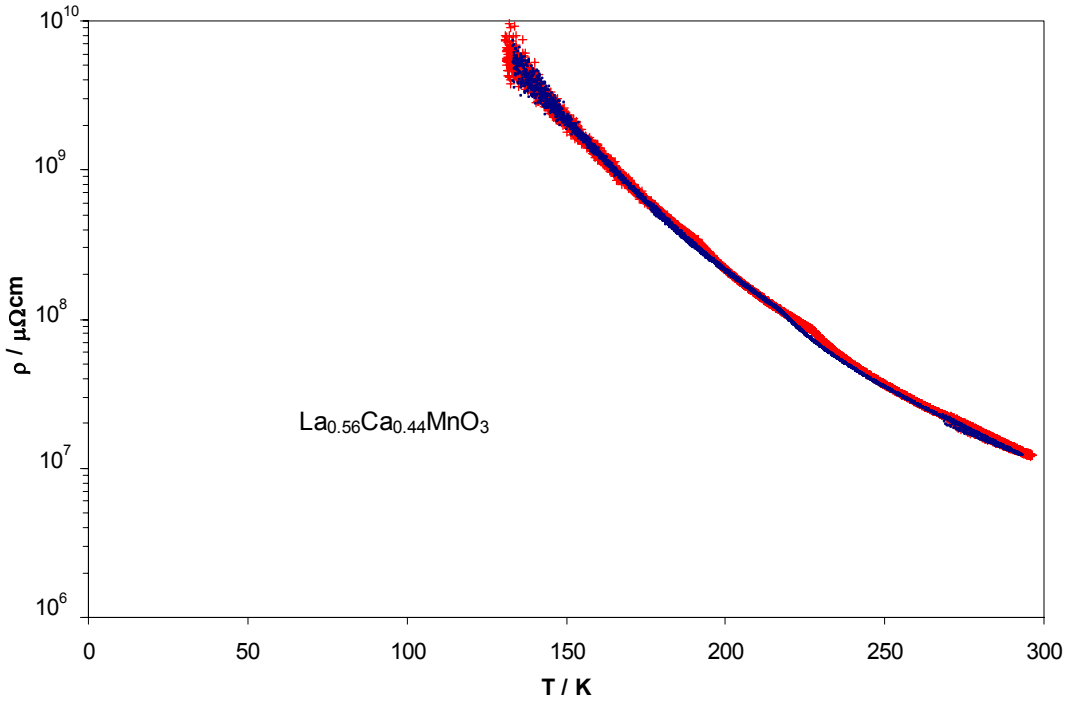

Figure 6.3. Resistivity vs. temperature for a 56 nm $La_{0.56}Ca_{0.44}MnO_3$ film on $SrTiO_3$ (001) in zero field (red) and 400 mT (blue).

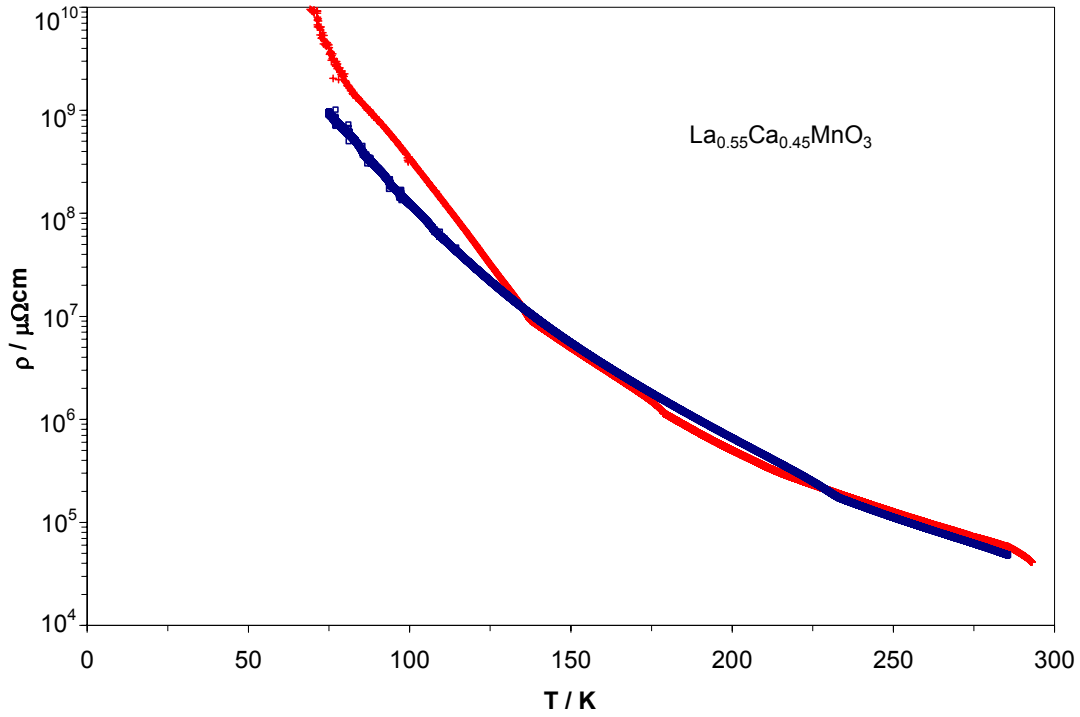

Figure 6.4. Resistivity vs. temperature for a 54 nm $La_{0.55}Ca_{0.45}MnO_3$ film on $SrTiO_3$ (001) in zero field (red) and 400 mT (blue).

As can be seen from Figures 6.1-6.4, a 400 mT field was not able to induce metallic behaviour into the otherwise insulating films. This is consistent with the magnetisation measurements from Section 5.5.1, in which the magnetic moment at 20 K and $\mu_0 H$=200 mT was found to be at best 5% of the fully spin-aligned value. This value is below the calculated 3-D percolation threshold of 14% [10] and the experimentally observed threshold for metallic behaviour of 17% [11]. The behaviour seen here adds further support to a picture where there are only very few locally ferromagnetic regions in the films with x>0.41, and these regions are too sparse to allow percolation on a macroscopic scale. There are reports in the literature of metallic behaviour at high fields in otherwise insulating manganite films, but the fields required to melt the insulating phase are usually several tesla, e.g. 5-9 T for the 'charge-ordered' phase in $Pr_{0.5}Ca_{0.5}MnO_3$ films [12] or 25 T for single crystals of the same material [13].

The MR effect in each case is very small, with a maximum value of about 10%. This is consistent with the bulk ferromagnetic material, where the MR effect is only appreciable close to T_{MI} [4]. Since these samples do not show a metal-insulator

transition either in zero field or in 400 mT, it is unsurprising that the MR is so small. There was little thermal hysteresis for any sample. The traces shown in each figure are for cooling, but the warming traces were coincident within the resolution of the experiment.

6.3.2 $x \leq 0.41$ – Metallic films

The resistivity as a function of temperature and magnetic field was also investigated for the $La_{0.59}Ca_{0.41}MnO_3$ and $La_{0.60}Ca_{0.40}MnO_3$ films. Figure 6.5 shows the resistivity in zero field and with B=300 mT as a function of temperature for the $La_{0.59}Ca_{0.41}MnO_3$ film. As can be seen, the transition temperature, as defined by the resistivity peak, increased slightly from 75 K in zero field to 80 K in 300 mT. Additionally, unlike the insulating samples, there was a significant MR close to the resistivity peak and the MR value decreased away from the metal-insulator transition. The maximum MR value for the $La_{0.59}Ca_{0.41}MnO_3$ film was 50% at 95 K. This is consistent with the bulk ferromagnetic compositions, e.g. x=0.30, where there is only a significant high field MR effect close to the transition temperature.

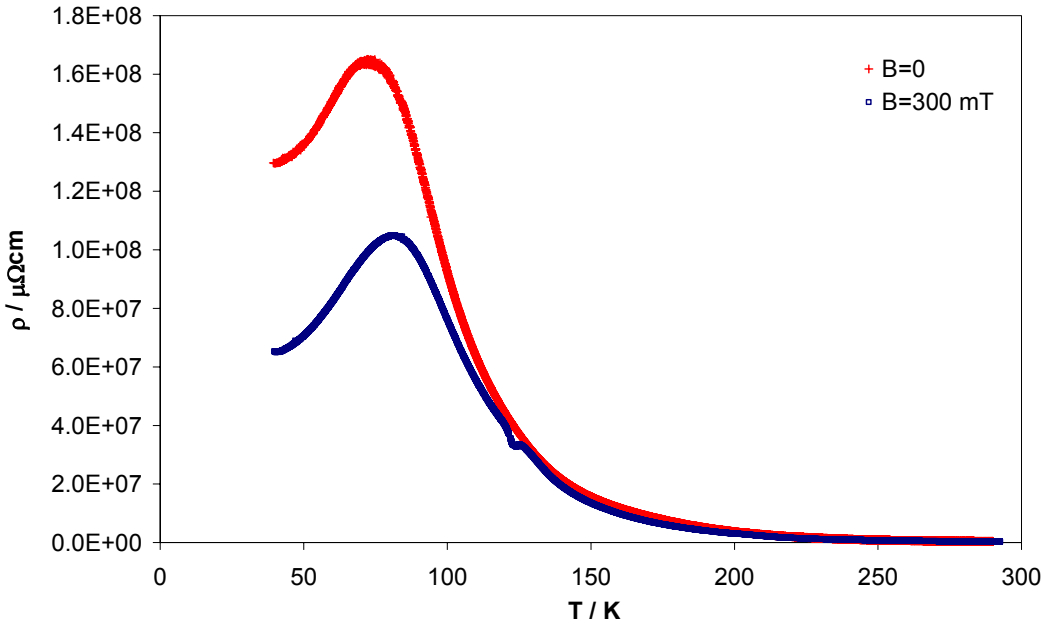

Figure 6.5. Resistivity in zero field (red) and 300 mT (blue) as a function of temperature for a 60 nm $La_{0.59}Ca_{0.41}MnO_3$ film on $SrTiO_3$ (001).

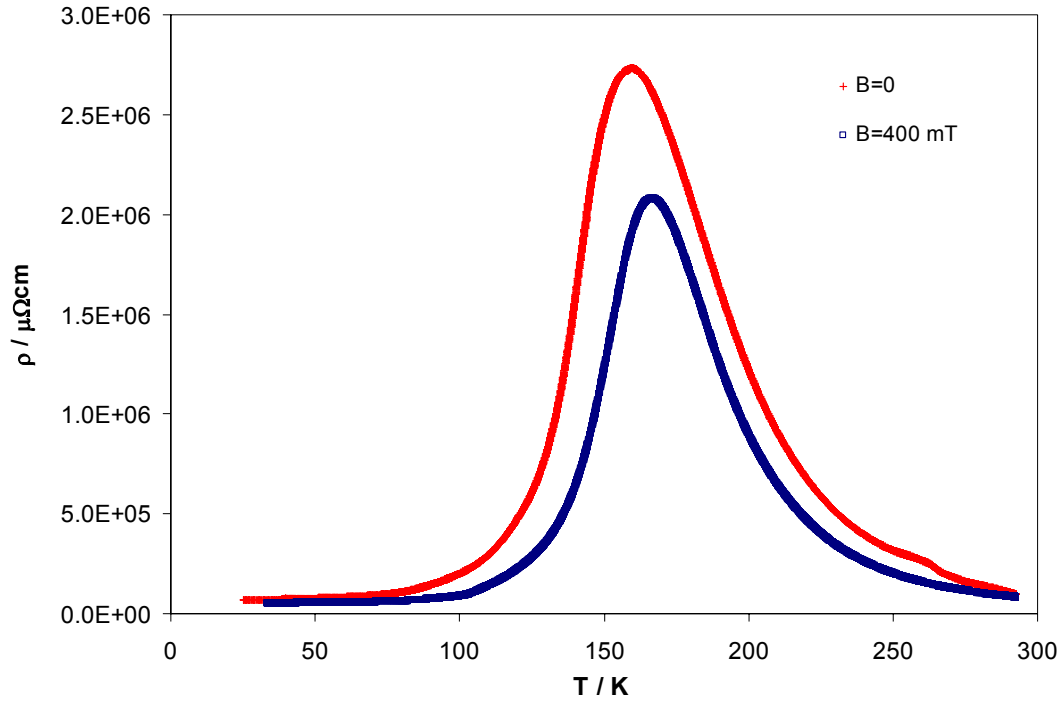

Figure 6.6. Resistivity in zero field (red) and 400 mT (blue) as a function of temperature for a 56 nm $La_{0.60}Ca_{0.40}MnO_3$ film on $SrTiO_3$ (001).

The resistivity as a function of temperature for a $La_{0.60}Ca_{0.40}MnO_3$ film in zero field and 400 mT is shown in Figure 6.6. For this film, the transition temperature increased from 160 K in zero field to 170 K in B=400 mT. As for the $La_{0.59}Ca_{0.41}MnO_3$, there is only a significant MR value close to and just above and below the resistivity peak. The MR at the transition temperature was 30% and the maximum MR was 60% at 140 K.

For the two samples that did show metallic behaviour at low temperature, temperature sweeps were taken through the transition temperature with different magnetic fields. Figure 6.7 shows the resistivity traces for a $La_{0.59}Ca_{0.41}MnO_3$ film in magnetic fields of B=0, 100 mT, 200 mT, 300 mT and 400 mT. The resistivity decreased with increasing magnetic field. This reduction in ρ was most significant close to the resistivity peak and there was comparatively little change above 110 K or below 40 K. The maximum in $\rho(T)$ on cooling showed a slight field dependence, increasing from 75 K for B=0 to 80 K for B=400 mT. Similarly, the resistivity peak on warming increased from 60 K for B=0 to 80 K for B=400 mT.

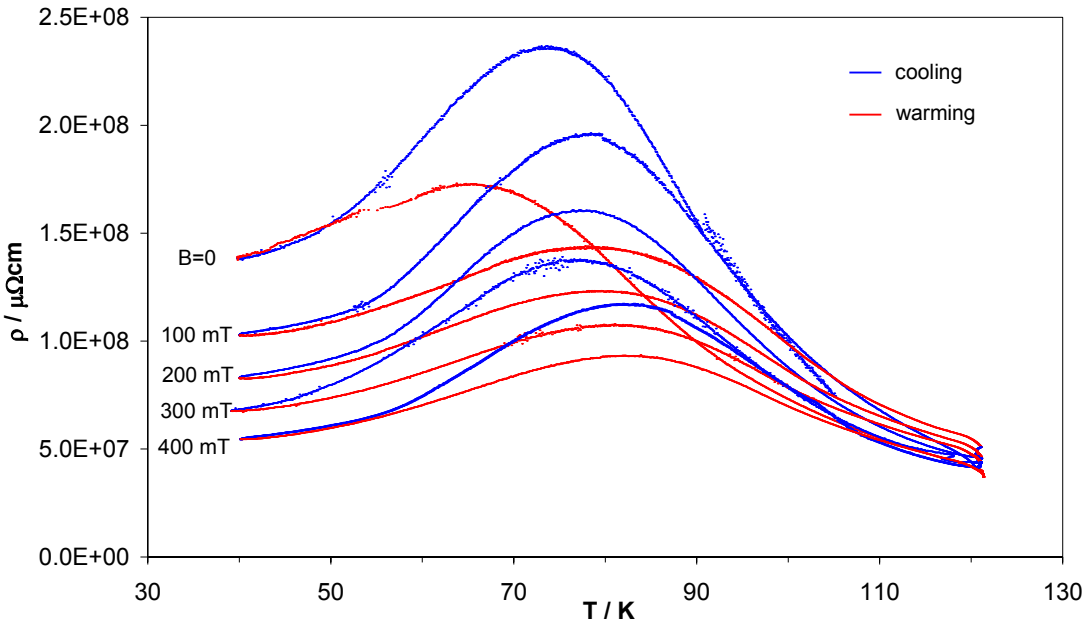

Figure 6.7. Resistivity vs. temperature for a 60 nm $La_{0.59}Ca_{0.41}MnO_3$ film in five different magnetic fields. The traces correspond to cooling (blue) and warming (red) in fields of B=0, 100 mT, 200 mT, 300 mT and 400 mT respectively.

Figure 6.7 shows thermal hysteresis around the transition for all magnetic fields and comparatively little hysteresis well away from the transition. Thermal hysteresis is typical of a first order phase transition. For all values of the applied field, including B=0, the peak resistance on warming was approximately 70% of the peak resistance on cooling in the same field. Figure 6.8 shows the MR values for the $La_{0.59}Ca_{0.41}MnO_3$ film. The MR values at 400 mT were 50% for cooling, and 45% for warming. On both cooling and warming the MR values increased monotonically with the applied field, although the rate of change in MR with field decreased with increasing magnetic field, which indicates that the MR effect was becoming saturated. The ratio of peak resistance on cooling to warming increased linearly from 73% in B=0 to 79% with B=400 mT.

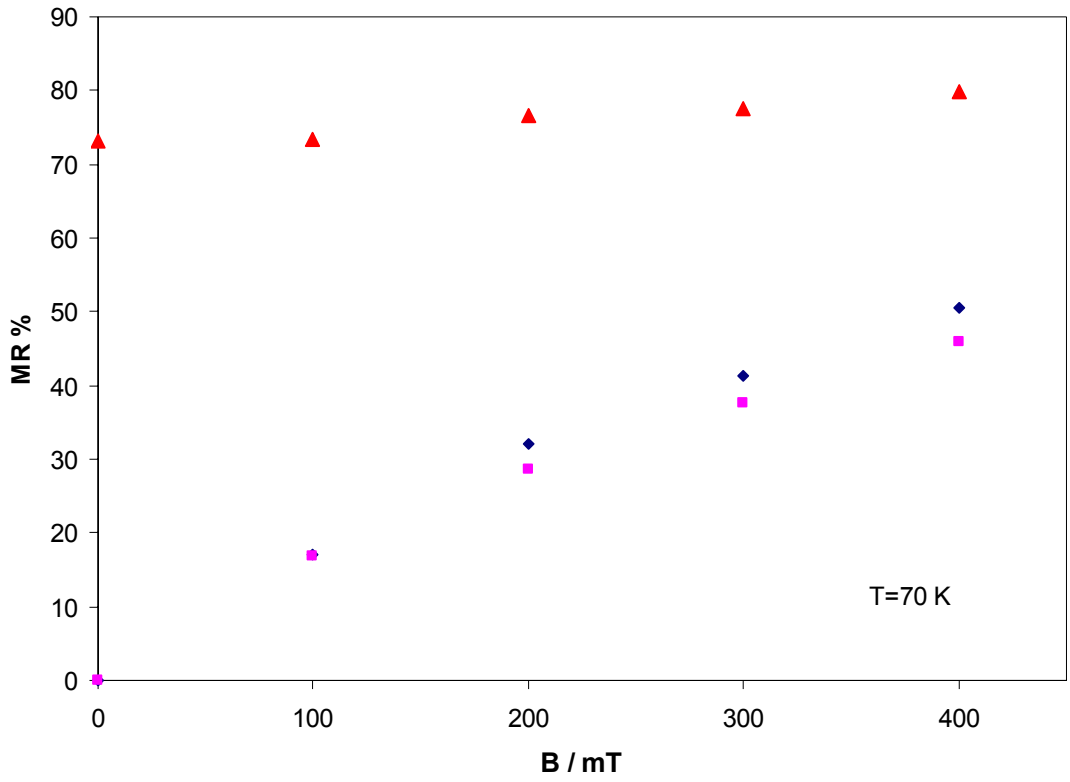

Figure 6.8. Magnetoresistance values at 70 K for a $La_{0.59}Ca_{0.41}MnO_3$ film on $SrTiO_3$ (001) taken from temperature sweeps on cooling (diamonds) and warming (squares). The relative value of the peak resistivity on warming to that on cooling in the same field is also shown (triangles). Error bars are comparable with the size of the points.

Figure 6.9 shows corresponding resistivity data in various magnetic fields for the $La_{0.60}Ca_{0.40}MnO_3$ film. Again, the resistivity decreased with increasing magnetic field. As for the $La_{0.59}Ca_{0.41}MnO_3$ film, there was hysteresis around the resistivity peak, but this time there were also differences in resistivity between the cooling and warming sweeps away from the peak. The reduction in peak resistivity for warming with respect to the corresponding cooling trace was less than 1% and decreased linearly as the magnetic field increases. This difference was much smaller than the difference of 23% in zero field for the $La_{0.59}Ca_{0.41}MnO_3$ film. The resistance peak increased slightly from 165 K in B=0 to 175 K in B=400 mT. Figure 6.10 shows the magnetoresistance values for the $La_{0.60}Ca_{0.40}MnO_3$ film. Again the size of the MR effect increased monotonically with increasing magnetic field. The MR value at 400 mT was 29% on cooling and 29% on warming. For this sample, the MR values for cooling and warming in the same field are the same to better than 1%.

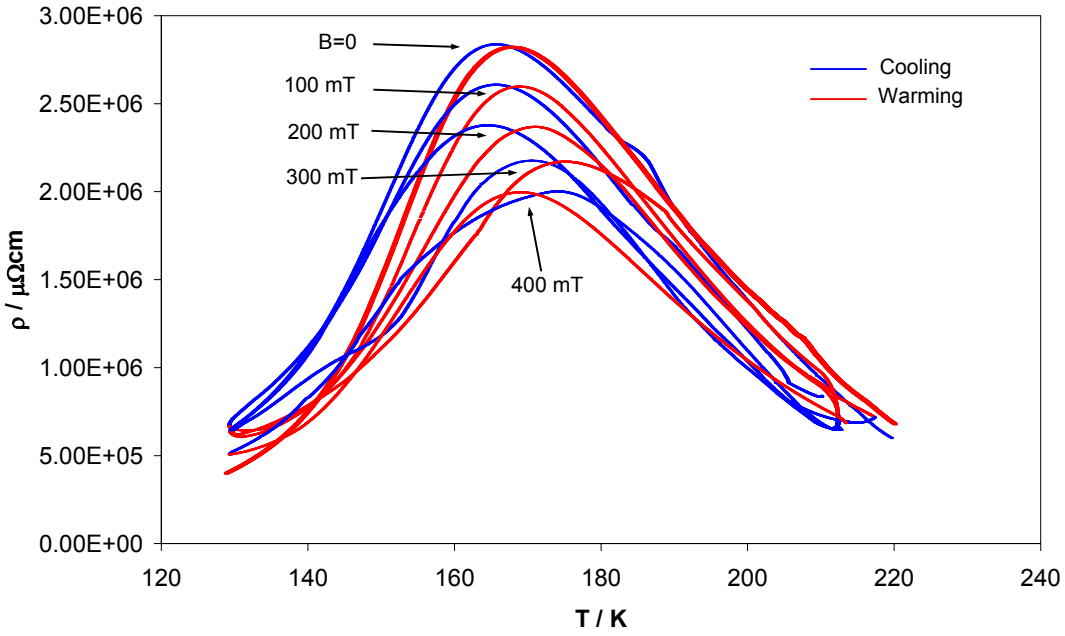

Figure 6.9. Resistivity vs. temperature in various magnetic fields for a 56 nm $La_{0.60}Ca_{0.40}MnO_3$ film on $SrTiO_3$ (001). The traces correspond to cooling (blue) and warming (red) in fields of B=0, 100 mT, 200 mT, 300 mT and 400 mT.

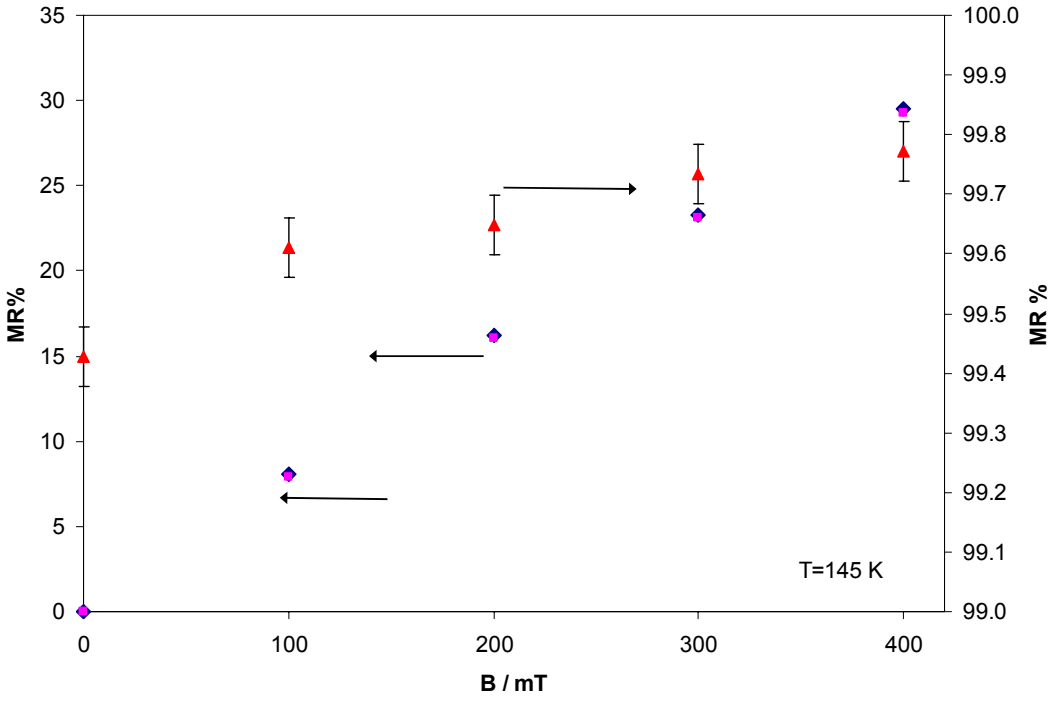

Figure 6.10. Magnetoresistance values as a function of applied field for a $La_{0.60}Ca_{0.40}MnO_3$ film. Symbols correspond to MR values on cooling (diamonds), warming (squares) and between the peak values for cooling and warming in the same field (triangles). Error bars for the cooling and warming series are smaller than the symbols.

From these two measurements, it seems that the behaviour of the $La_{0.60}Ca_{0.40}MnO_3$ and $La_{0.59}Ca_{0.41}MnO_3$ films is qualitatively the same, but the $La_{0.59}Ca_{0.41}MnO_3$ film exhibits greater MR values and larger thermal differences. This is possibly due to the $La_{0.59}Ca_{0.41}MnO_3$ film being closer to the limit of ferromagnetism found in the previous chapter, and as such it is therefore easier to alter the fractions of the competing phases. The change in distribution of these phases will be considered further in Chapter 7. The 5-10 K increase in metal-insulator transition temperature between zero-field measurements and data taken in 400 mT (25 K/T) agrees well with the values of 10 K/T for $La_{0.7}Ca_{0.3}MnO_3$ [1] and 20 K/T for $(La_{0.5}Pr_{0.5})_{0.7}Ca_{0.3}MnO_3$ [2].

6.4 Resistance vs. magnetic field at constant temperature

The resistance of the metallic samples was also measured at constant temperature as a function of magnetic field. Figure 6.11 shows the data for the $La_{0.59}Ca_{0.41}MnO_3$ film at 20 K, 50 K, 70 K and 100 K. Note that the data have been offset vertically for clarity and that T_{MI} for this film is 75 K. At each temperature the magnetic field was swept from B=0→+400 mT → −400 mT →+400 mT →0.

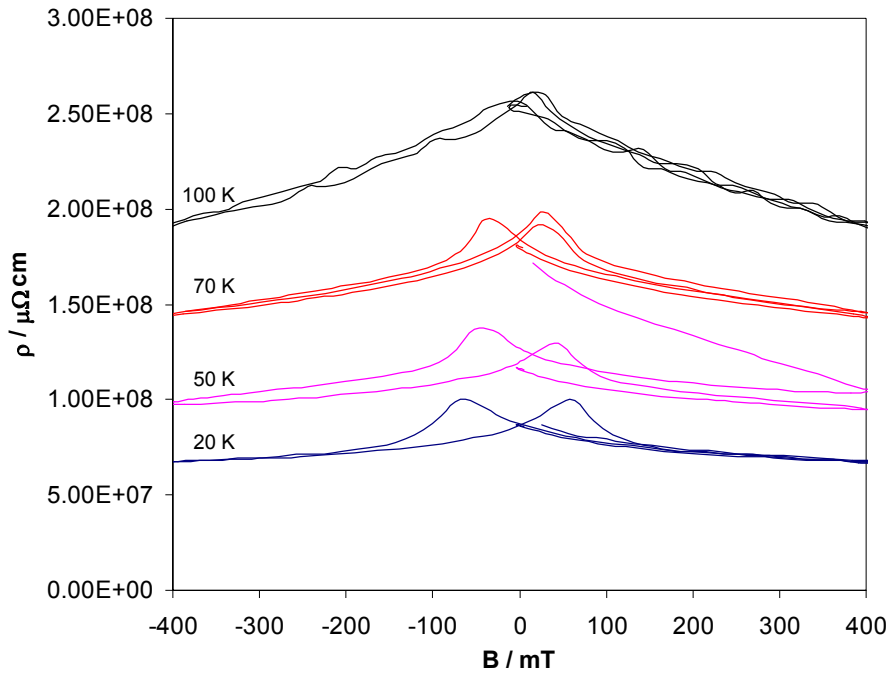

Figure 6.11. Resistivity vs. magnetic field for the $La_{0.59}Ca_{0.41}MnO_3$ film at 20 K, 50 K, 70 K and 100 K. The data for 50 K, 70 K and 100 K have been offset vertically by 10^7 μΩcm for clarity.

The hysteretic butterfly shape seen in Figure 6.11 for T=20 K, 50 K and 70 K is typical of a device with many ferromagnetic components with differing coercive fields. The resistivity depends on the relative orientations of the magnetic moments in the ferromagnetic domains as discussed later and leads to a low-field MR effect. If the LFMR is defined by

$$LFMR(B) = \frac{\rho_{\max}(B) - \rho_{\min}(B)}{\rho_{\max}(B)}, \qquad (6.1)$$

where $\rho_{\max}$ and $\rho_{\min}$ are the maximum and minimum resistivity values for a given field, then the maximum LFMR effect for the $La_{0.59}Ca_{0.41}MnO_3$ film is 20% at B=60 mT and 20 K, 24% at 50 mT and 50 K and 19% at 30 mT and 70 K. At 100 K the LFMR effect was very indistinct.

A high-field MR effect was seen in addition to any LFMR effect at each temperature. Figure 6.12 shows the high-field MR values in 400 mT and the low-field MR values from the previous paragraph as a function of temperature for the $La_{0.59}Ca_{0.41}MnO_3$ film. As expected the maximum high-field MR value was close to

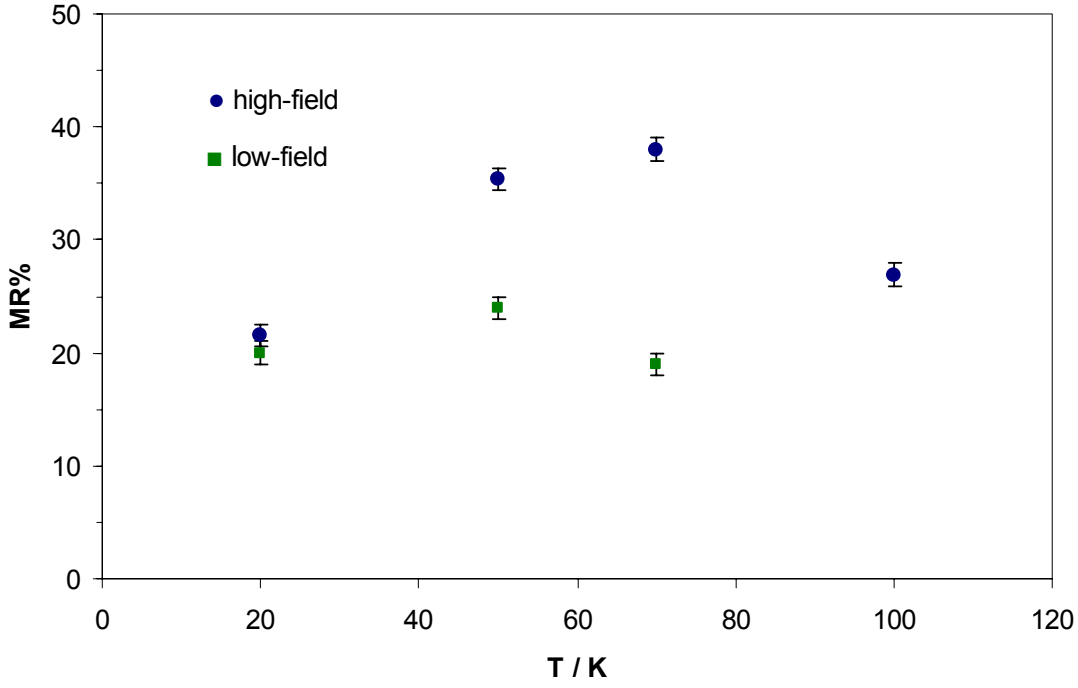

Figure 6.12. Magnetoresistance vs. temperature for a 60 nm $La_{0.59}Ca_{0.41}MnO_3$ film on $SrTiO_3$ (001).

the metal-insulator transition temperature (75 K). Although the size of the high-field MR effect was larger than the LFMR values, the high-field effect requires much larger magnetic fields for the same relative change in resistance. Consequently, the LFMR effect is more likely to be the basis of any future applications.

Figure 6.13 shows corresponding data for the $La_{0.60}Ca_{0.40}MnO_3$ film at various temperatures. Note that T_{MI} for this film was 160 K. Again there was only a LFMR effect below T_{MI}. However, the low-field peaks were hard to resolve and the size of the LFMR effect was an order of magnitude smaller than for the $La_{0.59}Ca_{0.41}MnO_3$ film. No LFMR effect was resolvable for the data at 170 K or 200 K. Figure 6.14 shows the low-field MR values and the high-field MR values in 400 mT. As for the $La_{0.59}Ca_{0.41}MnO_3$ film, the high-field MR effect was greatest close to the metal-insulator transition and the size of the high-field MR effect was greater than the size of the LFMR effect, although the ratio of the high-field to low-field effects was greater for the $La_{0.60}Ca_{0.40}MnO_3$ film. Additionally, the data for $La_{0.60}Ca_{0.40}MnO_3$ at 100 K has peaks at ±17 mT and ±40 mT. A second resistivity peak was not observed at any other temperature for either film.

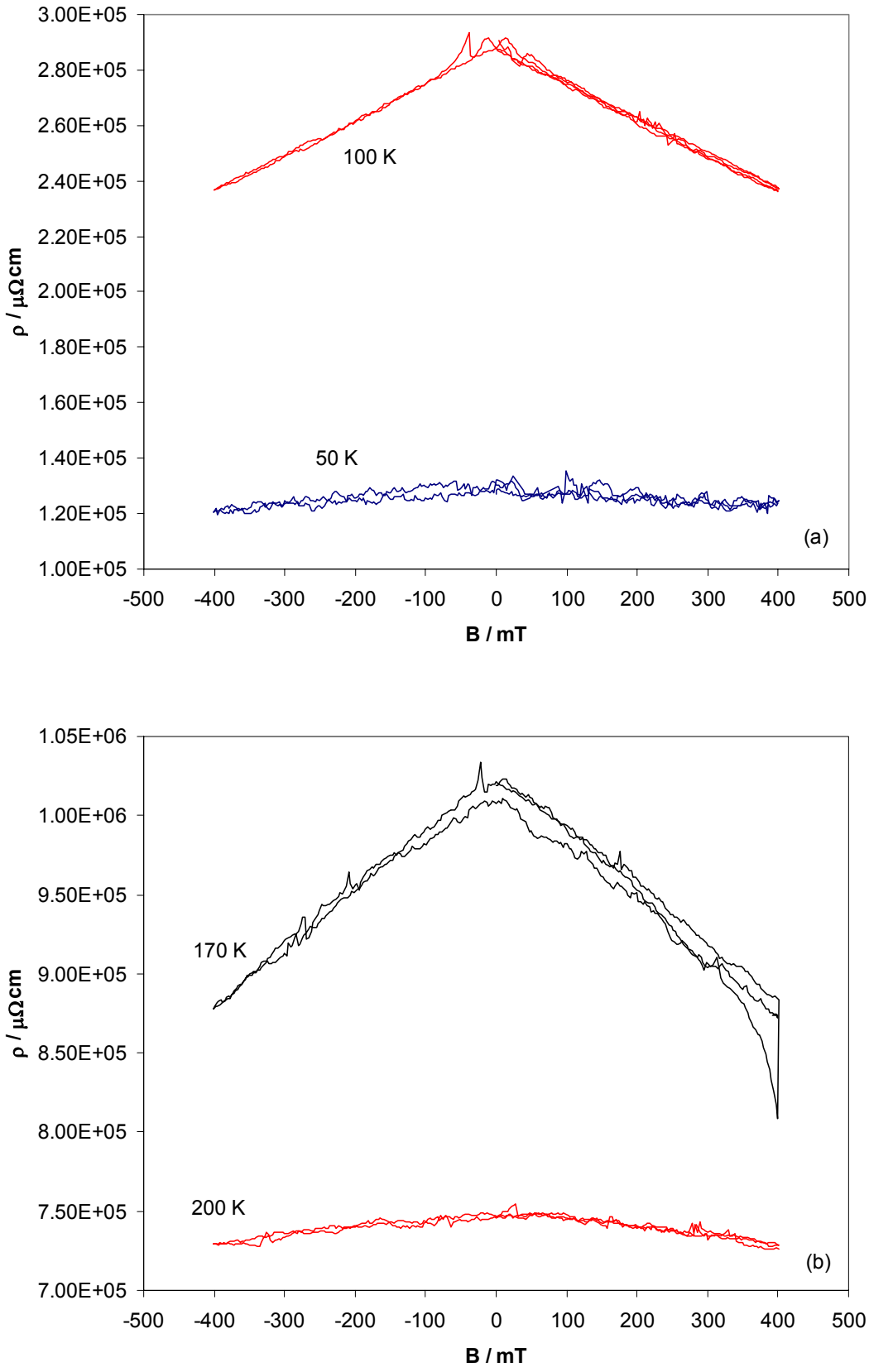

Figure 6.13. Resistivity vs. magnetic field for a $La_{0.60}Ca_{0.40}MnO_3$ film on $SrTiO_3$ (001) at (a) 50 K and 100 K and (b) 170 K and 200 K.

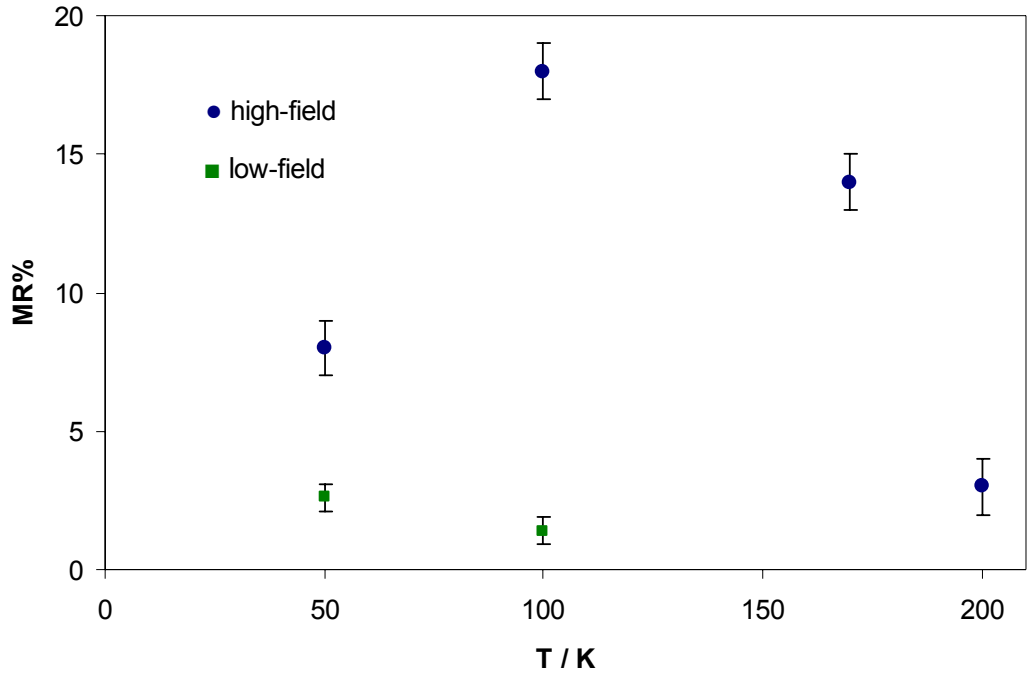

Figure 6.14. Magnetoresistance vs. temperature for a 56 nm $La_{0.60}Ca_{0.40}MnO_3$ film on $SrTiO_3$ (001).

The hysteretic nature of the resistance of the films below their metal-insulator transition temperatures seen in Figure 5.11 and Figure 5.13 is unexpected in a single crystal such as these films. Such butterfly shaped loops are characteristic of samples where the magnetic moments of each domain can switch independently of each other [6]. The independent nature of the magnetic domains can be due to a polycrystalline sample or to a magnetically inhomogeneous material where the ferromagnetic components have a range of coercive fields.

However, X-ray studies have shown that the $La_{0.60}Ca_{0.40}MnO_3$ and $La_{0.59}Ca_{0.41}MnO_3$ films were single crystalline, and so the sample should be single domain. One possible explanation for this discrepancy is that the $La_{0.60}Ca_{0.40}MnO_3$ and $La_{0.59}Ca_{0.41}MnO_3$ films comprise a phase separated mixture of ferromagnetic regions in a non-ferromagnetic matrix, and that there will be a range of Curie temperatures and coercive fields. An explanation of this hysteretic magnetoresistance behaviour is as follows.

The magnetic moments of the components will tend to align with the external field, and hence be parallel, at high fields. As the field reduces towards zero and then

becomes negative, the direction of one component will flip first. This results in an antiparallel configuration between some pairs of domains and introduces domain walls in the conduction path. Because the spins between these pairs of regions are misaligned, it is more difficult for the conduction electrons to pass through the film, which increases the resistance. As the field becomes more negative, more components flip and the number of domain walls will initially increase and then decrease towards zero. The number of domain walls will be zero when all the domains have reversed their moments. The resistance maximum occurs when there is the maximum number of adjacent domains misaligned. For the $La_{0.59}Ca_{0.41}MnO_3$ film the peak resistance occurs at fields of 65 mT at 20 K, 45-50 mT at 50 K and 30 mT at 70 K. The value at 20 K is in good agreement with the coercive field at 20 K from Section 5.5.1. Also note that the coercive field of a typical ferromagnet decreases with increasing temperature. At 100 K, the film as a whole was still insulating, although there may still be locally ferromagnetic regions. At each temperature, and for both the films that showed metallic behaviour at low temperatures, there was little difference between the data for positive and negative fields.

Although the two films that exhibit a low-temperature metallic state both show high-field and low-field MR effects, the MR values for the $La_{0.60}Ca_{0.40}MnO_3$ film were smaller than the corresponding values for the $La_{0.59}Ca_{0.41}MnO_3$ film. These smaller MR values, for the $La_{0.60}Ca_{0.40}MnO_3$ film are consistent with the view that the distribution of phases in this film is more stable and that the external field has a smaller effect on the interactions between the clusters.

For comparison, similar measurements were done on $La_{1-x}Ca_xMnO_3$ films with $x \geq 0.42$, i.e. samples that remained insulating at all temperatures. In no case was there a butterfly shape or a low-field magnetoresistance. A typical plot is shown in Figure 6.15, which was taken at 75 K for the $La_{0.55}Ca_{0.45}MnO_3$ film on $SrTiO_3$ (001). The resistivity decreased linearly with applied field, with a MR of 12% in 400 mT.

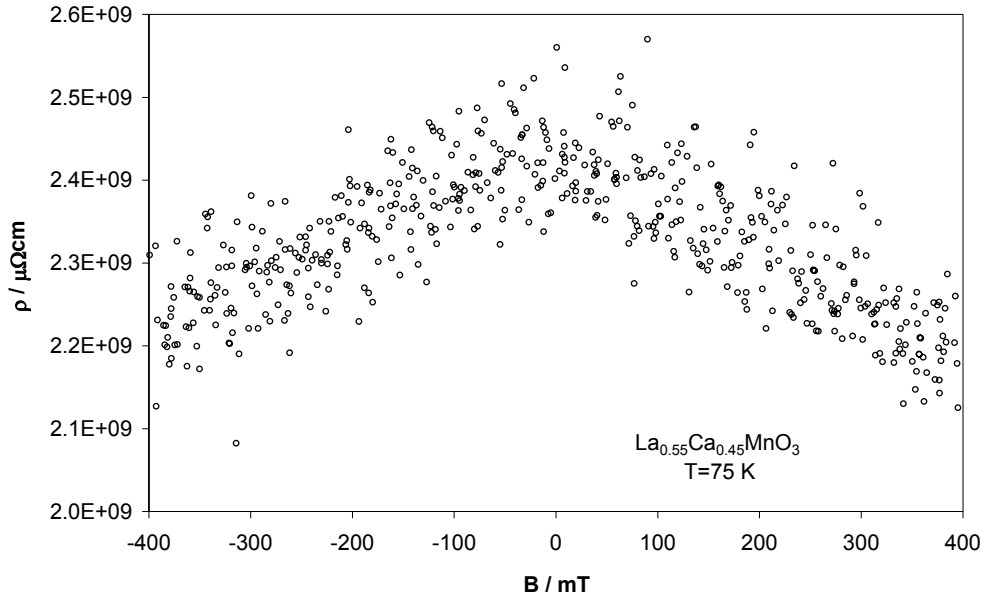

Figure 6.15. Resistivity vs. magnetic field at 75 K for a 54 nm $La_{0.55}Ca_{0.45}MnO_3$ film on $SrTiO_3$ (001).

6.5 Discussion

The effect of an external magnetic field on the resistivity of these samples is consistent with the findings of Chapter 5, in that there are only large FM regions in these films for x=0.40 and 0.41, and that for the films with $0.42 \leq x \leq 0.45$, a field of 400 mT applied along the [100] film direction parallel to the current was not able to increase the ferromagnetic fraction sufficiently to permit conduction through the sample as a whole. The resistivity of the films with $0.42 \leq x \leq 0.45$ has a much lower dependence on the field, so the lower MR values obtained from Figures 6.1-6.4 are reasonable. Conversely, the reduction in the resistivity seen in high fields for the metallic samples under a magnetic field is typical of a double exchange mediated interaction. The magnetic field causes the Mn spins to align themselves parallel to the field and thereby reduce the angle θ between the spins on adjacent Mn ions. The probability of the e_g electron hopping varies as $\cos(\theta/2)$, so this spin alignment will increase itinerant hopping and decrease the resistivity.

Due to the assumed phase-separated nature of these films, there will be boundaries between the phases. Additionally, it seems likely that these films have multiple magnetic domains and so there will be domain walls in the conductive path.

The effect of domain walls has been measured in patterned $La_{0.7}Ca_{0.3}MnO_3$ films grown on $SrTiO_3$ (001). The resistance-area product was found to be 8×10^{-14} Ωm^2 at 77 K [6]. In a domain wall, successive Mn spins are rotated by small angles. A typical 180º domain wall width in a $La_{0.7}Ca_{0.3}MnO_3$ film is around 38 nm or 100 unit cells [14]. In this scenario, adjacent Mn spins will be displaced by 1.8º, and the hopping parameter t will be reduced by approximately 0.01%. This reduction in t in the domain wall alone cannot explain the high resistance of a domain wall. However, mesoscopic phase separation *inside* the domain wall could be the cause of the large domain wall resistance [6]. Significant domain wall resistance is not usually observed in plain films, and only becomes significant when the current is forced to flow through domain walls at constrictions e.g. those patterned into tracks [6]. However, in a phase-separated mixture, as is inferred for these samples, the electrical conduction proceeds via a percolative mechanism and there will be discrete conducting pathways which resemble patterned constrictions.

However, the hysteretic behaviour of the resistance of the single crystal $La_{0.60}Ca_{0.40}MnO_3$ and $La_{0.59}Ca_{0.41}MnO_3$ films below their metal-insulator transition temperatures is unexpected and cannot be explained by double exchange and an additional explanation is required. Recent relaxation studies have indicated that the phase-separated manganites must be considered as an assembly of interacting magnetic clusters [15], with the *inter*cluster interactions, as opposed to *intra*cluster interactions, introducing the collective behaviour and glassiness. Similar time-dependent behaviour has been seen in systems of concentrated magnetic particles [16] and other nanostructure magnetic materials [17], and similar hysteretic magnetoresistance behaviour was seen in the phase-separated cobaltite $La_{0.85}Sr_{0.15}CoO_3$ [18]. The occurrence of qualitatively the same behaviour in a wide variety of physical systems suggests that the hysteretic behaviour and the LFMR effect seen in these $La_{1-x}Ca_xMnO_3$ films is an example of a general phenomenon and not something that is intrinsic to the $La_{1-x}Ca_xMnO_3$ system. Furthermore, temperature dependent neutron scattering measurements on the phase-separated cobaltite $La_{1-x}Sr_xCoO_3$ showed a simultaneous increase in the intensity at low q, arising from the growth of isolated ferromagnetic clusters in a non-ferromagnetic matrix, and the magnetisation below the Curie temperature [18].

Application of an external magnetic field has been shown to increase the size of the ferromagnetic clusters [9]. Additionally, it is thought that a magnetic field will increase the strength of the intercluster interaction [15]. If this is true, then it would allow the behaviour of the phase-segregated state to be readily controlled.

6.6 Summary

The effects on the resistivity of magnetic fields of up to 400 mT have been investigated for the set of $La_{1-x}Ca_xMnO_3$ films on $SrTiO_3$ (001) from the previous chapter. A magnetic field of 400 mT was not able to introduce metallic behaviour into any sample that had remained insulating at low temperature in zero field, but did result in a high-field MR effect at 400 mT of 50% at 90 K for a $La_{0.59}Ca_{0.41}MnO_3$ film grown on $SrTiO_3$ (001) and 60% at 140 K for a $La_{0.60}Ca_{0.40}MnO_3$ film. There was a slight increase of 5 K in the transition temperature at 400 mT for both films.

The effect of a magnetic field was also measured at constant temperatures. For the $La_{0.60}Ca_{0.40}MnO_3$ and $La_{0.59}Ca_{0.41}MnO_3$ films there were both a high-field and low-field MR effects. The high-field effect was seen at all temperatures and the resistivity decreased approximately linearly with increasing field. The maximum high-field MR values at 400 mT were 18% at 100 K for the $La_{0.60}Ca_{0.40}MnO_3$ film and 38% at 70 K for the $La_{0.59}Ca_{0.41}MnO_3$ film. There was no dependence on the sign of the magnetic field. Furthermore, below T_{MI} there was a low-field MR effect of approximately 20% at 20 K for the $La_{0.59}Ca_{0.41}MnO_3$ film and 1-2% at 50 K for the $La_{0.60}Ca_{0.40}MnO_3$ film in fields of 20-50 mT. This low-field magnetoresistance in single-crystalline films suggests that the phase-separated $La_{1-x}Ca_xMnO_3$ films close to the metal-insulator transition are examples of a more general class of material which behaves as an assembly of interacting magnetic particles [15]. This opens up the possibility of controlling the macroscopic behaviour of such materials by altering the intercluster interactions with a magnetic field.

For the insulating films (x>0.41) the high-field resistivity varied approximately linearly with the applied field, with a maximum MR value of 12% in 400 mT at 75 K for a $La_{0.55}Ca_{0.45}MnO_3$ film. No low-field magnetoresistance was seen for these insulating films.

References for Chapter 6

[1] M. Fäth, S. Freisem, A.A. Menovsky, Y. Tomioka, J. Aarts and J.A. Mydosh, *Spatially Inhomogeneous Metal-Insulator Transition in Doped Manganites.* Science **285**, 1540-2 (1999).

[2] N.A. Babushkina, L.M. Belova, D.I. Khomskii, K.I. Kugel, O.Yu. Gorbenko and A.R. Kaul, *Low-temperature transition to a metallic state in* $(La_{0.5}Pr_{0.5})_{0.7}Ca_{0.3}MnO_3$ *films.* Phys. Rev. B **59**, 6994-7000 (1999).

[3] A. Asamitsu, Y. Moritomo, Y. Tomioka, T. Arima and Y. Tokura, *A structural phase transition induced by an external magnetic field.* Nature **373**, 407-9 (1995).

[4] S. Jin, T.H. Tiefel, M. McCormack, R.A. Fastnacht, R. Ramesh and L.H. Chen, *Thousandfold Change in Resistivity in Magnetoresistive La-Ca-Mn-O Films.* Science **264**, 413-5 (1994).

[5] M.-H. Jo, N.D. Mathur, N.K. Todd and M.G. Blamire, *Very large magnetoresistance and coherent switching in half-metallic manganite tunnel junctions.* Phys. Rev. B **61**, R14905-8 (2000).

[6] N.D. Mathur, P.B. Littlewood, N.K. Todd, S.P.Isaac, B.-S. Teo, D.-J. Kang, E.J. Tarte, Z.H. Barber, J.E. Evetts and M.G. Blamire, *Resistance of a domain wall in* $La_{0.7}Ca_{0.3}MnO_3$. J. Appl. Phys. **86**, 6287-90 (1999).

[7] H.Y. Hwang, S.-W. Cheong, N.P. Ong and B. Batlogg, *Spin-Polarized Intergrain Tunneling in* $La_{2/3}Sr_{1/3}MnO_3$. Phys. Rev. Lett. **77**, 2041-4 (1996).

[8] M. Roy, J.F. Mitchell, A.P. Ramirez and P. Schiffer, *A study of the magnetic and electrical crossover region of* $La_{0.5+/-\delta}Ca_{0.5-/+\delta}MnO_3$. J. Phys.: Condens. Mat. **11**, 4843-59 (1999).

[9] P. Levy, F. Parisi, L. Granja, E. Indelicato and G. Polla, *Novel Dynamical Effects and Persistent Memory in Phase Separated Manganites.* Phys. Rev. Lett. **89**, 137001 (2002).

[10] I. Webman, J. Jortner and M.H. Cohen, *Numerical simulation of continuous percolation conductivity.* Phys. Rev. B **14**, 4737-40 (1976).

[11] K.H. Kim, M. Uehara, C. Hess, P.A. Sharma and S.-W. Cheong, *Thermal and Electronic Transport Properties and Two-Phase Mixtures in* $La_{5/8-x}Pr_xCa_{3/8}MnO_3$. Phys. Rev. Lett. **84**, 2961-4 (2000).

[12] W. Prellier, Ch. Simon, A.M. Haghiri-Gosnet, B. Mercey and B. Raveau, *Thickness dependence of the stability of the charge-ordered state in* $Pr_{0.5}Ca_{0.5}MnO_3$ *thin films.* Phys. Rev. B **62**, R16337-40 (2000).

[13] M. Tokunaga, N. Miura, Y. Tomioka and Y. Tokura, *High-magnetic-field study of the phase transition of* $R_{1-x}Ca_xMnO_3$ *(R=Pr, Nd).* Phys. Rev. B **57**, 5259-64 (1998).

[14] S.J. Lloyd, N.D. Mathur, J.C. Loudon and P.A. Midgley, *Magnetic domain-wall width in $La_{0.7}Ca_{0.3}MnO_3$ thin films measured using Fresnel imaging.* Phys. Rev. B **64**, 172407 (2001).

[15] F. Rivadulla, M.A. López-Quintela and J. Rivas, *Origin of the Glassy Magnetic Behaviour of the Phase Segregated State of the Perovskites.* Phys. Rev. Lett. **93**, 167206 (2004).

[16] T. Jonsson, J. Mattsson, C. Djurberg, F.A. Khan, P. Nordblad and P. Svedlindh, *Aging in a Magnetic Particle System.* Phys. Rev. Lett. **75**, 4138-41 (1995).

[17] S. Sahoo, O. Petracic, W. Kleemann, P. Nordblad, S. Cardoso and P.P. Freitas, *Aging and memory in a superspin glass.* Phys. Rev. B **67**, 214422 (2003).

[18] J. Wu, J.W. Lynn, C.J. Glinka, J. Burley, H. Zheng, J.F. Mitchell and C. Leighton, *Intergranular Giant Magnetoresistance in a Spontaneously Phase Separated Perovskite Oxide.* Phys. Rev. Lett. **94**, 037201 (2005).

Chapter 7 A study of relaxation effects and magnetic history dependence via transport and magnetic measurements

7.1 Motivation

The phase-separated nature of the $La_{1-x}Ca_xMnO_3$ system close to the FM-CO phase boundary is now well established [1], and the relative fractions of the competing phases have been successfully changed by altering numerous parameters [2]. However, the actual process by which these fractions change is not well understood. Previous studies have shown that there is a dynamic equilibrium between the competing phases of $La_{1-x}Ca_xMnO_3$ near the low-temperature FM-CO phase boundary, and the isothermal time dependence of the resistivity [3,4] and magnetisation [4] of $La_{0.5}Ca_{0.5}MnO_3$ have been investigated. Figure 7.1 shows $\rho(t)$ and $M(t)$ data for polycrystalline $La_{0.5}Ca_{0.5}MnO_3$ at 5 K. Both sets of data show a logarithmic time dependence over thousands of seconds, with ρ decreasing with time and M increasing. The 50% decrease in ρ is much more significant than the 0.3% increase in the magnetisation. This difference was attributed to limited conductive paths in the film.

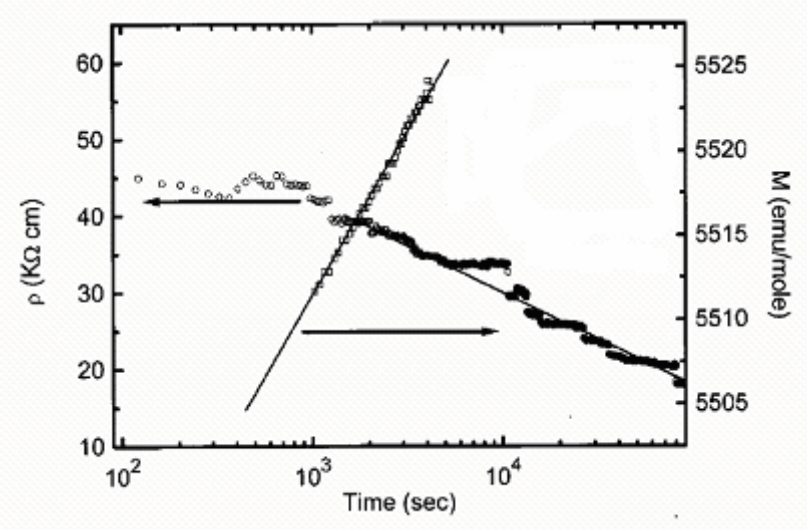

Figure 7.1. Time dependence of ρ and M at 5 K in fields of 7 T and 9 T respectively for polycrystalline $La_{0.5}Ca_{0.5}MnO_3$. (Taken from [4].)

The logarithmic time dependence of the magnetisation seen in Figure 7.1 is typical of a spin glass state. Similar behaviour is predicted from models based on hierarchical strained dynamics, in which each individual step can only proceed once all previous steps have been completed [5]. In this case, the hierarchical process is the growth of the FM phase where the phase boundary moves through discrete energy barriers. However, Sirena *et al*. found that the time dependence in manganite samples comprised both a logarithmic and an exponential component, with the logarithmic component dominating below 30 K and the exponential component being most significant above 100 K [6]. Similar spin-glass behaviour has been seen in phase-separated materials for single crystals [7,8], polycrystalline samples [8-10], and thin films [11], so it appears that the field-dependent behaviour and relaxation phenomena are intrinsic to phase-separated materials and not due to sample morphology. Furthermore, two types of relaxation process were reported for polycrystalline $La_{0.250}Pr_{0.375}Ca_{0.375}MnO_3$ [9]. At low fields, the relaxation was primarily due to domain realignment, whereas at higher fields the relaxation was associated with the enlargement of FM regions.

Furthermore, the low-field magnetoresistance effect observed in the single crystal $La_{1-x}Ca_xMnO_3$ films and discussed previous chapter lead to a postulate that theses phase-separated films are behaving as a collection of ferromagnetic nanoparticles in a non-magnetic matrix. The relaxation behaviour in similar phase-separated systems has been postulated to be primarily due to the interactions between the clusters [12], and consequently the ferromagnetic clusters in phase-separated manganites could be considered as nanoparticles. It is thought that the strength of this intercluster interaction can be tuned by an external magnetic field by altering the size or concentration of these ferromagnetic clusters [12]. If this is true, then the glass-like relaxation seen in many phase-separated manganite systems can be influenced by an external magnetic field. It may be possible to alter the timescale for the relaxation in this way.

Additionally, a memory effect has been observed in many phase-separated manganite systems [3,8,11], where the resistivity fell in a magnetic field and the zero-field resistivity depended primarily on the maximum field experienced. A

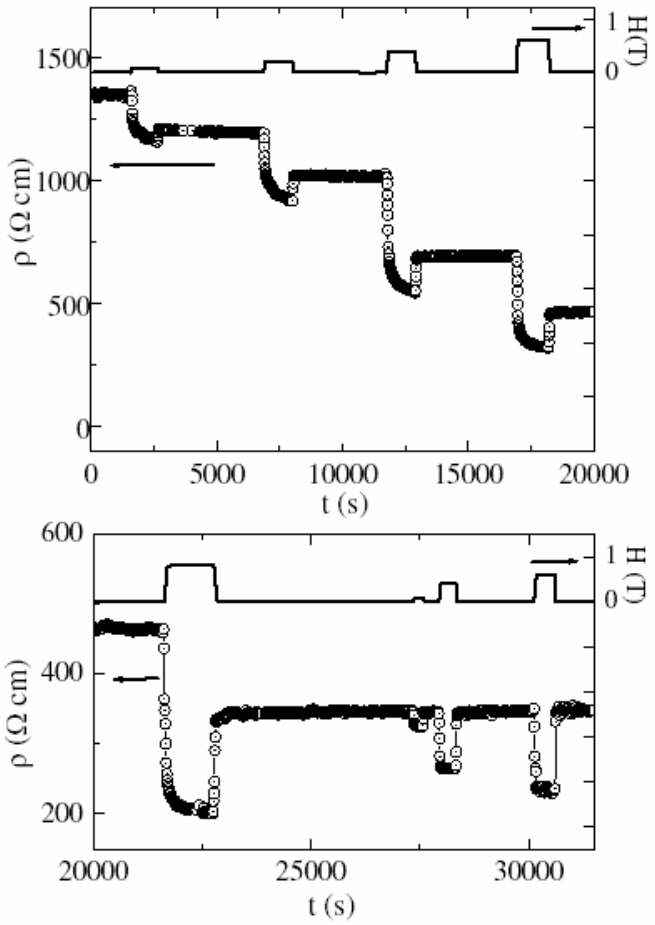

Figure 7.2. Resistivity vs. time and magnetic field at 72 K for polycrystalline $La_{0.5}Ca_{0.5}Mn_{0.95}Fe_{0.05}O_3$. (Adapted from [3].)

typical result is shown in Figure 7.2 for polycrystalline $La_{0.5}Ca_{0.5}Mn_{0.95}Fe_{0.05}O_3$ vs. time and magnetic field at 72 K [3]. There was a logarithmic decrease in ρ at constant field as the system relaxes into its final state.

7.2 Time-dependent measurements

The findings of Chapter 5 suggest that there is a phase-separated mixture of ferromagnetic regions in a non-ferromagnetic matrix at low temperatures in the $La_{0.60}Ca_{0.40}MnO_3$ and $La_{0.59}Ca_{0.41}MnO_3$ films. The low-temperature magnetisation measurements from Section 5.5, where the behaviour depends on the previous magnetic history suggest the existence of a spin-glass. The findings of Chapter 6 support this phase-separated picture through the LFMR effect and furthermore suggest that the interactions between the ferromagnetic clusters are dominant.

To investigate the nature of the phase segregation and the intercluster interactions, the time dependence of the resistivity and magnetisation was measured at constant temperature. In both cases, the temperature was set to be just below the transition temperature, as defined by the peak of $\rho(T)$ and the inflection point in $M(T,H)$. At these temperatures it should be easiest to alter the fraction of FM material, whilst still having a metallic sample for the resistivity measurements. Additional magnetisation data were taken at the same temperature as for the corresponding resistivity measurement and also at 20 K for comparison. Measurements were made in fields up to B=400 mT to see if the relaxation process depended on the applied field. Magnetic fields were always applied along a [100] direction in the film.

7.2.1 Resistivity

Figures 7.3 and 7.4 show the resistivity as a function of time and magnetic field for $La_{0.60}Ca_{0.40}MnO_3$ and $La_{0.59}Ca_{0.41}MnO_3$ films on $SrTiO_3$ (001). The magnetic fields applied were B=0, 100 mT, 200 mT, 300 mT and 400 mT respectively. Prior to taking the data, each sample was cooled from room temperature to the required temperature in zero field. As can be seen from these figures, the resistivity is primarily dependent not only on the current magnetic field, but also on the maximum field experienced. The behaviour of the two samples is qualitatively the same, and the main features are discussed below. Note that the resistivity scales in Figures 7.3 and 7.4 are linear and differ by two orders of magnitude.

Firstly, there were sharp decreases in the resistivity when a field was applied. These are likely to originate in sudden spin- and domain-alignment in the sample and from the enlargement of the FM regions. However, there was a further slow decrease of ρ with time, which implies that the changes in magnetic structure do not all occur instantaneously. This slow decrease can be attributed to the gradual enlargement of the FM regions at the expense of the non-FM matrix. This slow increase of the FM regions is due to the external field.

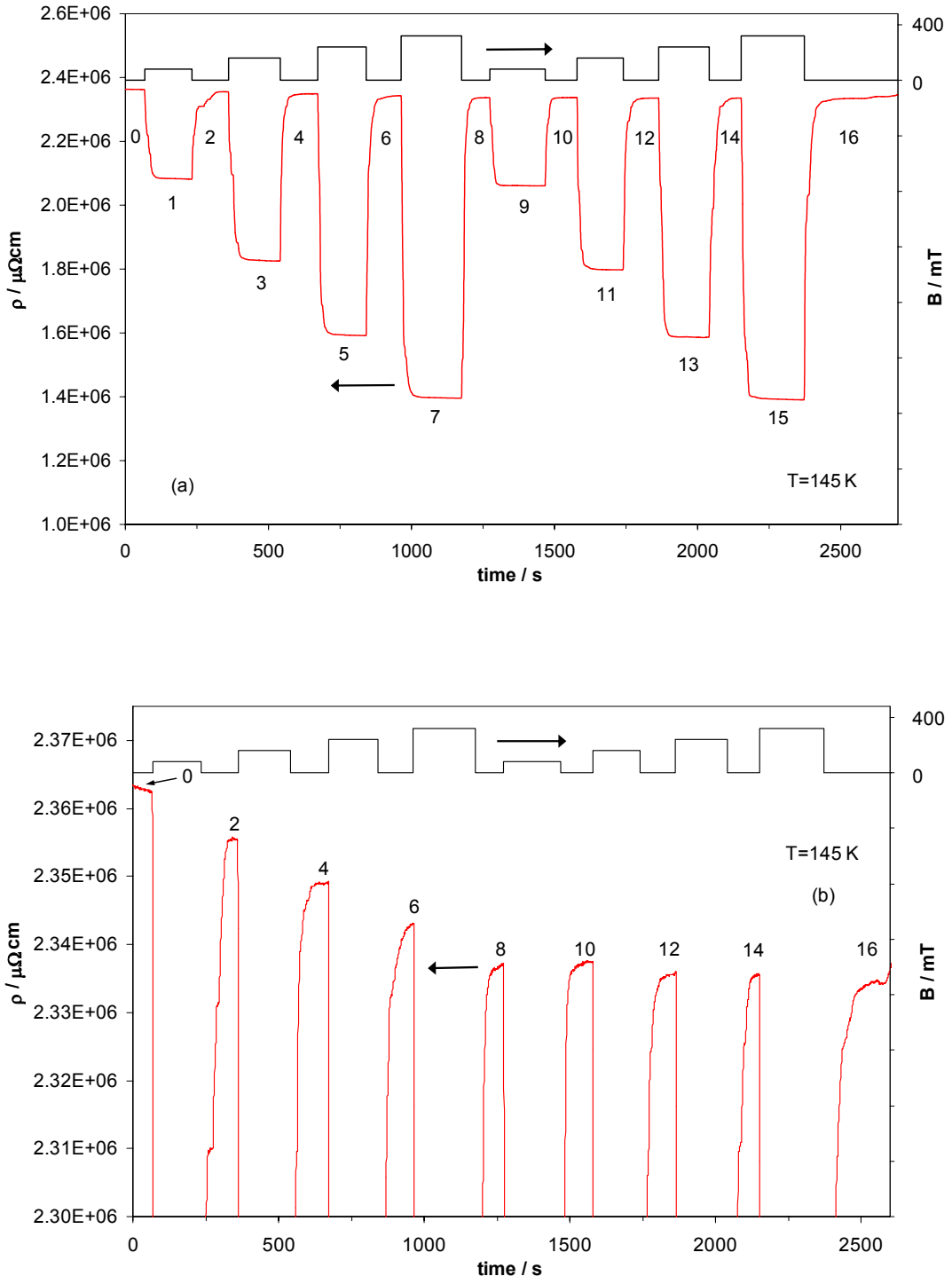

Figure 7.3. (a) Resistivity as a function of time and magnetic field at 145 K for a 56 nm $La_{0.60}Ca_{0.40}MnO_3$ film on $SrTiO_3$ (001). (b) Expanded view showing the reduction in $\rho_{B=0}$. The labels refer to sections of the curve and are discussed in more detail in Section 7.3.

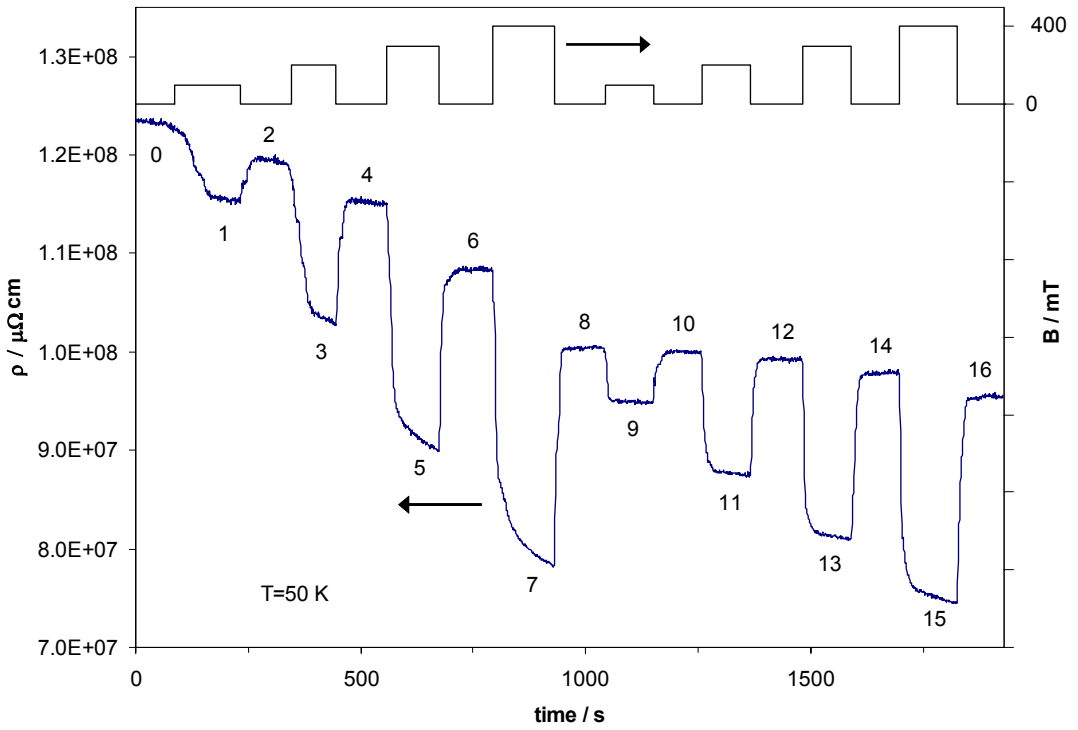

Figure 7.4. Resistivity vs. time and magnetic field at 50 K for a 60 nm $La_{0.59}Ca_{0.41}MnO_3$ film on $SrTiO_3$ (001). The labels refer to sections of the curve and are discussed in more detail in Section 7.3.

Secondly, the remnant resistivity $\rho_{B=0}(t)$ was dependent on the magnetic history of the sample. For both samples, $\rho_{B=0}(t)$ initially decreased approximately linearly with field after larger magnetic fields had been experienced. However, after applying 400 mT the remnant resistivity of the $La_{0.60}Ca_{0.40}MnO_3$ film was reasonably constant, whereas there was a further decrease with time for the $La_{0.59}Ca_{0.41}MnO_3$ film. Since the relaxation process was slower for the $La_{0.59}Ca_{0.41}MnO_3$ film, its FM fraction might still be increasing during this period, which would explain the continued decrease in resistivity. All of this suggests that the $La_{0.60}Ca_{0.40}MnO_3$ film was initially closer to its equilibrium distribution of phases than the $La_{0.59}Ca_{0.41}MnO_3$ film.

Figures 7.3 and 7.4 also show that, for both compositions, there was a slow change with time in the remnant resistivity immediately after a given field was removed. There was a slight increase in resistivity after all fields for $La_{0.60}Ca_{0.40}MnO_3$ and after removing B=400 mT for $La_{0.59}Ca_{0.41}MnO_3$, whereas there was a decrease in $\rho_{B=0}(t)$ for $La_{0.59}Ca_{0.41}MnO_3$ when the immediately preceding field was 300 mT or lower. The difference in sign can be explained as follows. If the

magnetic field had increased the FM fraction f past its equilibrium value f_0, then the system would evolve by reducing f, which would in turn increase ρ. Conversely, if the field did not allow f to reach equilibrium, then f would continue to increase and the resistivity would continue to decrease. This time dependence of $\rho_{B=0}(t)$ is clear evidence that the equilibrium state in these films is phase separated in nature, with $f_0 \neq f_{B=0}$ in each sample.

However, there were some differences in behaviour between the two samples. The initial decrease in resistivity was slower for the $La_{0.59}Ca_{0.41}MnO_3$ film. This might be a consequence of the reduced temperature; where there is less thermal energy to drive the rotation of the Mn spins and domains, i.e. the relaxation process is kinetically driven. Alternatively, due to the smaller ferromagnetic regions in the $La_{0.59}Ca_{0.41}MnO_3$ film the coupling between the ferromagnetic clusters could be weaker resulting in a slower relaxation process.

Figure 7.5 shows the MR values from Figures 7.3 and 7.4. For each sample the MR value is taken to be

$$\frac{\rho_0 - \rho_n}{\rho_0}, \qquad (7.1)$$

where ρ_n is the resistivity of the n^{th} plateau as defined in Figures 5.3 and 5.4. By using this definition, there is an MR value for B=0 after applying a field, due to the time- and field-dependent reduction in the zero-field resistivity.

For all the situations, the MR increased approximately linearly with the applied field. There was a maximum MR value of 41% for B=400 mT for $La_{0.60}Ca_{0.40}MnO_3$ and 36% at 400 mT for $La_{0.59}Ca_{0.41}MnO_3$. Furthermore, there was a slight reduction in the resistance of the $La_{0.60}Ca_{0.40}MnO_3$ film at a given field (typically ~1%) after applying B=400 mT and hence a corresponding small increase in the MR value. Conversely, for the $La_{0.59}Ca_{0.41}MnO_3$ film there was a 20% reduction in resistivity for a given field after applying 400 mT, and a corresponding increase in the MR values. This difference between the two samples supports the view that the distribution of phases in the $La_{0.60}Ca_{0.40}MnO_3$ film was closer to its final equilibrium than in the $La_{0.59}Ca_{0.41}MnO_3$ film.

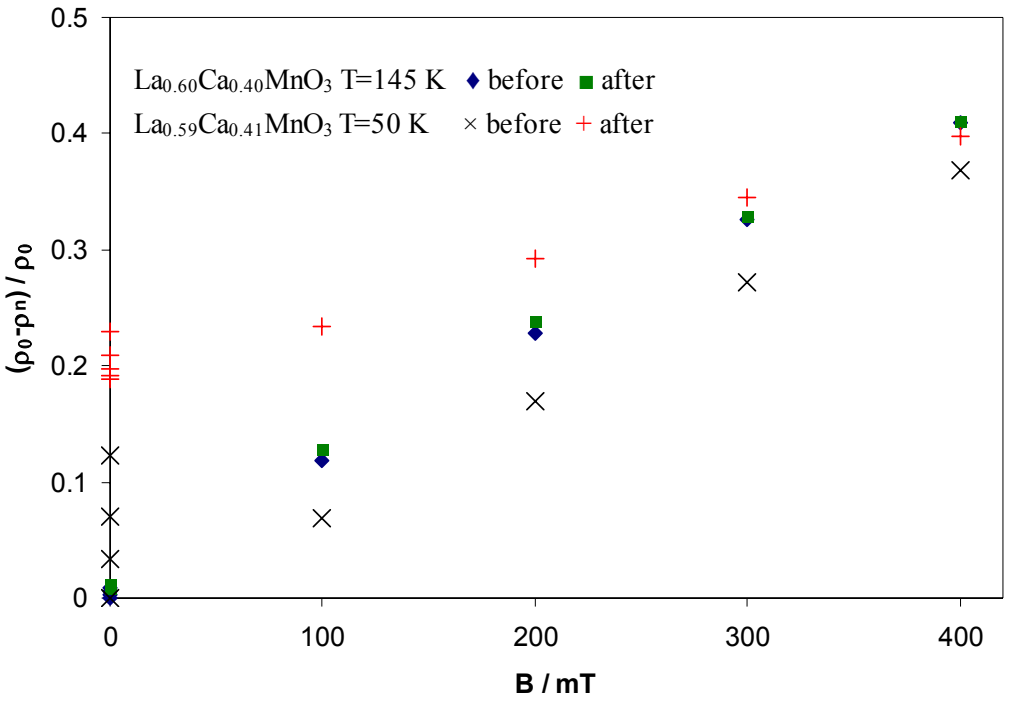

Figure 7.5. Magnetoresistance values plotted as a function of applied field. The symbols correspond to measurements on $La_{0.60}Ca_{0.40}MnO_3$ at 145 K before (♦) and after (■) applying 400 mT and to measurements on $La_{0.59}Ca_{0.41}MnO_3$ at 50 K before (×) and after (+) applying 400 mT. Both films were grown on $SrTiO_3$ (001). Error bars are smaller than the data points.

The behaviour of the two $La_{1-x}Ca_xMnO_3$ films discussed above is similar to that reported in polycrystalline samples of $La_{0.325}Pr_{0.300}Ca_{0.375}MnO_3$ [13] and Fe doped $La_{0.50}Ca_{0.50}MnO_3$ (shown in Figure 7.2) [3]. Both of these compounds have a well-established phase-separated nature, so the behaviour seen in the $La_{1-x}Ca_xMnO_3$ films lends further weight to the postulated phase-separated nature of $La_{1-x}Ca_xMnO_3$ films ($0.40<x<0.45$). The size of the MR effect seen here is comparable with that reported in the literature, e.g. the reduction in resistivity was approximately 50% for a 400 mT field at 72 K in reference [3] compared with 41% for B=400 mT at 145 K for the $La_{0.60}Ca_{0.40}MnO_3$ film on $SrTiO_3$ (001) studied here.

From the above experiments, it appears that the $La_{0.60}Ca_{0.40}MnO_3$ sample had 'remembered' the highest field to which it had been exposed by way of altering the FM fraction f. The maximum field was then encoded in the zero-field resistivity and it should be possible to recover this information through transport techniques. Memory effects in phase-separated manganites have been reported [3,8,11], and such

compounds have been proposed as non-volatile memory elements by Levy *et al*. [8]. However, there are several factors that could also affect the resistance and limit the effectiveness of such a device.

The most obvious limitation is that the device would need to be operated well below 300 K in order to have the maximum sensitivity. The size of the high-field MR effect is greatest close to T_{MI}, and so the resistance of the device should be most sensitive to the magnetic field close to T_{MI}. The transition temperature for the $La_{0.60}Ca_{0.40}MnO_3$ film was 150 K, which is too low a temperature for most practical applications. Furthermore, close to the metal-insulator transition, the magnitude of $d\rho/dT$ is greatest and small temperature fluctuations will have the largest effect on the resistivity. For the measurements at 145 K on the $La_{0.60}Ca_{0.40}MnO_3$ film, the temperature was stable to better than ±0.1 K, and a 0.1 K change in the temperature resulted in a 0.4% change in resistance. By operating further away from the metal-insulator transition temperature, the effect of temperature fluctuations could be reduced. However, this would lead to a reduction in the sensitivity of the device. There is also the issue of how long the information could be reliably stored, e.g. ρ fell by approximately 50% over 10^5 s (roughly one day) for the sample in Figure 7.1 Furthermore, the rate of decrease of the resistivity was not constant over this period. It is also unclear for how long the 'persistent memory' seen by Levy *et al.* [8] permits information to be reliably stored. Additionally, subsequent attempts to write to the device would either need to use a field that was greater than any previously applied field, or the material would need to be 'reset' by warming it up into the paramagnetic phase and randomising the Mn spins before cooling again. Clearly this limits the practicality of such a device. The further decrease of the remnant resistivity with time for the $La_{0.59}Ca_{0.41}MnO_3$ film makes it entirely unsuitable as a memory device.

7.2.2 Magnetisation

A similar study of the time- and field-dependent properties was made on the magnetisation of the $La_{0.60}Ca_{0.40}MnO_3$ and $La_{0.59}Ca_{0.41}MnO_3$ films. Measurements were performed for each sample at the base temperature of the VSM (20 K), at the same temperature as for the corresponding resistivity measurements in Section 7.2.1 and just below the Curie temperature as determined in Section 5.5.2. Prior to taking

the data, the films were demagnetised by applying an alternating positive and negative field with amplitude reducing from $\mu_0 H$=400 mT in steps of 5%. Again, the maximum field that the sample has been exposed to appeared to be encoded into the material via the remnant magnetisation. However, the sensitivity was much reduced compared with the resistivity measurements. Figures 7.6 to 7.8 show the time and field dependence of the magnetisation for the $La_{0.60}Ca_{0.40}MnO_3$ film at 200 K, 145 K, and 20 K respectively and Figures 7.9 to 7.11 show the behaviour at 150 K, 50 K and 20 K for the $La_{0.59}Ca_{0.41}MnO_3$ film. Note that the smallest field step is 100 mT and that the coercive for both films at 20 K was roughly 50 mT. The section therefore describes the effect of fields greater than H_C, and is not concerned with minor hysteresis loops.

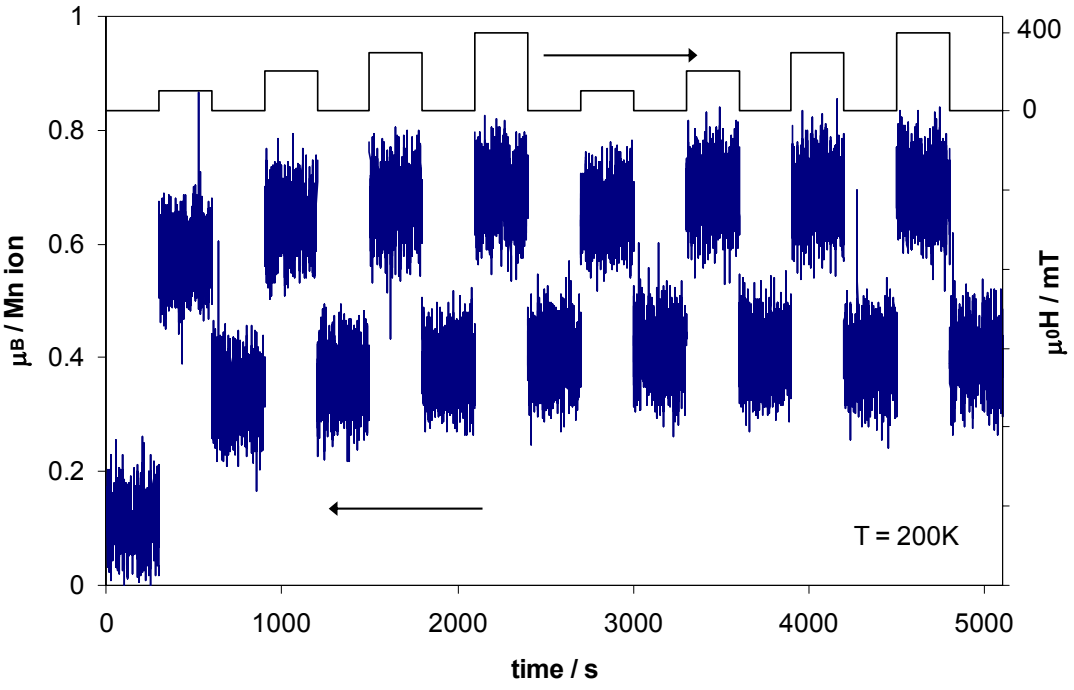

Figure 7.6. Magnetisation vs. time at different magnetic fields at 200 K for a 56 nm $La_{0.60}Ca_{0.40}MnO_3$ film on $SrTiO_3$ (001).

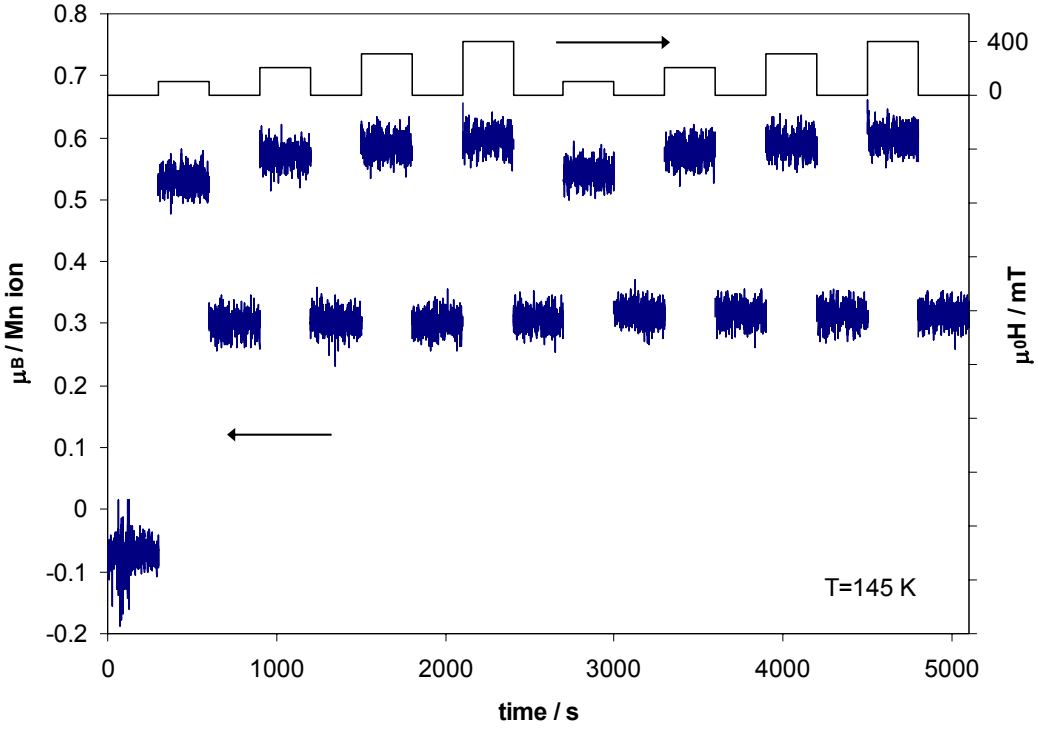

Figure 7.7. Magnetisation vs. time at different magnetic fields at 145 K for a 56 nm $La_{0.60}Ca_{0.40}MnO_3$ film on $SrTiO_3$ (001).

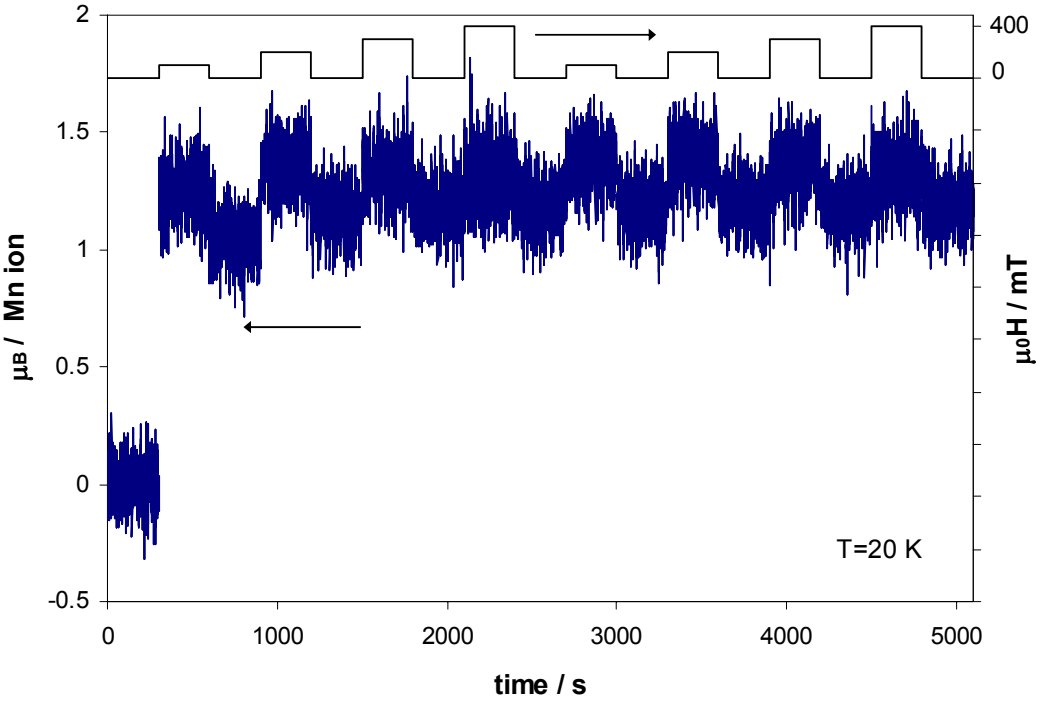

Figure 7.8. Magnetisation vs. time at different magnetic fields at 20 K for a 56 nm $La_{0.60}Ca_{0.40}MnO_3$ film on $SrTiO_3$ (001).

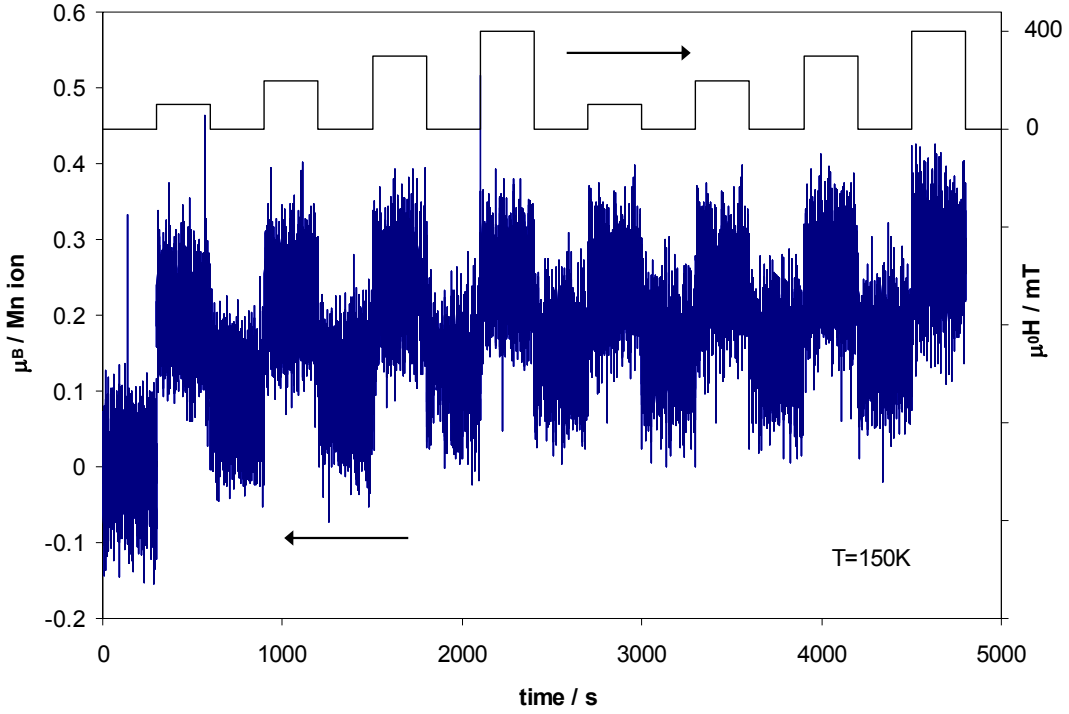

Figure 7.9. Magnetisation vs. time at different magnetic fields at 150 K for a 60 nm $La_{0.59}Ca_{0.41}MnO_3$ film on $SrTiO_3$ (001).

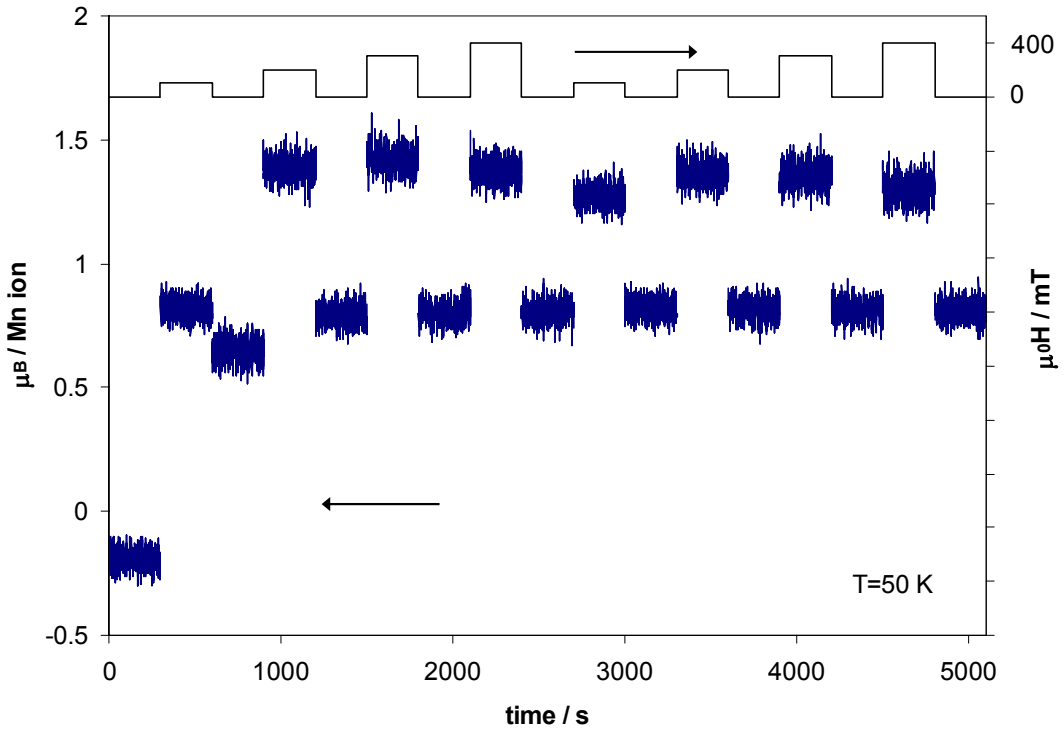

Figure 7.10. Magnetisation vs. time at different magnetic fields at 50 K for a 60 nm $La_{0.59}Ca_{0.41}MnO_3$ film on $SrTiO_3$ (001).

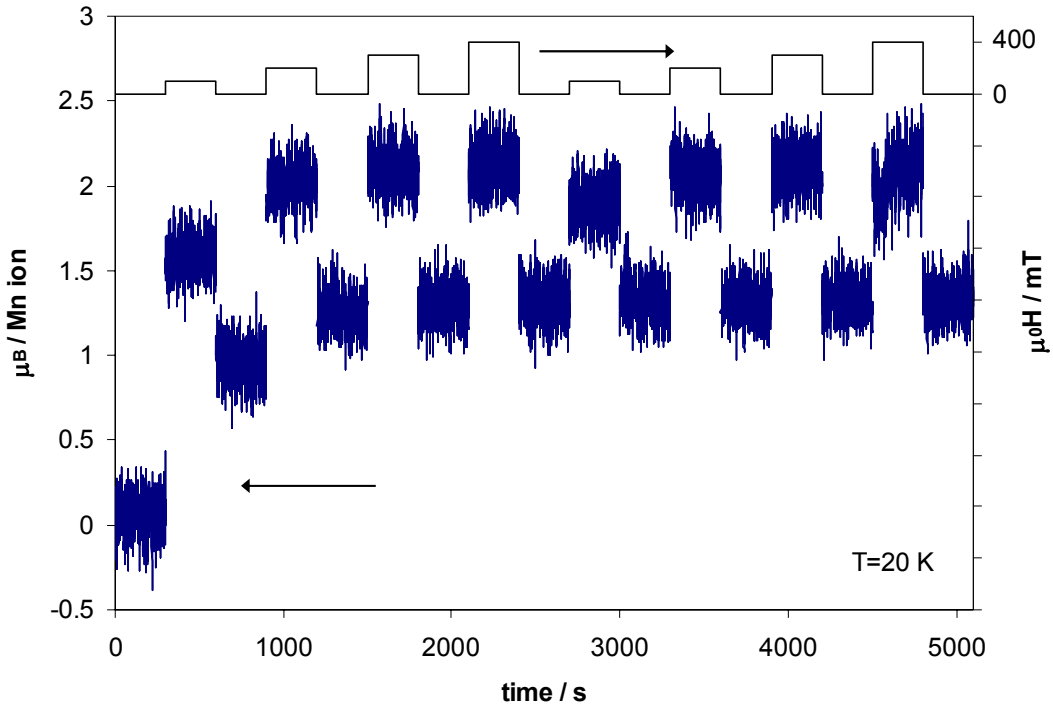

Figure 7.11. Magnetisation vs. time at different magnetic fields at 20 K for a 60 nm $La_{0.59}Ca_{0.41}MnO_3$ film on $SrTiO_3$ (001).

As can be seen from Figures 7.6-7.11, in each case the magnetisation was greater when there was an external field was applied. Furthermore, M increased with increasing field, and as expected the signal was greater at lower temperatures. As for the resistivity measurements, the remnant magnetisation M_R depended on the maximum field experienced and a memory effect was seen for both the $La_{0.60}Ca_{0.40}MnO_3$ and $La_{0.59}Ca_{0.41}MnO_3$ films at all temperatures. This is in contrast with the resistivity measurements, where the memory effect was only seen for the $La_{0.60}Ca_{0.40}MnO_3$ film. However, there were differences in the size of the memory effects for the two films.

For the $La_{0.60}Ca_{0.40}MnO_3$ film the difference in M_R values after applying 100 mT and 400 mT was 15% at 200 K, 3% at 145 K and 12% at 20 K. The reduction in M_R from 200 K to 145 K could be due to the fact that when the sample is further below the Curie temperature, more of the film should have undergone the paramagnetic-ferromagnetic transition, so the effect of the magnetic field on the FM fraction should be reduced. However, this cannot explain the increased difference at 20 K.

The same trend was observed for the $La_{0.59}Ca_{0.41}MnO_3$ film, with differences in M_R after applying 100 mT and 400 mT of 38% at 150 K, 23% at 50 K and 27% at 20 K. However, as mentioned previously, this sample was thought to be further from its equilibrium value of f, so a larger memory effect was expected.

7.3 Relaxation studies

To provide further insight into the mechanisms involved in the magnetoresistance effect and the behaviour of $\rho(t)$, the time dependence of ρ was modelled as

$$\rho(t) = a + b\exp(-(t - t_0)/\tau), \qquad (7.2)$$

where a, b and τ are parameters that were fitted to the data using a standard least-squares minimisation process and t_0 is the time at which the field was altered. Some data points at the start of each segment were rejected because the field was still settling. The values obtained for the time constant τ were sensitive to the number of data points rejected in this way. Also, the early points correspond mainly to spin and domain rotation, and not to enlargement of the ferromagnetic regions. Figure 7.12 show the values of τ as a function of field for the $La_{0.60}Ca_{0.40}MnO_3$ film that correspond to the 16 relaxation events as defined in Figures 7.3.

For each applied field the relaxation was slowest when the field was applied prior to applying 400 mT (events 1, 3, 5 and 7). The largest value of τ was for the initial application of 100 mT (event 1). For all fields, the time constant was 5-10 times smaller after prior application of 400 mT (events 9, 11, 13 and 15), suggesting that the final state was reached in a shorter time. There was little correlation between the time constant and the size of the applied field.

The values for the relaxation after removal of a field (i.e. relaxation in zero field, events 2, 4, 6, 8, 10, 12, 14 and 16) showed little dependence on both the maximum field experienced and the immediately preceding field. Furthermore, the values for τ for relaxation with an applied field after previous exposure to 400 mT (events 9, 11, 13 and 15) were similar to the zero-field relaxation values. The fact that these three situations all gave similar values for τ indicates that the mechanisms

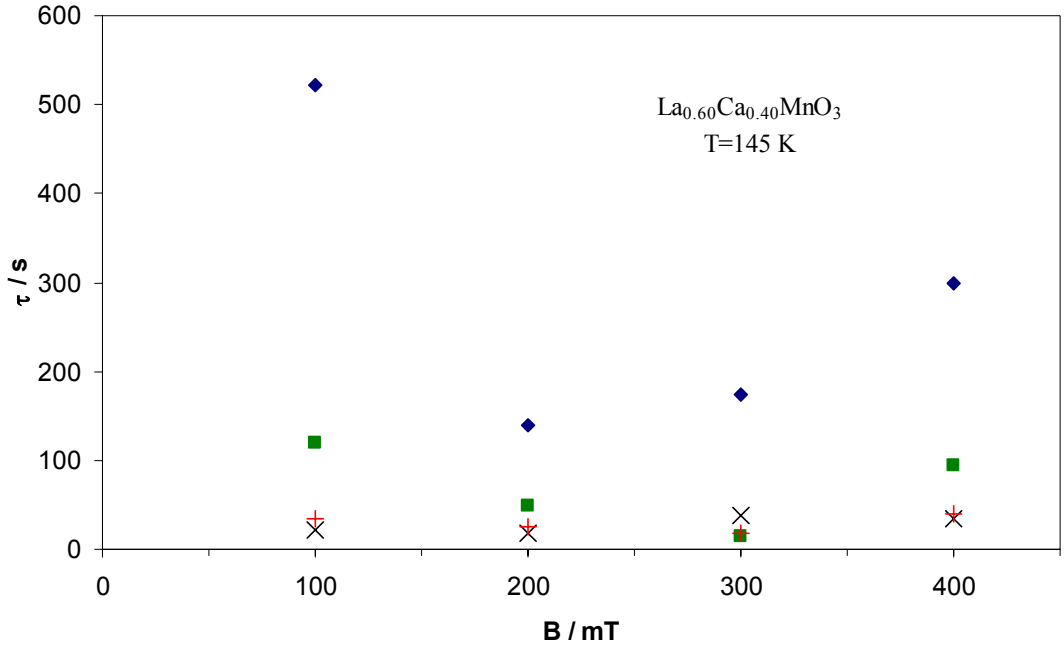

Figure 7.12. Values of τ as a function of magnetic field for a 56 nm $La_{0.60}Ca_{0.40}MnO_3$ film at 145 K. The symbols correspond to relaxation before (♦, events 1, 3, 5, and 7) and after (■, events 9, 11, 13 and 15) applying 400 mT. . Additionally, the values for relaxation in zero field both before (×, events 2, 4, 6 and 8) and after (+, events 10, 12, 14 and 16) applying 400 mT are shown as a function of the immediately preceding field. Error bars are comparable with the size of the symbols.

involved are similar for each case and the interactions between the ferromagnetic clusters are of similar strength. During these relaxation processes, the Mn spins and domains rotate, but there may be no change in the FM fraction.

Figure 7.13 shows the corresponding values of τ for the 16 relaxation events from Figure 7.4 for the $La_{0.59}Ca_{0.41}MnO_3$ film at 50 K. Again, the values obtained showed little correlation with magnetic field. The values for relaxation in zero field (events 2, 4, 6, 8, 10, 12, 14 and 16) were similar (in the range 10-100 s) to the values for the $La_{0.60}Ca_{0.40}MnO_3$ film. However the values for the initial application of a field (events 1, 3, 5 and 7) were smaller than the values for the corresponding field for $La_{0.60}Ca_{0.40}MnO_3$. This is counter-intuitive, as the decrease in resistance appeared slower for the $La_{0.59}Ca_{0.41}MnO_3$ film as shown in Figures 7.3 and 7.4. However, this can be explained as follows. The change in resistivity with time has the same structure for the two films, namely the sudden initial decrease from spin alignment

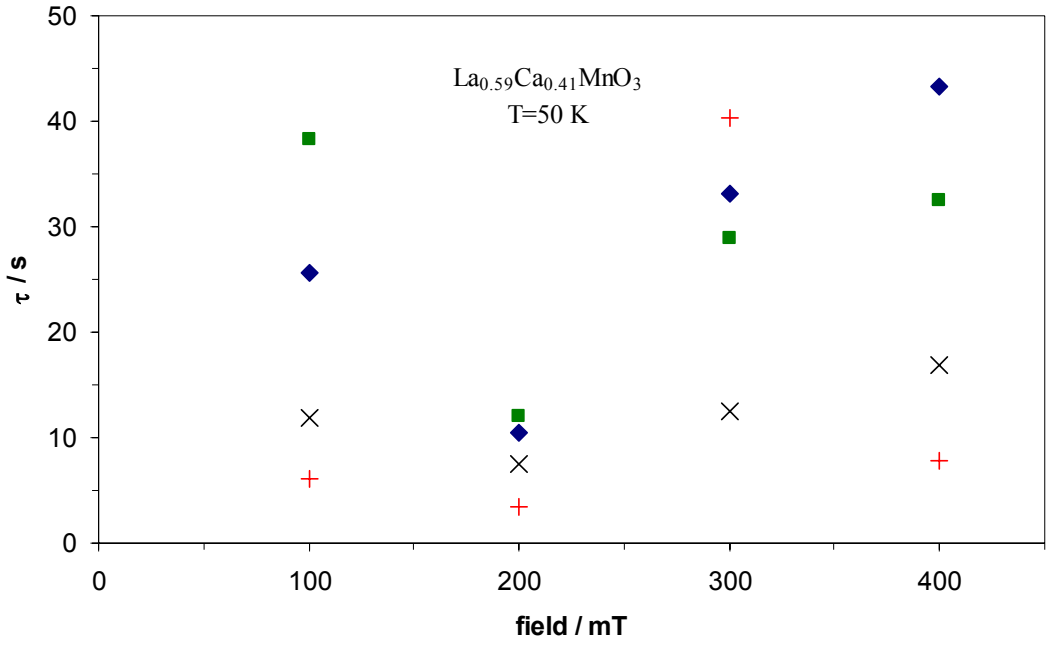

Figure 7.13. Values of τ as a function of magnetic field for a 60 nm $La_{0.59}Ca_{0.41}MnO_3$ film at 50 K before (♦, events 1, 3, 5, and 7) and after (■, events 9, 11, 13 and 15) applying 400 mT. Additionally, the values for relaxation in zero field both before (×, events 2, 4, 6 and 8) and after (+, events 10, 12, 14 and 16) applying 400 mT are shown as a function of the immediately preceding field. Error bars are comparable with the size of the symbols.

and then the gradual decrease due to ferromagnetic enlargement. For the $La_{0.59}Ca_{0.41}MnO_3$ film the change in ferromagnetic fraction *f* is relatively more significant than for the $La_{0.60}Ca_{0.40}MnO_3$ film, so the ratio of the coefficients *b/a* is about 0.1 for $La_{0.59}Ca_{0.41}MnO_3$, compared with a value of 0.01 for $La_{0.60}Ca_{0.40}MnO_3$. The resistance then decreases by a larger amount during the enlargement phase for $La_{0.59}Ca_{0.41}MnO_3$, but the relative rate of decrease is slower for $La_{0.59}Ca_{0.41}MnO_3$ than for $La_{0.60}Ca_{0.40}MnO_3$. The larger value of *b/a* and the larger relative change in resistance for the $La_{0.59}Ca_{0.41}MnO_3$ film suggest that this film is further from its equilibrium distribution of phases.

Similar behaviour with time constants around 500 s has been seen in tracks patterned into $La_{0.59}Ca_{0.41}MnO_3$ films grown on $NdGaO_3$ (001) substrates [14]. This suggests that such time-dependent behaviour is intrinsic to phase-separated $La_{1-x}Ca_xMnO_3$ films with these compositions, and is not a direct effect of the choice of substrate. The relaxation process seen in polycrystalline $La_{0.5}Ca_{0.5}Mn_{0.95}Fe_{0.05}O_3$ in

[3] corresponds to a value for τ of 1.8×10^4 s. This value is roughly 40 times greater than the values observed for the films, which suggests that, although the behaviour for films and polycrystalline material is qualitatively the same, there are nevertheless differences between the behaviour of different types of sample.

Attempts were made to fit the magnetisation data to a similar model. The poor signal-to-noise ratio meant that it was difficult to extract any quantitative values. A naïve attempt at fitting an exponential curve gave values of τ in the range 10^3-10^4 s, although the associated errors are comparable with these values. These values were almost independent of field and are at least an order of magnitude higher than the corresponding values for the transport data. The longer relaxation time for the magnetisation is consistent with the literature [4].

7.4 Discussion

The time- and field-dependent behaviour and the memory effect seen in the resistivity and magnetisation seen above can be explained as follows. When the field was applied the spins and domains partially aligned, hence increasing the magnetisation. In double exchange, the alignment of the Mn spins will increase the probability of the e_g electron hopping between Mn ions and decrease the resistivity. The fraction of FM material can be also increased by the field via a step-wise movement of the ferromagnetic phase boundary through energy barriers, which will increase M and decrease ρ further. A given field H permitted f to increase through all the energy barriers up to a set level. Increasing H further allowed more barriers to be overcome and thus f increased further. When the field was removed the spins and domains misaligned their orientation to reduce the magnetostatic energy, but f did not decrease. Subsequent application of $H<H_{max}$ aligned the spins and domains but did not increase f further. A schematic of this process is shown in Figure 7.14.

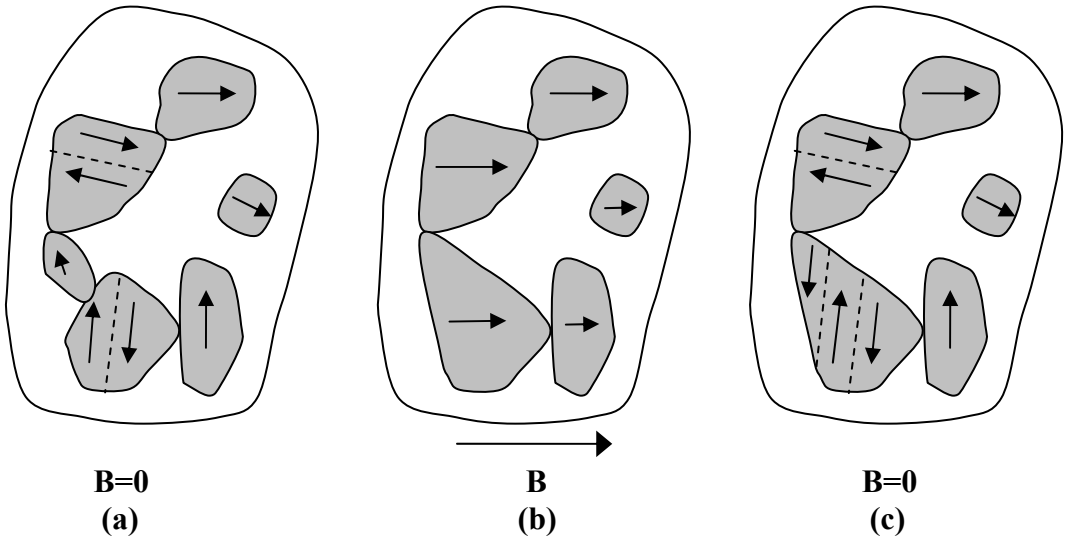

Figure 7.14. Schematic of the magnetic domain structure showing the ferromagnetic regions (grey) in the insulating matrix (white) (a) initially, (b) with a magnetic field and (c) after removal of the field.

From the relaxation data we can obtain some information about the timescales of the processes involved. The initial decrease in resistivity due to the alignment of spins and domain is quick, but the enlargement of the FM regions is slower, although applying a field for 30 s was found to be sufficient to alter the relative fractions of the competing phases. This is 10 times longer than was found for $La_{0.325}Pr_{0.300}Ca_{0.375}MnO_3$ at 95 K [8]. The enlargement of the FM state proceeds at the expense of an insulating non-ferromagnetic state. This insulating state is probably a paramagnetic insulator, but the charge-ordered state cannot be ruled out.

The rotation of the ferromagnetic domains might result in an increased average domain size. This would require domain walls to overcome energy barriers when they move through the film past pinning sites such as dislocations, magnetic inhomogeneities or oxygen vacancies. It is possible that the motion of the domain walls past these sites is most difficult, and hence slowest, the first time a field is applied, but subsequent movements are easier, hence the quicker relaxation. Also, the motion of the domain walls past pinning sites might be permanent, so the increase in domain size is also permanent (as distinct from the increase in FM fraction which is also permanent).

There is similarity in the behaviour of glassy states and phase-separated manganites. The origin of the phase-separated phenomena in the manganites is thought to be in the local frustration between ferromagnetic and antiferromagnetic exchanges [15] that originate in the local strain states that occur at the boundary between the competing phases [10]. These intrinsic strain states are due to slight differences in the lattice parameters of the two phases caused by the cooperative Jahn-Teller distortions that are present in the insulating state [16], but are not found in the FM phase [17]. The magnitude of the strain has been shown to depend on grain size for polycrystalline samples [18]. The changes of the relative fractions of the phases then occur by the martensitic-like growth of one phase within a parent phase. However, recent relaxation studies on phase-separated manganites [12] have explained the glassy behaviour by considering the interactions between the ferromagnetic clusters.

7.5 Summary

The time- and field-dependent properties of resistivity and magnetisation have been investigated at constant temperature for $La_{0.60}Ca_{0.40}MnO_3$ and $La_{0.59}Ca_{0.41}MnO_3$ films on $SrTiO_3$ (001). Both the resistivity and magnetisation showed dependence on the magnetic history of the sample, in that, for a given magnetic field, the resistivity was lower and the magnetisation was higher if the sample had previously been exposed to 400 mT. The resistivity decreased linearly with increasing field, and the magnetisation was in general larger for higher magnetic fields. High-field magnetoresistance values of 41% at 145 K for $La_{0.60}Ca_{0.40}MnO_3$ and 36% at 50 K for $La_{0.59}Ca_{0.41}MnO_3$ were seen in fields of 400 mT. Finally, for both samples the zero-field resistivity depended on the maximum field applied up to the limit of the apparatus (400 mT). This behaviour was attributed primarily to the increase in FM fraction induced by the external field. From the size of the change of resistivity in a magnetic field, it was inferred that the $La_{0.60}Ca_{0.40}MnO_3$ film was closer to its equilibrium state than the $La_{0.59}Ca_{0.41}MnO_3$ film.

The time dependence of relaxation processes was also studied. For the resistivity, there was exponential behaviour immediately after the field was altered, with time constants in the range 10-1000 s that depended on the magnetic history of

the sample. In the majority of cases, the relaxation process was quicker for measurements after applying 400 mT. For these cases, the field will have increased the extent ferromagnetic regions, which will increase the interaction between the ferromagnetic clusters and should result in a shorter relaxation time. It was not possible to extract any quantitative values for relaxation studies performed on magnetisation data due to the poor signal-to-noise ratio.

References for Chapter 7

[1] M. Uehara, S. Mori, C.H. Chen and S.-W. Cheong, *Percolative phase separation underlies colossal magnetoresistance in mixed-valent manganites.* Nature **399**, 560-3 (1999).

[2] N.D. Mathur and P.B. Littlewood, *The self-organised phases of manganites.* Solid State Commun. **119**, 271-80 (2001).

[3] P. Levy, F. Parisi, L. Granja, E. Indelicato and G. Polla, *Novel Dynamical Effects and Persistent Memory in Phase Separated Manganites.* Phys. Rev. Lett. **89**, 137001 (2002).

[4] M. Roy, J.F. Mitchell and P. Schiffer, *Time dependent effects and transport evidence for phase separation in* $La_{0.5}Ca_{0.5}MnO_3$. J. Appl. Phys. **87**, 5831-3 (2000).

[5] R.G. Palmer, D.L. Stein, E. Abrahams and P.W. Anderson, *Models of Hierarchically Constrained Dynamics for Glassy Relaxation.* Phys. Rev. Lett. **53**, 958-61 (1984).

[6] M. Sirena, L.B. Steren and J. Guimpel, *Magnetic relaxation in bulk and film manganite compounds.* Phys. Rev. B **64**, 104409 (2001).

[7] A. Anane, J.-P. Renard, L. Reversat, C. Dupas, P. Veillet, M. Viret, L. Pinsard and A. Revcolevschi, *Colossal resistive relaxation effects in a* $Pr_{0.67}Ca_{0.33}MnO_3$ *single crystal.* Phys. Rev. B **59**, 77-80 (1999).

[8] P. Levy, F. Parisi, J. Sacanell, L. Granja, M. Quintero, J. Curiale, G. Polla, G. Leyva, R.S. Freitas, L. Ghivelder, C. Acha, T.Y. Koo and S.-W. Cheong, *Persistent magnetoresistive memory in phase separated manganites.* J. Magn. Magn. Mater. **258-259**, 293-5 (2003).

[9] I.G. Deac, S.V. Diaz, B.G. Kim, S.-W. Cheong and P. Schiffer, *Magnetic relaxation in* $La_{0.250}Pr_{0.375}Ca_{0.375}MnO_3$ *with varying phase separation.* Phys. Rev. B **65**, 174426 (2002).

[10] M. Uehara and S.-W. Cheong, *Relaxation between charge order and ferromagnetism in manganites: Indication of structural phase separation.* Europhys. Lett. **52**, 674-80 (2000).

[11] N.A. Babushkina, L.M. Belova, D.I. Khomskii, K.I. Kugel, O.Yu. Gorbenko and A.R. Kaul, *Low-temperature transition to a metallic state in* $(La_{0.5}Pr_{0.5})_{0.7}Ca_{0.3}MnO_3$ *films.* Phys. Rev. B **59**, 6994-7000 (1999).

[12] F. Rivadulla, M.A. López-Quintela and J. Rivas, *Origin of the Glassy Magnetic Behaviour of the Phase Segregated State of the Perovskites.* Phys. Rev. Lett. **93**, 167206 (2004).

[13] P. Levy, F. Parisi, M. Quintero, L. Granja, J. Curiale, J. Sacanell, G. Leyva, G. Polla, R.S. Freitas and L. Ghivelder, *Nonvolatile magnetoresistive memory in phase separated* $La_{0.325}Pr_{0.300}Ca_{0.375}MnO_3$. Phys. Rev. B **65**, 140401(R) (2002).

[14] B.B. van Aken, private communication.

[15] J.A. Mydosh, *Spin glasses: An experimental introduction*, Taylor & Francis, London (1993).

[16] P.G. Radaelli, D.E. Cox, M. Marezio and S.-W. Cheong, *Charge, orbital, and magnetic ordering in* $La_{0.5}Ca_{0.5}MnO_3$. Phys. Rev. B **55**, 3015-23 (1997).

[17] P.G. Radaelli, D.E. Cox, M. Marezio, S.-W. Cheong, P.E. Schiffer and A.P. Ramirez, *Simultaneous Structural, Magnetic, and Electronic Transitions in* $La_{1-x}Ca_xMnO_3$ *with* $x=0.25$ *and* 0.50. Phys. Rev. Lett. **75**, 4488-91 (1995).

[18] V. Podzorov, B.G. Kim, V. Kiryukhin, M.E. Gershenson and S.-W. Cheong, *Martensitic accommodation strain and the metal-insulator transition in manganites.* Phys. Rev. B **64**, 140406(R) (2001).

Chapter 8 Conclusions and outlook

8.1 Conclusions

The perovskite manganite $La_{1-x}Ca_xMnO_3$ ($0<x<1$) is well known for having distinct phases that can coexist over short lengthscales. In this dissertation it has been shown that the effects of substrate-induced strain are sufficient to alter the electrical and magnetic properties and make the phase diagram more complex. There is a phase-separated mixture of a ferromagnetic metal and a non-magnetic insulator around x=0.4 and the limit of metallic behaviour is x=0.41 for 60 nm films grown on $SrTiO_3$ (001). However, weak ferromagnetic behaviour persisted up to x=0.45. The saturation magnetisation was reduced to approximately 40% of the spin-aligned value for x=0.40 and 0.41, whereas it was at most 5% of the spin-aligned value for x=0.42-0.45. These variations from the bulk behaviour are thought to be due to the substrate-induced strain altering the crystal symmetry and altering the Mn-O-Mn bond lengths, thereby making the cubic ferromagnetic state less stable. It should be noted that this new limit of metallic behaviour might depend on the film thickness.

The effect of a magnetic field on the resistivity was also investigated. As for the bulk material [1], the high-field magnetoresistance was greatest close to the metal-insulator transition and decreased away from T_{MI}. The maximum high-field MR for the $La_{0.59}Ca_{0.41}MnO_3$ film was 50% at 400 mT and 95 K and 60% for the $La_{0.60}Ca_{0.40}MnO_3$ film at 140 K and the same field. The high-field MR was much reduced for films with x>0.41 and no metal-insulator transition was seen at any temperature down to 20 K for fields of up to 400 mT. Measurements of resistance versus field for metallic films below T_{MI} at constant temperature revealed a low-field MR of ~20% in fields of 20-50 mT for $La_{0.59}Ca_{0.41}MnO_3$ and 1-2% in similar fields for $La_{0.60}Ca_{0.40}MnO_3$. The presence of a LFMR effect in these single crystal films supports the recent view that the phase-separated manganites close to a metal-insulator transition should be thought of as a glassy collection of interacting magnetic particles [2], where the interactions between the ferromagnetic clusters are predominately responsible for the magnetic properties. Furthermore, it appears that the strength of the interaction, and hence the resultant relaxation and memory effects, can be tuned by external magnetic fields.

The time and magnetic field dependence of the resistivity and magnetisation of the metallic compositions was investigated. The zero-field resistivity was found to depend primarily on the maximum field experienced. This behaviour was attributed to the field-induced enlargement of the ferromagnetic regions in a phase-separated mixture. A similar dependence on the maximum field experienced was observed for the remnant magnetisation.

The zero-field resistivity values varied with time and the preceding magnetic field. In particular the sign of the change was shown to depend on the preceding field, where for values below a critical field the zero-field resistivity continued to decrease with time, whereas it increased for larger values of the field. This behaviour is consistent with a non-equilibrium phase-separated mixture where the FM fraction can be altered by an external stimulus (here the magnetic field), and the system is relaxing into its final equilibrium state. Crucially, it was inferred that for a virgin sample the equilibrium FM fraction $f_0 \neq f_{B=0}$. The isothermal time dependence of the resistivity was shown to have a negative exponential form, with time constants in the range 10-1000 s. The magnetisation also decreased slowly with time, with time constants crudely estimated to be in the range 10^4-10^5 s.

From the reduced values of T_{MI} and T_C, and from the larger MR values, the $La_{0.59}Ca_{0.41}MnO_3$ film was inferred to be further from its equilibrium distribution of phases than the $La_{0.60}Ca_{0.40}MnO_3$ film. This was as expected, as the $La_{0.59}Ca_{0.41}MnO_3$ film is closer to the limit of metallicity than the $La_{0.60}Ca_{0.40}MnO_3$ film, and small compositional differences in the doped manganites have been found to lead to significant changes in the resultant physical properties.

8.2 Outlook

The findings of this dissertation have inevitably left some unanswered questions. Firstly, because it has been shown that the limit of ferromagnetism and metallic behaviour can be moved to below the corresponding value for the bulk material by using an in-plane tensile strain; it may be possible to move this limit to greater levels of Ca doping for compressive strains, e.g. by using $LaAlO_3$ as a substrate. Metallic behaviour at 20 K has been reported in $La_{0.5}Ca_{0.5}MnO_3$ films grown on $LaAlO_3$ [3], Additionally, ferromagnetic metallic behaviour has already

been seen in $La_{1-x}Ca_xMnO_3$ (x<0.2) films grown on $LaAlO_3$ [4], which is a composition where the bulk material is a ferromagnetic insulator and the dominant magnetic interaction is superexchange. It therefore seems that reducing the Mn-O-Mn bond length and increasing the orbital overlap can promote double exchange and lead to ferromagnetism and metallic behaviour.

Another possible experiment would be to pattern tracks into $La_{1-x}Ca_xMnO_3$ films on a range of substrates near to the limit of metallic behaviour to see if the same relaxation phenomena are present and if the magnetic shape anisotropy can influence the relative stability of the competing phases. Such tracks would have a different geometry to the film and the strain state may differ along the edges of the tracks. However, the edges of the tracks might be damaged during production, which would make it difficult to distinguish intrinsic and extrinsic effects. Additionally, it might be possible to obtain a single phase in the track, although this might not be reproducible.

Although it did not arise in this work, recent studies in the group have found that there are reproducibility issues with the low-temperature transport properties of $La_{0.60}Ca_{0.40}MnO_3$ and $La_{0.59}Ca_{0.41}MnO_3$ films in that films grown under the conditions described in Section 4.2 did not always show metallic behaviour at 20 K. This can probably be attributed to structural differences in the films, e.g. coherency of strain, and could be investigated more thoroughly using X-ray diffraction techniques. Furthermore, the degree of correlation between the electrical, magnetic and structural properties could be studied.

Another possible extension to this work would be to deposit films of different thicknesses. Film thickness and the coherency of the strain may be important factors in determining the properties of strained films, particularly if there is an insulating 'dead' layer close to the film-substrate interface as has been inferred in manganite films [5,6]. However, as the thickness increases, the film should start to partially relax and the behaviour should tend to that of the bulk material, i.e. there should be a metal-insulator transition around 240 K for all the compositions studied here.

Finally, the characterisation techniques employed in this dissertation have concentrated on the macroscopic properties of the samples at the expense of microscopic properties, in particular the spatial distribution of the competing phases.

It should be possible to observe the spatial extent of the FM regions using TEM and see if the phase coexistence occurs on a microscopic or mesoscopic lengthscale and possibly produce a spectroscopic map of metallic and insulating regions.

References for Chapter 8

[1] S. Jin, T.H. Tiefel, M. McCormack, R.A. Fastnacht, R. Ramesh and L.H. Chen, *Thousandfold Change in Resistivity in Magnetoresistive La-Ca-Mn-O Films.* Science **264**, 413-5 (1994).

[2] F. Rivadulla, M.A. López-Quintela and J. Rivas, *Origin of the Glassy Magnetic Behaviour of the Phase Segregated State of the Perovskites.* Phys. Rev. Lett. **93**, 167206 (2004).

[3] E.B. Nyeanchi, I.P. Krylov, X.-M. Zhu and N. Jacobs, *Ferromagnetic ground state in $La_{0.5}Ca_{0.5}MnO_3$ thin films.* Europhys. Lett. **48**, 228-32 (1999).

[4] W. Prellier, M. Rajeswari, T. Venkatesan and R.L. Greene, *Effects of annealing and strain on $La_{1-x}Ca_xMnO_3$ thin films: A phase diagram in the ferromagnetic region.* Appl. Phys. Lett. **75**, 1446-8 (1999).

[5] J.Z. Sun, D.W. Abraham, R.A. Rao and C.B. Eom, *Thickness-dependent magnetotransport in ultrathin manganite films.* Appl. Phys. Lett. **74**, 3017-9 (1999).

[6] M. Bibes, Ll. Balcells, S. Valencia, S. Sena, B. Martínez, J. Fontcuberta, S. Nadolski, M. Wojcik and E. Jedryka, *Thickness dependence of surface roughness and transport properties of $La_{2/3}Ca_{1/3}MnO_3$ epitaxial thin films.* J. Appl. Phys. **89**, 6686-8 (2001).